

THE $M_{\alpha,\beta}$ X-RAY EMISSION SPECTRA

OF THE HEAVY RARE EARTHS

Howard Anthony Padmore

A thesis submitted to the University of Leicester
for the degree of Doctor of Philosophy

1983

UMI Number: U346597

All rights reserved

INFORMATION TO ALL USERS

The quality of this reproduction is dependent upon the quality of the copy submitted.

In the unlikely event that the author did not send a complete manuscript and there are missing pages, these will be noted. Also, if material had to be removed, a note will indicate the deletion.



UMI U346597

Published by ProQuest LLC 2015. Copyright in the Dissertation held by the Author.
Microform Edition © ProQuest LLC.

All rights reserved. This work is protected against
unauthorized copying under Title 17, United States Code.



ProQuest LLC
789 East Eisenhower Parkway
P.O. Box 1346
Ann Arbor, MI 48106-1346



Thesis
21.5.1984

CONTENTS

	<u>Page</u>
Abstract	
Acknowledgements	
CHAPTER 1 : INTRODUCTION	1.
CHAPTER 2 : THE M SPECTRA OF THE RARE EARTHS	6.
2:1 The $M_{4,5}$ Absorption Spectra and $M_{\alpha,\beta}$ Emission Spectra of the Rare Earths	6.
2:2 Theories of the Origin of X-ray Emission Satellite Lines	14.
2:2:1 The Effect of Auger and Autoionising Processes in X-ray Emission	15.
2:2:2 Wentzel-Druyvesteyn Satellites	17.
2:2:3 Coster-Kronig Satellites	18.
2:2:4 Low Energy Satellites	19.
2:3 The Present Study: The $M_{\alpha,\beta}$ Structures of Thulium, Ytterbium and Lutetium	20.
2:4 Experimental Requirements for Recording Rare Earth $M_{\alpha,\beta}$ Structures Generated by Electron Bombardment	27.
CHAPTER 3 : EXPERIMENTAL APPARATUS	29.
3:1 Classification of Crystal Types	30.
3:2 Corrections to the Bragg Law due to Refraction	31.
3:3 Characteristics of Crystal Spectrometers	31.
3:4 Theories of X-ray Diffraction by a Crystal	33.
3:5 Choice of Type of X-ray Spectrometer	34.
3:5:1 Plane Crystal Spectrometers	34.
3:5:2 Focusing Crystal Spectrometers	36.
3:6 Horizontal Focusing Spectrometers	36.
3:6:1 Defocusing in Johann Geometry Spectrometers	37.
3:7 Choice of Geometry and Selection of Crystals for a Focusing Spectrometer	41.

	<u>Page</u>
3:8 X-ray Wavelength Units	42.
3:9 The Spectrometer	44.
3:9:1 General Arrangement of the Spectrometer.	45.
3:9:2 Mechanical Arrangement of the Spectrometer Table	50.
3:9:3 The Slit and Counter Mechanism	53.
3:9:4 Mechanical Arrangement of the Crystal Chamber and Crystal Block	55.
3:9:5 The X-ray Source Chamber	57.
3:9:6 The Electron Gun and Power Supply	60.
3:9:7 The Vacuum Metal Evaporator	62.
3:9:8 The Spectrometer Vacuum System	63.
3:9:9 Adjustment and Calibration of the Spectrometer	64.
 CHAPTER 4 : THE SPECTROMETER DETECTION AND CONTROL SYSTEMS	 67.
4: <u>Part a</u> The Microprocessor Controlled Data Acquisition System	67.
4:a(1) Stepping Motor Oscillators and Interfaces	73.
4:a(2) Crystal Angle Measurement	74.
4:a(3) Unit 1: The Data Sampler, Display and Formatter	76.
4:a(4) Unit 2: The Digital Tape Recorder	77.
4:a(5) The a.c. Motor Control System	78.
4:a(6) The Microprocessor Hardware	81.
4:a(7) The Microprocessor Software	82.
<u>4:Part b</u> The X-ray Photon Detection System	83.
4:b(1) The Gas Flow Proportional Counter	84.
4:b(2) The Detection Electronics and Gas Supply System	86.
<u>4:Part c</u> Operation of the Spectrometer Detection and Control Systems	87.

	<u>Page</u>
CHAPTER 5 : EXPERIMENTAL TECHNIQUES AND RESULTS	90.
5:1 Deconvolution of Self Absorption Effects in the Spectra of the Rare Earths	92.
5:2 Treatment of Data	94.
5:3:1 The m_{α} Emission Spectrum of Ytterbium Metal	96.
5:3:2 The $m_{\alpha,\beta}$ Emission Spectra of Ytterbium in Ytterbium Fluoride	98.
5:3:3 The $m_{\alpha,\beta}$ Emission Spectra of Lutetium in Lutetium Fluoride	100.
5:3:4 The $m_{\alpha,\beta}$ Emission Spectra of Thulium Metal	101.
5:3:5 The $m_{\alpha,\beta}$ Emission Spectra of Thulium in Thulium Fluoride	101.
CHAPTER 6 : DISCUSSION AND CONCLUSION	103.
6:1 Resonance Emission in Lanthanum	107.
6:2 Competing processes in the Spectra of the Heavy Rare Earths	109.
6:3 The $m_{\alpha,\beta}$ Region of Lutetium Fluoride	111.
6:4 The m_{α} Region of Ytterbium Metal	114.
6:5 The $m_{\alpha,\beta}$ Region of Ytterbium Fluoride	117.
6:6 The $m_{\alpha,\beta}$ Region of Thulium Metal and Fluoride	122.
6:7 Experimental Refinements	125.
6:8 Conclusions	127.
APPENDIX	129.
REFERENCES	139.

ABSTRACT

The $m_{\alpha,\beta}$ x-ray emission spectra of some of the heavy rare earths were measured using a high resolution x-ray spectrometer. The x-ray spectrometer was designed to allow the preparation of pure samples in ultra-high vacuum conditions so that accurate spectra could be measured. Due to the large number of measurements necessary, the spectrometer was automatically controlled by a microprocessor based system.

From the high resolution data obtained, it has been possible to produce an explanation of the gross structures seen in the rare earth $m_{\alpha,\beta}$ x-ray emission spectra. It has been shown that the spectra are made up from several competing processes but that the main features can be explained in terms of resonant excitation of a 3d electron to the 4f shell followed by 4f - 3d emission and by normal 4f - 3d emission after ionisation of a 3d electron. Modifications to the spectra caused by excited final state transitions have also been observed. The dramatic effects on the m_{α} spectra of ytterbium due to chemical combination have also been explained in terms of the reduction of the 4f occupancy from $4f^{14}$ to $4f^{13}$.

It has been shown that much of the published data for the $m_{\alpha,\beta}$ rare earth emission spectra is incorrect. The distorting effects of self absorption and sample contamination have been shown to be particularly severe for the rare earths.

ACKNOWLEDGEMENTS

I would like to record my deep gratitude to Mr. J.E. Wilson for his unfailing supervision of this work. I also wish to thank the SERC for the award of a maintenance grant.

I would also like to thank Dr. C. Norris for his interest and encouragement.

I have been greatly helped by the expert technical support provided by the Physics Department Mechanical and Electronics Workshops under Mr. R. Cox and Dr. T. Harris respectively.

I would also like to express my thanks to Mr. J.S.G. Taylor for my education in ultra-high vacuum technology and for the loan of much equipment.

For my introduction to microelectronics I would like to thank all the members of the Ionospheric Physics group and particularly Mr. C. Thomas.

Finally, I would like to thank Mrs. M. Dickson for her careful typing of this thesis.

CHAPTER 1Introduction

If a core hole is created in an atom by the removal of an electron by some ionising process, the hole can be filled by an electron from a higher energy level. If this de-excitation is accompanied by the emission of a quantum of radiation, then the mechanism is that of x-ray emission. If the ionisation occurs as the result of the absorption of a quantum of energy from a surrounding photon radiation field, this is known as x-ray absorption. The energy of x-ray photons is such that the transitions involved in emission or absorption originate from widely separated energy levels, one of which is a deep core level. The binding energy of electrons in these levels is so large that the character of the absorption spectrum is dominated by the nature of the core level and not by variations in the energy of the final state. A plot of the absorption coefficient of a material over a wide range of energies will show a series of discontinuities at energies just sufficient to remove electrons from the various core levels. The edge discontinuities are named in the manner of the initial level of the ejected electron, for example K, L₁, L₂, L₃. An electron need not be completely removed from the atom but merely excited into one of the optical levels. These levels are quantized energy states and therefore transitions which result from the absorption mechanism are subject to the usual selection rules. (Condon and Shortley, 1935). If the azimuthal quantum number associated with the initial level is l , then the final level must possess $l \pm 1$ symmetry. From a consideration of x-ray emission lines it appears that transitions to states possessing $l - 1$ symmetry are less probable and so the character of absorption spectra will be mainly dependent on $l + 1$ symmetry (Parratt, 1959).

The binding energies of the optical electrons are small compared to the binding energy of the deep core levels and when the absorbing material is a system of non-interacting atoms such as in a monatomic gas, the optical electrons occupy a set of energy levels which rapidly converge to a series limit. The absorption spectrum in this case therefore shows fine structure on and near the absorption edge and this has been observed in the rare gases by Parratt (1939). In the solid state, the outermost energy levels are strongly perturbed by the crystal field. In a system of N non-interacting atoms, corresponding electrons in all of the atoms possess the same energies, that is they occupy common degenerate energy states. In the solid state, if the electrons are sufficiently close together that the interatomic distances are comparable to the spatial extent of the outer shell electron orbitals; the energy degeneracies are removed so that a given degenerate state will split up into a set of N discrete levels forming an energy band. At large binding energies, the bands become narrow and in the limit represent the discrete atomic energy levels of a free atom, but if the binding energy is small the energy bands are wide. In the limiting case of an electron possessing zero binding energy, it will behave as a free electron. This leads to a clear distinction in the band picture of solids between the electronic structure of metals and insulators. If a material possesses metallic properties then either the highest filled band overlaps the first unoccupied band, or the highest occupied band is only partially filled. The highest occupied level within this band, known as the valence band, is called the Fermi level. In an insulator all the occupied bands are filled and in this case a large gap exists between the occupied and unoccupied bands. The energy bands will also have an associated symmetry which is derived from their equivalent atomic level, that is there will be s,p,d,f symmetry bands, but there will also

be bands of mixed symmetry caused by the overlap of individual bands. This type of mixed band is known as a hybridised band. Absorption spectra will therefore give information about the density of electron states within the unoccupied bands above the Fermi level, although this information is convoluted with the transition probabilities between these bands and the inner atomic states of particular symmetry. In contrast, x-ray emission can give information about the density of occupied states within a band. An important point is that the density of unoccupied states measured by x-ray absorption is that for the particular case where there is a hole in an inner core level and the density of occupied states as measured by x-ray emission is that for the case where there is a hole in the occupied band at the end of the emission process. These processes can only be approximated by one electron transitions as within the lifetime of the absorption or emission event rearrangements of other electronic states also occurs. X-ray absorption and emission measurements can give useful information on unoccupied and occupied states but this information is distorted by transition probabilities and the excited state nature of the spectroscopy. In metals, the onset of absorption caused by removal of a core electron to an unoccupied band should correspond to the energy of a photon emitted after an electron has dropped from the highest occupied level into the core hole. In insulators, due to the gap between occupied and unoccupied bands there should be a corresponding gap between absorption and emission structures involving the same core level.

X-ray emission and absorption processes can also occur involving transitions to and from a partially filled core level such as occurs in the lanthanide and actinide elements. If the partially filled core level is localised so that there is negligible perturbation from the crystal field then sharp line

absorption structures will be seen. In the rare earth metals, although the 4f level is situated close to the Fermi level, the 4f electrons are highly localised and unperturbed by the crystal field. It is possible therefore to have both emission and absorption transitions involving a deep core level, the localised 4f level and the occupied and unoccupied bands giving structures in the same photon energy range. Also, due to reciprocal absorption and emission processes being possible, x-ray emission spectra can be distorted by reabsorption of the x-ray photons in the material under examination.

The purpose of this investigation was to measure the $M_{\alpha,\beta}$ emission spectra of three of the rare earths, thulium, ytterbium, and lutetium in order that a model could be formed for the mechanisms responsible for the complex structures observed by many experimenters in rare earth m series spectra. The chosen materials represent the simplest rare earths from the point of view of m series x-ray emission, and both thulium and ytterbium were studied in both metallic and compound form to demonstrate the effect of bonding on the electronic structure of the rare earths.

Due to the reactivity of the rare earth metals and the relatively small cross section for the $M_{\alpha,\beta}$ transition, a new type of high resolution spectrometer was built involving ultra-high vacuum sample preparation, focusing crystal optics, computer controlled data acquisition and electronic spectrometer coordination.

Chapter 2 outlines the nature of the $M_{4,5}$ absorption and the $M_{\alpha,\beta}$ emission in the rare earths and discusses the special problems associated with recording accurate rare earth emission structures. Chapter 3 discusses the principles of x-ray spectrometry and describes the spectrometer system that was developed during the course of this work. In chapter 4, the computer

control system and the photon detection system used in the spectrometer are presented. The experimental techniques developed to record $M_{\alpha,\beta}$ spectra are discussed in Chapter 5, together with a presentation of the results. In Chapter 6, a general discussion of the work is presented together with some conclusions and suggestions for future measurements and experimental refinements.

CHAPTER 2

THE M SPECTRA OF THE RARE EARTHS

	<u>Page No.</u>
<u>Introduction</u>	6.
2:1 The $M_{4,5}$ Absorption Spectra and $M_{\alpha,\beta}$ Emission Spectra of the Rare Earths.	6.
2:2 Theories of the Origin of X-ray Emission Satellite Lines	14.
2:2:1 The Effect of Auger and Autoionising Processes in X-ray Emission.	15.
2:2:2 Wentzel-Druyvesteyn Satellites.	17.
2:2:3 Coster-Kronig Satellites.	18.
2:2:4 Low Energy Satellites	19.
2:3 The Present Study:	
The $M_{\alpha,\beta}$ Structures of Thulium, Ytterbium and Lutetium.	20.
2:4 Experimental Requirements for Recording Rare Earth $M_{\alpha,\beta}$ Structures Generated by Electron Bombardment.	27.

CHAPTER 2THE M SPECTRA OF THE RARE EARTHSIntroduction

The rare earth series of elements is characterised by a gradual filling of the 4f shell, from an empty shell in the case of lanthanum to a full shell with fourteen electrons in the case of ytterbium. These elements also possess the common feature of a xenon core structure of electrons with two or three loosely bound valance electrons. At the beginning of the rare earth series it has been shown that the spatial extension of the 4f eigenfunctions drops suddenly (Mayer, 1941; Coulson and Sharma, 1962; Rau and Fano, 1968) and that there is a corresponding rapid reduction in the binding energy of the 4f electrons (Mayer, 1941). In lanthanum ($Z = 57$), the 4f eigenfunction is essentially located outside the xenon core but in neodymium ($Z = 60$) it has contracted so that its maximum lies inside the $5s^2 5p^6$ closed shells of the xenon configuration. The 4f electrons are therefore located deeply within the atom and behave essentially as members of a closed shell, the localisation increasing towards the heavier rare earths as the 4f contraction continues.

The physical and chemical properties dependent on the valance electron state are therefore very similar throughout the rare earth elements, all the elements being metallic with a valancy of three except for cerium, europium and ytterbium. Due to the tendency of the 4f shell to be either half full or full, both europium and ytterbium are divalent in the solid state. Cerium exhibits anomalous behaviour with a valance between three and four depending upon the phase state of the metal (Spedding and Duane, 1961; Gschneidner and Smoluchowski, 1963).

2:1 The $m_{4,5}$ absorption spectra and $m_{\alpha,\beta}$ emission spectra of the rare earths

The localisation of the 4f electrons in the rare earths leads

to many interesting effects in the m series spectra. The $m_{4,5}$ absorption spectra are found to consist of strong lines as originally shown by Lindburg (1931) for erbium and ytterbium. Subsequently all the elements of the rare earth series have been measured using photographic techniques by Rule (1945), Lee and Stewardson (1951), Lee, Stewardson and Wilson (1952), Zandy (1952, 1967), Stewardson and Wilson (1956), Russell (1958), Williams (1966) and by Bonnelle and Karnatak (1969). In none of this photographic work were any edge absorption structures found corresponding to the ionisation of a 3d electron. In more sensitive measurements in which photon counting techniques were used, true edge absorption was observed in hafnium and lutetium (Combley, 1963), in lanthanum and cerium (Ottewell, 1969; Ottewell, Stewardson and Wilson, 1973) and in ytterbium (Combley, Stewardson and Wilson, 1968). Edge absorption was also seen in tantalum (Combley, 1963) and in barium and caesium (Ottewell, 1969). The absorption edges are characterised by a broad weak rise in absorption whereas the absorption lines are strong sharp absorptions. The weak absorption edges are due to transitions into an unoccupied f symmetry final state band. The m_4 and m_5 spectra are well separated due to large 3d spin orbit splitting and the individual components are made up of closely overlapped components due to 3d - 4f exchange interaction. For lanthanum in which the 4f level is empty, the total angular momentum of the atom in the ground state will be $J = 0$. On promotion of an electron from the 3d level to the 4f level, the total angular momentum of the incomplete 3d shell then takes a value corresponding to that of a single 3d electron. Therefore,

$$j_1 = l_1 \pm s_1, \quad l_1 > s_1, \quad 2(1)$$

where l_1 and s_1 are the orbital angular momentum quantum number and the spin angular momentum quantum number respectively of the equivalent d electron. As $l_1 = 2$ and $s_1 = \pm \frac{1}{2}$, j_1 will take

the values $5/2$ or $3/2$. The total angular momentum of the f electron may be similarly represented by,

$$j_2 = l_2 \pm s_2 \quad l_2 > s_2 \quad 2(2)$$

where $l_2 = 3$ and $s_2 = \frac{1}{2}$ giving $j_2 = 7/2$ or $5/2$.

Since on the basis of a simple vector model the calculated number of components is independent of the coupling scheme used, it is convenient to assume simple jj coupling. Using this coupling scheme, the total angular momentum of the atom can be represented by;

$$J = j_2 \pm j_1 \quad j_2 > j_1 \quad 2(3)$$

where any integral value of J between $J = j_2 + j_1$ to $j_2 - j_1$ is allowed.

For the m_5 absorption line $j_1 = 5/2$ therefore;

$$J = 5/2 + 5/2 \rightarrow 5/2 - 5/2 = 5, 4, 3, 2, 1, 0 \quad j_2 = 5/2 \quad 2(4)$$

$$J = 7/2 + 5/2 \rightarrow 7/2 - 5/2 = 6, 5, 4, 3, 2, 1 \quad j_2 = 7/2$$

The selection rules dictate that

$$\Delta J = 0 \pm 1 \quad J = 0 \rightarrow J = 0 : \text{forbidden} \quad 2(5)$$

The final levels $(j_1, j_2)_J$ allowed are therefore,

$$(5/2, 5/2)_1 ; (5/2, 7/2)_1$$

For lanthanum there should therefore be two m_5 lines. In

the case of the m_4 absorption line, $j_1 = 3/2$ therefore

$$J = 5/2 + 3/2 \rightarrow 5/2 - 3/2 = 4, 3, 2, 1 \quad j_2 = 5/2 \quad 2(6)$$

$$J = 7/2 + 3/2 \rightarrow 7/2 - 3/2 = 5, 4, 3, 2 \quad j_2 = 7/2$$

Therefore only one m_4 line is allowed corresponding to a final state of $(3/2, 5/2)_1$. On this basis, the number of components in the m_4 and m_5 structures has been experimentally verified for lanthanum (Ottewell, 1969; Karnatak, Esteva and Connerade, 1981), thulium (Wilson, 1978; Belrhmi-Belhassan, Karnatak, Spector and Bonnelle, 1981) and Ytterbium oxide (Combley, Stewardson and Wilson, 1968; Karnatak, 1971; Karnatak,

Esteva and Connerade, 1981). The case of ytterbium oxide (Yb_2O_3) is the simplest with a single m_5 component and no m_4 component resulting from the single vacancy in the 4f shell. Due to the complete 4f shell in ytterbium no line absorption can take place. In the case of thulium with twelve 4f electrons, three components are predicted for m_5 and one for m_4 . In the case of lanthanum, as shown above, two components are expected for m_5 and one for m_4 . In the cases where there is either a single component in a line or the components are well separated, there is complete agreement with experiment. In the case of intermediate rare earths, many components are predicted ranging up to several hundred for the middle rare earths and so unambiguous identification of components is impossible. A calculation for an atom containing only one 4f electron in the ground state yields 23 and 30 components for m_4 and m_5 respectively. Calculations of the line positions within the multiplet depend upon the coupling scheme used. For instance, if jj coupling is used to calculate the splitting of the $(5/2\ 5/2)$, $(5/2\ 7/2)$, m_5 components in lanthanum, the splitting is found to be approximately 0.3eV in comparison to the measured value of 3.8eV. An intermediate coupling scheme has been proposed (Ottewell, 1969) in which the resultant of the spin-orbit coupling within the d shell is strongly coupled with the l vector of the f electron to produce a resultant vector k. This is strongly coupled to the spin vector of the f electron to produce J, the resulting total angular momentum for the atom. All other vector couplings were neglected. This scheme may be represented by,

$$J = (j_1 \cdot l_1) \cdot s_2 = k \cdot s_2 \quad 2(7)$$

This model was found to give excellent agreement with experiment for lanthanum, quadrivalent cerium and thulium. Sugar (1972A) has investigated various coupling schemes and calculated the

intensities of the individual component lines based on a method developed for $4d - 4f$ absorption spectra (Sugar, 1972B). This model originally applied to erbium and thulium has been used for lanthanum and cerium in metallic and oxide form (Bonnelle, Karnatak and Sugar, 1974), for europium and gadolinium (Bonnelle, Karnatak and Spector, 1977) and in a remeasurement of thulium $m_{4,5}$ (Belrhmi-Belhassan, Karnatak, Spector, and Bonnelle, 1981). In all cases good agreement of peak positions and intensities between experiment and theory have been found. The line widths and line shapes of absorption lines in the simple rare earths has also been examined (Connerade and Karnatak, 1981; Karnatak, Esteva and Connerade, 1981). For lanthanum, the absorption and emission measurements by Mariot and Karnatak (1974) which revealed an intensity anomaly in the ratio of $m_{4,5}$ to $m_{\alpha,\beta}$ and the existence of asymmetric peak shapes, were explained using a model involving Coster-Kronig and autoionisation decay modes. The role of Coster-Kronig and autoionising transitions is discussed later in this chapter.

There therefore exists a wide body of information on $m_{4,5}$ line and edge absorptions and the origin of the spectral features appears to be well understood. In the case of the $m_{\alpha,\beta}$ emission spectra however not as much experimental evidence exists as for the $m_{4,5}$ absorption and the spectra appear to be more complex and not well understood. In general, the $m_{\alpha,\beta}$ structures directly overlap in energy the corresponding $m_{4,5}$ absorptions and similarly have multiplet structure due to coupling between the incomplete $3d$ and $4f$ shells. The $m_{\alpha,\beta}$ spectra were first observed by Van der Tuuk (1927) and Lindberg (1931) and the correspondence between $m_{4,5}$ and $m_{\alpha,\beta}$ structures was noted by Rule (1945) and confirmed by Zandy (1952) for measurements on samarium. The $m_{4,5}$ and $m_{\alpha,\beta}$ spectra of erbium were investigated by Stewardson and Wilson (1956) and revealed a complete

overlap of absorption and emission lines. It was noted in the emission measurements that the overlapping components became much more distinct at higher excitation energies and it was concluded that at least some of the structure was due to self absorption in the target material. The self absorption effect was investigated for all the rare earths in both oxide and metallic form by Fischer and Baun (1967), both $m_{4,5}$ and $m_{\alpha,\beta}$ spectra being recorded. The $m_{\alpha,\beta}$ spectra were measured at various excitation energies and takeoff angles and revealed that either at high energy or low takeoff angle large self absorption features appeared in the emission spectra which completely agreed with the measured $m_{4,5}$ spectra. Under these conditions the emission spectra were grossly distorted with some strong emission features recorded under minimised self absorption conditions being completely absent under these strong absorption conditions. The $m_{\alpha,\beta}$ spectra were then measured at low excitation voltage under conditions which minimised self absorption and shown to consist of single lines for m_{α} and m_{β} although the lines were in general non-lorentzian and asymmetric. The nearest approximation to symmetric line shapes was found for elements with either an empty or a full 4f shell at excitation voltages only three hundred volts above the m_4 threshold. Fischer and Baun concluded therefore that all the multiplet structure in the $m_{\alpha,\beta}$ spectra was caused by self absorption, the multiplicity only being evident in the absorption process, and that the m_{α} and m_{β} structures were single lines with associated high energy satellites causing asymmetrical line shapes. It was also noted that no change could be found in the spectra on going from a metallic to compound form except for europium and ytterbium. The spectrum of metallic ytterbium was recorded but the metallic europium sample was too reactive to be recorded accurately. The peak of the ytterbium

m_{α} spectrum showed a 4eV shift to higher energy when going from the metallic to oxide state and was correlated with the work of Combley, Stewardson and Wilson (1968) on the oxidation of ytterbium metal as observed by m_{β} x-ray absorption. The change in the x-ray emission spectra for ytterbium and europium can be correlated with a change in valance from two to three on oxidation which causes the occupation of the 4f shell to drop by one (Topp, 1965). The m_{α} spectra of ytterbium and hafnium in the oxide form have been studied by Parrott (1965) under conditions of minimised self absorption and showed that at higher excitation energies, anomalously large satellite emission was observed on the high energy side of the main m_{α} peak for ytterbium, but not for hafnium. The satellites were observed to be highly excitation voltage dependent and an attempt was made to analyse the satellite structure into overlapping lorentzian components. In comparison to ytterbium, the hafnium satellites were very weak and far less excitation energy dependent. The m_{α} spectrum of metallic ytterbium was recorded but was found to be not reproducible in shape due to oxidation. The $m_{\alpha,\beta}$ spectra of cerium, europium, gadolinium, dysprosium and ytterbium have been studied in the metallic and oxide state, (Karnatak, 1971; Bonnelle and Karnatak, 1969, 1970) the metallic surface being coated with aluminium in an attempt to prevent oxidation. This work was conducted under conditions of minimised self absorption and at excitation voltages fairly close to threshold and showed that the $m_{\alpha,\beta}$ structures were not single lines as suggested by Fischer and Baun (1967), but had several weak low energy components and voltage sensitive high energy components. In the case of metallic ytterbium, the m_{α} structure was observed to be 2eV lower in energy than the metallic spectra of Fischer and Baun (1967) and was shown to contain a large voltage sensitive high energy

component even at low excitation energies. The x-ray fluorescence $m_{\alpha,\beta}$ spectra have been measured for gadolinium and ytterbium in the oxide form by La Villa (1974) and show a single broad line for m_{α} and m_{β} in the case of ytterbium oxide. The m_{α} peak is shifted by approximately 4eV to higher energy compared with the m_5 absorption measurements of Karnatak (1971) and Combley, Stewardson and Wilson (1968) although a small structure can be seen in the spectra as a shoulder at the m_5 absorption energy. The $m_{\alpha,\beta}$ spectra of ytterbium in metallic and oxide form are discussed in detail later in this chapter.

At excitation energies very close to threshold, the $m_{\alpha,\beta}$ spectra of the rare earths has been shown to be very voltage dependent. The $m_{\alpha,\beta}$ spectra of lanthanum and cerium in the metallic state have been studied from the m_5 threshold to 15eV above the m_4 threshold and show large oscillations in the intensity of spectral features as a function of excitation energy (Liefeld, Burr and Chamberlain, 1974; Chamberlain, Burr and Liefeld, 1974). These effects were ascribed to resonances in the cross section for scattering of incident electrons into the vacant 4f level, the mechanism involved being due to the m_5 or m_4 vacancy and the incident electron and the excited 3d electron in a two electron bound state. In these near threshold spectra the m_{α} and m_{β} structures do not have any high energy components, but do have a low energy component which gets weaker with respect to the main line with increasing excitation energy. This low energy shoulder is still observable at an excitation energy over 600eV higher than the m_5 threshold in both metallic cerium (Karnatak, 1971) and metallic lanthanum (Mariot and Karnatak, 1974), but is much weaker than at low excitation energy. In the $m_{\alpha,\beta}$ spectra of lanthanum and cerium recorded at 1500eV excitation energy, satellite structure has appeared on the high

energy side of the main $m_{\alpha,\beta}$ structures but is still relatively small compared to the main feature.

The identification of components in the $m_{\alpha,\beta}$ spectra of the rare earths appears uncertain, with several processes possibly taking place to produce a spectrum. The identification of components has been confused by most early work suffering from self absorption and the spectra of the metals being often recorded from partially oxidised samples. The rare earth metals are highly reactive and in the cases of europium and ytterbium, oxidation induces a valance change which reduces the occupation of the 4f shell and completely alters the $m_{\alpha,\beta}$ emission spectra. Some features in the $m_{\alpha,\beta}$ spectra appear to be due to the normal transition involving ionisation of the 3d shell with the subsequent transition of a 4f electron into the 3d hole and some appear to be due to resonance transitions involving the promotion of a 3d electron to the 4f level. These transitions are discussed in detail later in this chapter. Further components appear to be due to satellites of the $m_{\alpha,\beta}$ lines and the origin of satellites in x-ray emission spectra is dealt with in the next section of this chapter.

2:2 Theories of the origin of x-ray emission satellite lines

X-ray satellites were first found in the K emission spectrum of zinc by Siegbahn and Stenstrom (1916). Satellites usually lie close to a parent line and are sometimes referred to as non-diagram lines as they cannot be understood by one electron transitions represented by the usual x-ray energy level diagram of a singly ionised atom. The field of x-ray satellite emission is very large and so only the most important types of satellite transitions will be discussed. Before specific satellite processes are considered, the role of Auger and autoionising processes must first be considered.

2:2:1 The effect of Auger and autoionising processes in x-ray emission

After ionisation of a core level, the atom can return to the ground state by various processes. The two dominant processes are those of x-ray emission and Auger decay. In the former decay process, the core level is filled by an electron from a higher level with the emission of a photon of characteristic energy given by the energy difference between the two levels involved in the transition. The second process does not lead to the emission of a photon but rather the filling of the core hole leads to the ejection of an electron from a higher level. If we consider an ionisation in the K shell, then an electron from the L level could fill the core hole with the ejection of an M electron with a kinetic energy given by,

$$E_{kin} = E_K - E_L - E_M \quad 2(8)$$

This is normally represented as a KLM Auger transition, the initial hole being in the K shell and the final holes being in the L and M shell. A KLL transition would leave two holes in the L shell. The Auger process therefore leads to doubly ionized atoms. As the Auger process competes with the x-ray emission process it influences the lifetime of states and hence the width of emission lines. It also influences the intensity of x-ray emission lines due to the transfer of inner holes. Due to the production of doubly ionised atoms transitions that subsequently follow will lead to the production of satellite lines.

Auger transitions in which the initial hole and one of the final state holes are in the same shell are known as Coster-Kronig transitions (Coster and Kronig, 1935). If the ionisation energies of two inner subshells are E_{x_i} and E_{x_f} and the energy of the outer level from which the Auger electron is ejected is E_y , then the kinetic energy of the electron is given by,

$$E_{kin} = E_{x_i} - E_{x_f} - E_{\gamma} \quad 2(9)$$

and will only occur if

$$E_{x_i} - E_{x_f} > E_{\gamma} \quad 2(10)$$

As for the Coster-Kronig transition, this is represented by $X_i X_f Y$. From 2(10) it can be seen that particular Auger and Coster-Kronig transitions can only occur over certain ranges of atomic number. A list of possible Auger and Coster-Kronig transitions has been given by Cooper (1944). Because of the change in screening when an inner electron is missing, equation 2(10) has to be altered to take account of the increase in the effective nuclear charge. To a first approximation the outer electron sees a field of charge $Z + 1$ and so equation 2(10) becomes,

$$E_{x_i}(Z) - E_{x_f}(Z) > E_{\gamma}(Z+1) \quad 2(11)$$

and so 2(9) becomes

$$E_{kin} = E_{x_i}(Z) - E_{x_f}(Z) - E_{\gamma}(Z+1) \quad 2(12)$$

A comprehensive calculation of Auger and Coster-Kronig transition probabilities and line widths has been made by McGuire (1971A, 1971B, 1972A, 1972B) including M shell transitions, which have also been calculated by Chen, Crasemann and Mark (1980).

A process similar to the Auger process is that of auto-ionisation. An electron is first promoted to an outer level instead of being ionised as in the Auger process. If the excitation energy is greater than the ionisation energy of any of the other electrons present, the excited atom will eject an electron and reorganise to an ion. In the Auger process the core electron is ionised instead of being promoted to an outer level and this results in a doubly ionised final state instead of the singly ionised final state after an autoionising transition. In this case, the ejected electron is known as the autoionisation electron. Again, this is a competitive process to radiative decay and so alters the width and intensity of emission

lines resulting from radiative decay.

2:2:2 Wentzel-Druyvesteyn satellites.

In the original theory of Wentzel (1921), it was suggested that the K satellites originated from an initial state of multiple ionisation caused by a single electron impact. The K_{α} satellites were assigned to the transitions,

$$\begin{array}{ll} K_{\alpha_3} : & KL \rightarrow LL & K_{\alpha_4} : & KK \rightarrow KL \\ K_{\alpha_5} : & KLL \rightarrow LLL & K_{\alpha_6} : & KKL \rightarrow KLL \end{array}$$

the diagram line being due to KL

If the energy required to remove an electron from the K shell in an atom of atomic number Z is $(E_K)_Z$, then the energy required to remove a further K electron is $(E_K)_{Z+1}$ as the effective nuclear charge has been increased by one. The energy needed to remove a third electron, an L electron, would be $(E_L)_{Z+2}$. From these considerations it was shown that the frequency of the satellite components could be given by,

$$\nu_{\alpha_4} - \nu_{\alpha_3} = \nu_{\alpha_6} - \nu_{\alpha_5} \quad (13)$$

$$\nu_{\alpha_5} - \nu_{\alpha_2} = \nu_{\alpha_3} - \nu_{\alpha_1} \quad (14)$$

giving,

$$\nu_{\alpha_6} - \nu_{\alpha_4} = \nu_{\alpha_5} - \nu_{\alpha_3} = \nu_{\alpha_3} - \nu_{\alpha_1} \quad (15)$$

The energy separations of alternate satellite lines should therefore be equal and Wetterblad (1927) provided some experimental justification of this in measurements of the K_{α} satellites for the elements sodium to silicon. The problem with the original Wentzel theory arose from a consideration of the process responsible for double K shell ionisation. A process in which double electron impact creates the double ionisation has a vanishingly small probability, and a process involving the ejection of a second K shell electron by Auger emission is energetically impossible. The only possible process is that the double ionisation is created by a single electron impact. For this process, the excitation potential of the satellite

line due to a transition into one of the K holes should be just over twice that for the parent line caused by a transition into a single K hole. Backlin (1924) found that this was not the case in practice and concluded that none of the K_{α} satellites were due to double ionisation of the K shell. The modification of the original Wentzel theory by Druyvesteyn (1928) suggested that the K satellites could be explained if double ionisation occurred but by single ionisation in different sub shells. Wolfe (1933) and Ramberg and Kennard (1934) extended the Wenzel-Druyvesteyn theory to include coupling between the incomplete shells and spin orbit interaction. Good agreement was found with experiment and it was shown that the $K_{\alpha_{3,4}}$ satellites arose from initial ionisation in the K and L shells with an electron dropping from the L shell into the K hole, and that the $\alpha_{5,6,7,8}$ satellites arose from transitions in atoms lacking two additional L electrons. An extension of the basic model to include different coupling models has been given by Demekin and Sachenko (1967). The Wenzel-Druyvesteyn model has been highly successful and is the standard theory for K emission satellites.

2:2:3 Coster-Kronig Satellites

Although K series satellites may be well explained by a Wenzel-Druyvesteyn process, the peculiar intensity variations of the L and M series satellites cannot be explained by the same process. The Wenzel-Druyvesteyn theory predicts that the intensities of the satellites should decrease towards high atomic number, but for L and M series satellites there appear to be regions of atomic number where the intensity of particular satellites peak and other regions where the satellites disappear only to reappear in atoms of higher atomic number. Coster and Kronig (1935) were the first to consider the Auger process as being responsible for the production of double ionisation of the

atom with the subsequent emission of high energy satellites. The Coster-Kronig process fully explains the observed L satellite intensities and their appearance and disappearance as a function of atomic number. The Coster-Kronig process was originally confirmed by Richtmyer and Ramberg (1937) for the $L_{\alpha_1,2}$ and L_{β} satellites of gold. An excitation study of the L_{α_1} satellites by Valadares and Mendes (1948) confirmed the earlier work of Richtmeyer and Ramberg (1937). They found that if the excitation voltage was reduced below the L_1 excitation limit the L_{α_1} satellites disappeared. This is in agreement with the earlier work as the Coster-Kronig transition $L_1 L_3 M_{4,5}$ had been assigned for the satellite structure ($L_{\alpha_1} : L_3 M_5$). Hirsh (1931, 1941, 1942) has attempted to explain the origin of M-series satellites on the basis of Coster-Kronig transitions. He showed that the transition $M_3 M_5 N_{4,5}$ which is possible for $Z < 88$ and $M_3 M_4 N_{4,5}$ which is possible for $Z < 84$ accounted for m_{α} and m_{β} satellites respectively. Little experimental evidence exists for this and the identification of satellite components in the M series appears to be confused.

2:2:4 Low energy satellites

Low energy satellite lines have been widely observed in both K and L spectra (Beuthe, 1930; Ford, 1932; Valasek, 1938). No single theory has been able to explain the existence of these satellites, but the most applicable model is that of the radiative Auger effect (Åberg, Utriainen 1969). A radiative Auger transition is a double-electron transition, where an outer shell electron $n_{f_1} l_{f_1}$ drops down to fill a core hole $n_i l_i$ and simultaneously another outer shell electron $n_{f_2} l_{f_2}$ is excited into a bound or continuum state ϵl . The energy of the emitted photon can be given by

$$h\nu = E_i - E_{f_1, f_2} - \epsilon \quad 2(16)$$

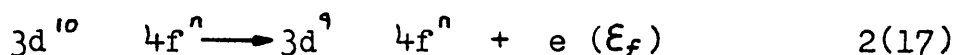
where E_i is the ionisation energy of the $n_i l_i$ level, and E_{f_1, f_2} is the energy required for the simultaneous ionisation of the two electrons $n_{f_1} l_{f_1}$ and $n_{f_2} l_{f_2}$ from the neutral system.

The spectra recorded by Aberg and Utriainen (1969) for $K_{\alpha,1,2}$ satellites of sulphur reveal both radiative Auger transitions in which the promoted electron is excited into bound states giving sharp well defined low energy peaks and radiative Auger transitions where the promoted electron is excited into continuum states giving broad bands of emission. Each band corresponds to different energy terms of the final doubly ionized atom.

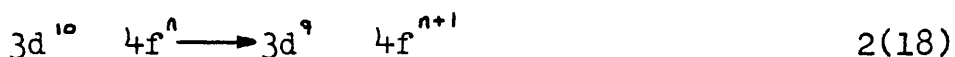
Many other types of satellite transitions have been found to occur and only those processes yielding the principle types of satellite have been discussed. A useful review of the theory of x-ray satellites has been given by Åberg (1966) and a general survey and classification has been given by Deodhar (1962).

2:3 The present study; the $m_{\alpha, \beta}$ structures of thulium, ytterbium and lutetium

As previously discussed in this chapter, the edge absorption process is due to the transition,



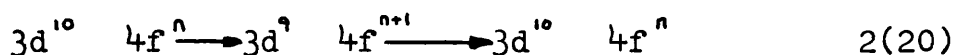
where $e(\epsilon_f)$ indicates that the ejected electron has been promoted to an f continuum state. The line absorptions have also been shown to be due to the transition,



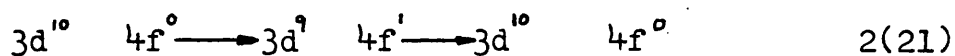
A comparison of the edge and line intensities reveals that the transition of a 3d electron into the 4f shell is much more probable than a transition into a continuum f state. For lanthanum, the line transition would be represented by,



As the m_s and m_α absorption and emission structures in lanthanum directly overlap in energy the initial state for emission must be the same as the final state in absorption. The emission process must therefore have an initial state of $3d^9 4f^1$ for lanthanum, but the normal m_α process which results in the ionisation of the 3d shell gives an initial state for emission of $3d^9 4f^0$. From this initial state, it is obvious that a reciprocal emission line cannot be generated. The probability of excitation of the 3d electron into the 4f level rather than ionisation has been demonstrated by consideration of line and edge absorptions. It is therefore possible for the absorption and emission structures to occur at the same energy in lanthanum if a transition of the following type occurs,



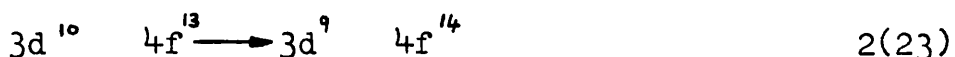
giving for lanthanum,



In this transition it can be seen that the initial state for emission is the same as the final state for absorption giving overlapping m_s , m_α and m_γ , m_β structures. If the m_α spectrum of YbF_3 or Yb_2O_3 is now considered (Parrott, 1965; Karnatak 1971), then due to the vacancy in the 4f shell a transition of the following type should occur,



The m_s absorption in Yb_2O_3 measured by Combley, Stewardson and Wilson (1968) shows a single symmetrical line and was assigned to the transition,

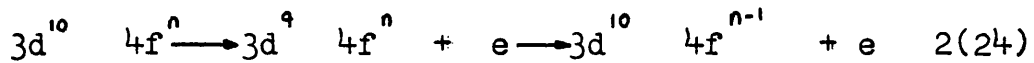


On the basis of the emission model for lanthanum, the emission structure should be given by a transition of the type represented by equation 2(22) which would give reciprocal m_s and m_α transitions. In the work of Parrott (1965) and Karnatak (1971) it was

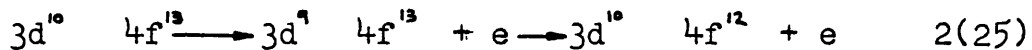
found the m_{α} structure was not simple but consisted of a principle line at 1520.0eV and a large overlapping high energy component. The principle line at 1520eV lies at the same energy as the m_{β} absorption and so can be assigned to a resonance transition of the type described by equation 2(22). Both Karnatak and Parrott found that the high energy component was voltage sensitive but a large discrepancy exists between the measured widths of the whole m_{α} structures. Karnatak recorded the $m_{\alpha,\beta}$ spectra of Yb_2O_3 and found the full widths at half maximum to be 13eV and 8.3eV for m_{α} and m_{β} respectively at 3.1 KV excitation, and 8.9 eV and 6.2 eV for m_{α} and m_{β} respectively at 1.8 KV excitation. In the case of Parrott, the m_{α} spectra of YbF_3 was recorded and the full width at half maximum was found to be 8.2eV, 6.9eV and 5.5eV at 3.0 KV, 2.0 KV and 1.8 KV excitation voltage respectively. There is obviously a very large discrepancy between these two results and it is interesting to note that in the work of Karnatak the Yb_2O_3 m_{β} absorption was measured and quoted to have a full width at half maximum of 2.8eV. This can be compared to the measurement by Combley, Stewardson and Wilson (1968) in which the width of the m_{β} absorption line was measured to be 1.7eV and the very high resolution work of Karnatak, Esteva and Connerade (1981) in which using a synchrotron radiation source and a double crystal monochromator the line width was measured to be 1.4eV. In this study the instrumental broadening was measured and when deconvolved gave a true line width of 1.2eV. The broadening in the work by Combley, Stewardson and Wilson was therefore 0.5eV and in the work by Karnatak, 1.6eV. In the work of Fischer and Baun (1967) the m_{α} line width was measured to be 5.8eV and the m_{β} to be 4.0eV at 1850eV excitation voltage. The m_{α} measurement seems to be in reasonable agreement with the work of Parrott (1965). An attempt was

also made by Parrott to measure the m_4 region for ytterbium, and although the spectrum was not reproduceable because of oxidation, the high energy satellites appeared to be greatly reduced with an associated decrease in linewidth. A reduction in linewidth was also noted by Karnatak to 11.2eV and 7.6eV at 3.1 KV and 1.8 KV excitation voltages respectively.

If the 3d electron which is promoted to the 4f level in a resonance excitation is instead ionised, then the following transition could occur,



This process would not be possible in lanthanum due to the empty 4f shell, but for ytterbium fluoride with a single vacancy in the 4f shell this transition could take place,



This transition would lead to a multiplet on the high energy side of the resonance excitation line. If a normal line absorption occurs in thulium either in metallic or compound form, then due to the two vacancies in the 4f shell, the following transition will occur,

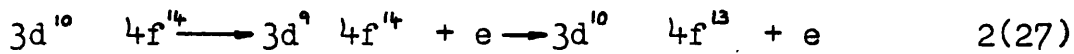


From equations 2(25) and 2(26) it can be seen that the initial and final states for an ionisation emission transition in ytterbium fluoride are the same as the final and initial states for line absorption in thulium or thulium fluoride. The thulium $m_{4,5}$ line absorption has been measured by Wilson (1978) and by Belrhmi - Belhassan, Karnatak, Spector and Bonnelle (1981) and has been shown to consist of a strong heavily overlapped m_5 structure in which there are three components which are just experimentally resolvable and a single m_4 line. The overall full width of the m_5 structure is 5.7eV and the m_4 single line is 3.0eV wide. The ratio of the integrated

intensities of the m_5 and m_4 absorption structures is 25:1 towards m_5 . For ytterbium fluoride, if a $3d^9 4f^{13} \rightarrow 3d^{10} 4f^{12}$ transition occurred after the ionisation of a 3d electron, then the resulting m_α and m_β structures would contain emission components that would reflect the thulium m_5 and m_4 line structures respectively. The ionisation and resonance emission transitions are competitive processes and so the m_α spectra would contain a single resonance line at the m_5 absorption energy together with three components from ionisation transitions at slightly higher energy. Similarly, the m_β structure should have a resonance component at the m_4 energy and an ionisation component at slightly higher energy. Cross sections for the complete ionisation of inner electron shells as determined by measurements of the intensity of x-ray lines as a function of voltage typically increase to a maximum value at several times the ionisation threshold. For electron excitation however, cross sections generally increase to a maximum value and then rapidly decrease. Absolute cross section data is only available for a few cases, mostly gases and little is known about core electron excitation functions (Massey & Burhop, 1952). However, it should be possible to observe the relative change in intensities of the ionisation and resonance components as the excitation voltage is changed. It would be expected that the lower energy resonance component would dominate at low voltages due to the high probability of resonance excitation near threshold and the relatively low probability of ionisation transitions as assessed from a comparison of the intensities of line and edge $m_{4,5}$ absorptions. As the excitation voltage is increased, the probability of resonance excitation would decrease sharply and so the ratio of ionisation to resonance transitions would increase. For the m_β structure of ytterbium fluoride the ionisation component should be relatively small and so on increasing the voltage, the ratio of ionisation

to resonance components should remain small even at high voltages, due to the resonance cross section decaying very rapidly near threshold to a fairly small value which then remains reasonably constant as the voltage is further increased.

As ytterbium metal has a complete 4f shell, only ionisation transitions should be possible.



The Yb_2O_3 m_5 absorption has been shown to be due to the transition,

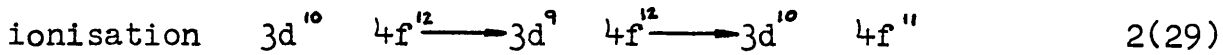
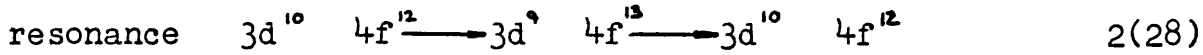


This is again the reverse of the ionisation emission in ytterbium metal. Using the same arguments as applied to ytterbium fluoride $m_{\alpha,\beta}$ emission, the m_{α} structure in ytterbium metal should show the same components as the Yb_2O_3 m_5 absorption which has been shown by Combley, Stewardson and Wilson (1968) and Karnatak, Esteva and Connerade (1981) to be a symmetrical single line well represented by a lorentzian with a full width at half maximum of 1.2eV. In this case, as no resonance transition is possible due to the full 4f shell, the m_{α} spectrum of ytterbium metal should consist of a narrow single component. As this is an ionisation transition, the line intensity should be only a slowly varying function of excitation energy.

In the case of lutetium, on the basis of the resonance and ionisation model, only ionisation transitions can take place due to the full 4f shell. The line structure should therefore be similar to that of ytterbium metal with simple single lines for the m_{α} and m_{β} structures. It would also be expected that the lines would be narrow as in the case of ytterbium metal. Again, as in the case of ytterbium metal, the lines should only be slowly varying functions of excitation energy as no resonance transitions can occur. In both cases of ytterbium metal and lutetium fluoride, any satellite transitions in doubly ionised atoms should be

observable due to the absence of high energy resonance transitions.

In the case of thulium metal and fluoride as there are twelve 4f electrons in both cases then the $m_{\alpha, \beta}$ spectra should be similar. In thulium the following transitions should make up the $m_{\alpha, \beta}$ structures.



The resonance components should therefore mirror the thulium $m_{4,5}$ absorption giving three components for m_5 and one weak component for m_4 . The components due to ionisation should give structure similar to the erbium $m_{4,5}$ absorption line structure,



Using the experimental $m_{4,5}$ spectrum of erbium measured by Stewardson and Wilson (1956) and the theoretical interpretation of Sugar (1972), the m_5 profile is found to consist of seven components, with two strong components and one weaker component making up most of the structure. The overall m_5 structure has a full width at half maximum of 5.6eV. The m_4 structure consists of three weak closely grouped components giving a full width at half maximum of 2.8eV. In the experimental spectra only three components are resolved for m_5 these being heavily overlapped and one component for m_4 . The ratio of the integrated intensities is 10:1 towards m_5 . The thulium $m_{\alpha, \beta}$ structure should be a combination of resonance and ionisation transitions with the ionisation transitions weighted towards higher energy. It can be seen therefore that in this case the m_β structure should be substantially narrower than the m_α structure. From this it also follows that both the m_α and m_β structures should be wider in thulium than in ytterbium fluoride. Due to the structureless nature of both the overlapped triplet m_4 absorption in erbium and the singlet m_4 absorption in thulium, the m_β emission

in thulium should be a simple shape with at most two resolved peaks, one due to resonance emission and one due to ionization emission. In the m_{α} spectrum, the three components for the thulium m_{β} absorption and the three resolved components for the erbium m_{β} absorption will overlap causing a broad structure with possibly several very weak emission features. In both m_{α} and m_{β} cases it is unlikely that high energy satellites will be visible due to the high energy resonance components.

2:4 Experimental requirements for recording rare earth $m_{\alpha,\beta}$ structures generated by electron bombardment.

Most recordings of the $m_{\alpha,\beta}$ spectra of the rare earths either have suffered from a high level of self absorption or in the case of the metals, from contaminated samples. In general the $m_{\alpha,\beta}$ absorption measurements have not suffered from the problem of sample contamination as the absorption foils do not have to dissipate any heat load. In x-ray emission, due to electron bombardment, even with good water cooling the surface temperature of the sample can still be very high. At high temperature the thin film will become more reactive and will quickly chemically combine. Most measurements have also used a direct line of sight electron bombardment from a tungsten filament. This can cause large amounts of contamination on the sample surface particularly if thoriated filaments are used to increase the emission current. The problem of self absorption has been discussed already and it has been shown that it is vital to reduce self absorption to a minimum if useful results are to be recorded. It is also important to know how much self absorption occurs even under minimised conditions so that corrections can be made. From an examination of absorption spectra, it can be seen that a resolution of better than 0.5eV is required, giving a resolving power of better than 3000 at the m_{α} line of

ytterbium. It has been shown in this chapter that it is necessary to be able to vary the energy of the electron beam so that structures due to ionization, resonance or satellites can be identified. The electron gun and the sample anode must also be rotatable so that the degree of self absorption can be altered. To prevent contamination from the residual vacuum, the sample should be deposited in situ by evaporation, and the best ultra-high vacuum conditions should be achieved.

These requirements dictated the design of the spectrometer described in chapter 3. The spectrometer used curved crystal focusing optics which were allied to an ultra-high vacuum sample chamber in which the samples were prepared by evaporation. The electron gun used a deflecting arrangement to prevent line of sight between the filament and the sample and was also rotatable between the sample normal and the sample surface. The sample target was water cooled and rotatable between zero and ninety degrees to the analysing axis. The whole spectrometer system was automatically controlled by a microcomputer which also handled the flow of data onto magnetic tape storage and to a mainframe computer.

Introduction	29.
3:1 Classification of Crystal Types.	30.
3:2 Corrections to the Bragg Law due to Refraction.	31.
3:3 Characteristics of Crystal Spectrometers.	31.
3:4 Theories of X-ray Diffraction by a Crystal.	33.
3:5 Choice of Type of X-ray Spectrometer.	34.
3:5:1 Plane Crystal Spectrometers	34.
3:5:2 Focusing Crystal Spectrometers	36.
3:6 Horizontal Focusing Spectrometers.	36.
3:6:1 Defocusing in Johann Geometry Spectrometers	37.
3:7 Choice of Geometry and Selection of Crystals for a Focusing Spectrometer.	41.
3:8 X-ray Wavelength Units.	42.
3:9 The Spectrometer.	44.
3:9:1 General Arrangement of the Spectrometer.	45.
3:9:2 Mechanical Arrangement of the Spectrometer Table.	50.
3:9:3 The Slit and Counter Mechanism.	53.
3:9:4 Mechanical Arrangement of the Crystal Chamber and Crystal Block.	55.
3:9:5 The X-ray Source Chamber.	57.
3:9:6 The Electron Gun and Power Supply.	60.
3:9:7 The Vacuum Metal Evaporator.	62.
3:9:8 The Spectrometer Vacuum System.	63.
3:9:9 Adjustment and Calibration of the Spectrometer.	64.

CHAPTER 3EXPERIMENTAL APPARATUSIntroduction

In the soft x-ray region of interest, around a wavelength of 7\AA , both gratings and crystals can be used as wavelength dispersing elements. Gratings are normally used in the vacuum ultra-violet region down to wavelengths of 20\AA , but in recent years with the production of gratings of complex shape and non-uniform grating density being made possible using holographic lithography, this wavelength limit has been reduced. In the wavelength region of interest the resolving power of crystals is much higher than that of the best available gratings and it was for this reason that a crystal dispersing element was chosen for the present study.

Crystal diffraction spectrometry is based on the Laue interference conditions for a three-dimensional point lattice, as expressed by the Bragg equation,

$$n\lambda = 2d \sin\theta \quad 3(1)$$

where d is the spacing of the atomic planes (h,k,l) which reflect the incident rays of wavelength λ at the Bragg angle θ (θ is the complement of the normal angle of incidence) and n being the order of reflection $1,2,3, \dots$. From the Bragg equation, if we have a polychromatic source of x-rays incident on a crystal, then the diffracted beam in a direction θ will consist of various wavelengths, $\lambda, \lambda/2, \lambda/3, \dots$, the

intensities of which are related to the structure factor of the particular reflection involved. For some reflections one of the orders of reflection can be dominant, such as the first order (100) reflection from mica, but in general many order reflections will occur and so if monochromatic radiation is to be selected from a continuous spectrum, (Bremsstrahlung, Synchrotron radiation) then either selective reflection at grazing incidence from metal surfaces or energy dispersive detection (proportional counter, solid state detector) must be used to eliminate higher order radiation.

3:1 Classification of Crystal Types

Four general classifications exist for x-ray diffracting crystals, the symmetrical and asymmetrical Laue and Bragg groups. If the incident and reflected rays are located on the same side of a semi-infinitely thick crystal and the reflecting planes are parallel to the external reflecting surface then this is the symmetrical Bragg case. The asymmetrical Bragg case occurs when the Bragg reflecting planes are not parallel to the crystal surface. In the Laue case, the incident and reflected rays are on opposite sides of the crystal, the diffracted beam being transmitted through the crystal. The condition for symmetry and asymmetry is the same as in the Bragg case. The Laue case is therefore limited to the short wavelength region where the absorption in the crystal would tend to be small. For the wavelength region of interest, the Bragg reflector was used as

absorption in the Laue case would have been too severe.

3:2 Correction to the Bragg Law due to Refraction

Although the Bragg law is valid inside a crystal, corrections must be made for refraction at the surface for the entrant and emergent rays. This is important for soft x-rays but can be corrected by rewriting the Bragg equation in the form (Cauchois and Hulubei, 1947),

$$n\lambda = 2d_n \sin \theta_n \quad 3(2)$$

where $d_n = d(1-T)$, λ is the wavelength outside the crystal, θ_n is the measured Bragg angle in the n^{th} order and T is a function of n and δ , where the index of refraction $\mu = 1 - \delta$. In the symmetrical Bragg case, T can be approximated by, (Compton and Allison, 1935)

$$T = \delta / \sin^2 \theta_n \quad 3(3)$$

where δ can be calculated using the classical expression (monoatomic crystal)

$$\delta / \lambda^2 = (e^2 / 2\pi mc^2) N f(0) \quad 3(4)$$

where N is the number of atoms per unit volume and $F(0)$ is the atomic scattering factor for radiation scattered in the direction of the incident wave. The term δ / λ^2 should be a constant for any given material except in the vicinity of absorption edges where it can vary. This effect is equivalent to anomalous dispersion in optics. The refraction effect is important in the soft x-ray region and is particularly important where calibration of a spectrometer is carried out using short wavelength x-ray lines recorded in higher orders.

3:3 Characteristics of Crystal Spectrometers

The dispersive power of a crystal spectrometer can be expressed either as an angular or linear dispersion.

Angular dispersion; $D(\theta) = \frac{d\theta}{d\lambda} = \left\{ \frac{1}{2d} \right\} (n/\cos \theta_n)$ 3(5)

The linear dispersion $D(L)$ is measured at the detector and depends on the geometrical arrangement of the spectrometer.

For a plane crystal spectrometer,

$$D(L) = \frac{dl}{d\lambda} = (L/2d)(n/\cos\theta_n) \quad 3(6)$$

Where L is the detector to crystal distance.

The resolving power, S , of a spectrometer is determined from the smallest wavelength separation of two adjacent spectral lines that can be resolved at the detector. If the spectrometer measured a truly monochromatic spectral line of wavelength λ , then the detector would see a broadened line $F(\lambda)$, the instrumental function or spectrometer spectral window. If $d\lambda$ is the width of the spectral window at half maximum, then the resolving power is,

$$s(\lambda) = \lambda/d\lambda = E/dE \quad 3(7)$$

The observed spectrum is therefore a convolution of the true spectrum and the instrumental function. The true spectrum can be deconvolved with a knowledge of the instrumental function although sufficiently accurate instrumental functions are only available for plane crystal spectrometers.

The flux at the detector is an important parameter in a crystal spectrometer. This is determined by the spectrometer geometry, the resolving power required and by the reflecting power of the crystal. If we define the reflection coefficient $R(\theta)$ of a crystal as the fraction of the total incident beam reflected in a direction θ , then we find that $R(\theta)$ is a very highly peaked function over a small range of θ . This defines the diffraction pattern of the crystal. The integral of the reflection coefficient in this peaked area is the reflecting power P ,

$$P = \int_{-\infty}^{+\infty} R(\theta) d\theta \quad 3(8)$$

The function $R(\theta)$ is only different from zero over a very small angular range allowing the use of $\pm \infty$ limits in the integration.

3:4 Theories of X-ray Diffraction by a Crystal

The first treatment of the diffraction of x-rays by a crystal was a geometrical theory termed the kinematic theory (James, 1954). The theory neglects absorption in the crystal and interactions between incident and scattered radiation and furthermore assumes that each reflected wave has only been scattered once. The kinematic theory is only appropriate where the volume of the crystal is so small that multiple scattering and absorption can be ignored. Although it is inappropriate for calculations involving large perfect crystals in reality crystals appear to behave as collections of small independent crystals with small variations in orientation with respect to each other. These crystals are termed mosaic crystals and their characteristics have been successfully calculated using a kinematic theory (James, 1954).

Where reflection from a large perfect single crystal is to be considered a more exact approach must be used. Dynamical crystal diffraction theories (Darwin, 1914; Ewald, 1916, 1917) which include descriptions of multiple scattering, when combined with models of absorption in the crystal, (Prins, 1930) can give accurate predictions of the width and shape of the diffraction pattern, percent reflection and reflecting power. Disorder caused by thermal agitation can cause broadening of the diffraction profile and is easily included in the Darwin Prins model, but for most crystals at room temperature the effect is small. Many crystals can be produced without mosaic imperfections (Silicon, Germanium) but on grinding or polishing a mosaic surface layer is created. This broadens the diffraction profile but can usually

be removed by acid etching the crystal surface.

3:5 Choice of Type of X-ray Spectrometer

In the soft x-ray region, reflection geometry has to be used due to the high absorption in the transmission mode at long wavelengths. The basic choice in design is therefore between a non-focusing plane crystal spectrometer or a focusing curved crystal instrument, both of which can be used with single or multiple crystal elements.

3:5:1 Plane Crystal Spectrometers

The simple single plane crystal Bragg spectrometer (Fig. 3:1) consists of a small or point source (X) collimated by a small aperture (S) so that radiation is incident on the reflecting crystal (AB) over a small angular range. In this arrangement, the detector (I) would have a small slit or aperture so that a line through the slit (CO) would define the angle COB which was always equal to the source crystal angle XOA. The energy resolution was simply dependent upon the angular acceptance of the crystal defined by the source X, slit width S and the slit to crystal distance, and the diffraction profile of the crystal. If a large source were to be used and high resolution was required, a further slit would be added (Sl) to define the angular acceptance. The angular dispersion can be given by,

$$D = \frac{d\theta}{d\lambda} = \frac{n}{2d} \frac{1}{\cos\theta} = \frac{\tan\theta}{\lambda} \quad 3(9)$$

The angular dispersion therefore increases with order n and becomes large at large Bragg angles. The definition of resolution by Allison (1931) is that two spectral lines are just resolved when their separation is equal to the full width of the instrumental window. If the instrumental window is (W) which is a convolution of the angular acceptance and the natural angular rocking width of the crystal, then from equation 3/9 the resolving power can be

given by,

$$\frac{\lambda}{d\lambda} = \frac{\tan\theta}{W} \quad 3/10$$

The resolving power is therefore high at large Bragg angles and with small instrumental window widths. The sensitivity of recording can be increased by using an extended source in conjunction with photographic recording as in Fig. 3:2. The angular range defined by the extended source and the slit gives a spectrum over a range of wavelengths. The auxiliary circle defines the following geometrical property.

$$\angle SOA = \angle SDO \quad 3/11$$

and as the points O and D lie on the auxiliary circle

$$\angle SOF = \angle SDF \quad 3/12$$

If the crystal is therefore rotated to a new position (BOD) the wavelength positions on the focusing circle (GE) remain unaltered. Although this appears to be a focusing method the focusing occurs at different times as the crystal is oscillated over some angular range. At any time there is only one point on the crystal D reflecting radiation of a particular wavelength to a point F. In this photographic method only a small fraction of the crystal surface around the point D is used to form a spectrum line at F. This area is defined by the entrance slit width and distance from the crystal and by the rocking width of the crystal. In the Soller spectrometer (Soller, 1924; Fig. 3:3) an extended source is used, radiation from which is collimated by a large number of parallel plates. The equal gaps that the array of parallel plates define set the angular resolution but because of the difficulty of making collimators with sufficiently small gaps the resolving power of a Soller spectrometer is always less than its Bragg counterpart. However, this type of arrangement can give a very high detector flux and has a resolution that is adequate for many applications and so is widely used in commercial

spectrometers.

The double crystal arrangement (Fig 3:4) can be used to achieve very high resolving powers, and has been extensively used for precision wavelength measurements (Bearden and Burr, 1967). However, although it is possible to obtain true widths of spectral lines corrected for the instrumental window, the optical aperture is necessarily very small. For the spectral features of interest in this present work, good optical efficiency as well as high resolving power was necessary.

3:5:2 Focusing Crystal Spectrometers

In focusing crystal spectrometers the reflecting crystal is usually bent into the form of a cylinder. If the entrance or exit slits are parallel to the cylindrical axis this is known as a horizontal focusing instrument and if the slits are perpendicular to the cylindrical axis this is known as a vertical focusing instrument. Horizontal and vertical focusing has been attempted using toroidally shaped plastically deformed crystals (Barreman, 1955) but although very high optical efficiencies have been achieved, the resolving power has so far been limited due to imperfect toroidal bending. Although several successful vertical focusing devices have been made (Kunzl, 1935; Van der Berg and Brinkman 1955) horizontal focusing instruments are normally used as their construction can be somewhat simpler

3:6 Horizontal Focusing Spectrometers

The most commonly used form of horizontal reflection focusing uses a geometry due to Johann (1931). A similar type of geometry was independently pioneered by Cauchois (1932) for transmission curved crystal spectrometers. In the Johann geometry (Fig 3:5), a crystal with the reflecting planes parallel to the optical surface is bent into a horizontal cylinder BAC

with a radius OA of R. If an auxiliary circle is now constructed with a radius of $R/2$ centred on X, then radiation of wavelength λ making an angle α to the tangents at points D, A and E on the surface of the bent crystal, will be approximately focused on the auxiliary circle at F. The Johann geometry does not give a true focus or a point to point image, but is an approximate focusing technique.

3:6:1 Defocusing in Johann Geometry Spectrometers

The extent of the horizontal defocusing can be calculated from Fig. 3:6. If firstly the central ray is considered, then it can be seen that if it is incident on the crystal at point A at an angle α and if the Bragg condition is satisfied, then it is reflected at an angle α to intersect the auxiliary circle (Rowland circle) at point F. The source is usually a broad source situated inside the Rowland circle. If the reflected ray is produced backwards and projected through the source, it would cut the Rowland circle at a point G. A point H can be taken at a distance along the Rowland circle which defines the symmetric opening angle of the crystal θ . A line OHC can now be drawn which intersects the crystal at its maximum aperture. The tangent T1, T2 can now be drawn at the point C on the crystal and a parallel line can be drawn at H so that as the angles OAG and OHG are equal angles, GHT3 and OHT4 are equal to the Bragg angle α . From this it follows that if the portion of the crystal at C could be transferred to a position at H without altering its angle, then the central ray and the ray reflected at H if of the same wavelength, would meet at F and form a true focus. If a ray of the same wavelength travels parallel to the incident ray GH and intersects the crystal at C, it will cut the Rowland circle at E near the mean focal point F. Thus, at any wavelength defined as a position along the Rowland circle,

there will be an effective broadening given by EF. The distance along an arc (L) from the centre of the crystal face (A) can be given by,

$$L = R\theta \quad \text{where } \theta \text{ is the Bragg angle} \\ \text{and } R \text{ is the crystal radius} \quad 3/13$$

If the Bragg equation is written in the form,

$$n\lambda = 2d \sin \frac{L}{R} \quad 3/14$$

this gives an expression for the inverse linear dispersion along the Rowland circle

$$\frac{d\lambda}{dL} = \frac{2d}{nR} \cos\left(\frac{L}{R}\right) = \frac{\lambda}{R} \cot\theta \quad 3/15$$

The horizontal broadening of monochromatic rays intersecting the Rowland circle given by the length FE can be calculated from a projection of the length CH. The monochromatic broadening W1 can be given by

$$W1 = CH \cot(\alpha - \theta/2) \quad 3/16$$

and expressing CH in terms of the lengths AC and AH gives,

$$W1 = ((2R \sin \theta/4)^2 - (R \sin \theta/2)^2)^{\frac{1}{2}} \cot(\alpha - \theta/2) \quad 3/17$$

$$W1 = 2R \sin^2 \theta/4 \cdot \cot(\alpha - \theta/2) \quad 3/18$$

Similarly, an expression can be derived for the broadening introduced by the crystal height H

$$W2 = \frac{H^2}{8R} \cot\theta \quad 3/19$$

A further broadening is contributed by the intrinsic diffraction pattern width. For the case of curved crystals however a complete dynamical description does not exist although kinematic theories have been proposed by Fock (1940) and Blackman (1951). The diffraction pattern also depends on the type and extent of the bending with some crystals exhibiting mosaic behaviour after formerly being perfect. Most experimental determinations of diffraction widths have been carried out for the transmission case, an example of which is a

measurement by Knowles (1965) on quartz, in which the intrinsic diffraction width of a few arc seconds was broadened to between fifteen and twenty arc seconds after slight bending. For the reflection case, an approximate treatment of the diffraction pattern for a curved crystal has been proposed by Senemaud (1963) based on an original model by White (1950). This model gives the linear width along the focal circle due to the diffraction width as,

$$W_3 = R\Omega + [(\cos\theta) 2\mu] \ln 2 \quad 3/20$$

where Ω the angular width of the domain of total reflection is an approximation such that the Darwin curve of the reflection coefficient is represented by a rectangle of angular width Ω giving an integrated intensity the same as for a perfect crystal. μ is the linear absorption coefficient and θ is the Bragg angle. Experimental results by Belin (1967) suggest that this approximate model is an adequate description of the diffraction profile for curved crystals. The second term in equation 3/20 can usually be ignored for soft x-ray reflections as absorption is negligibly small.

Further broadening can occur in curved crystal spectrometers due to mechanical misalignment. If the radius of the Rowland circle is not half that of the crystal radius, then the broadening of a line along the Rowland circle can be given by

$$W_4 = \theta |2r - R| \sin \theta \quad 3/21$$

where r is the Rowland circle radius.

Another broadening term can arise if the cylindrical axis of the crystal is not perpendicular to the plane of the Rowland circle. If the misalignment is given by the angle α , the broadening on the Rowland circle can be given by,

$$W_5 = H/2 \cdot \alpha \cdot \sec \theta \quad 3/22$$

In the worst case W_1 , W_2 and W_3 will be additive but W_4 and W_5 will be added in quadrature. If W represents the total broadening

on the Rowland circle, then this can be given by,

$$W = ((W_1 + W_2 + W_3)^2 + (W_4)^2 + (W_5)^2)^{\frac{1}{2}} \quad 3/23$$

With good alignment and mechanical design, the terms W_4 and W_5 can be reduced to negligible proportions. It is evident from equations 3/18 and 3/19 that if the Bragg angle is small then the geometrical aberrations due to the crystal aperture become very large, and that if the Bragg angle is near $\pi/2$ then the aberrations become very small. Protopopov (1948) has suggested because of this that if the crystal is cut so that the reflecting planes lie at an angle β to the optical surface (Fig 3:7) then it can be arranged that over a narrow wavelength range of interest, the angle of reflection to the optical surface can be near $\pi/2$, and so the geometrical broadening can be reduced to a very small value. Using this method the dispersion along the Rowland circle is unaltered but the spectral lines are shifted by 2β towards the centre of the crystal bending circle. Using this method, considerable enhancement of the resolving power can be achieved. It is obvious from the geometrical construction used in Fig 3:6 that if the crystal is bent to a radius R and the optical surface is then ground to a radius $R/2$ then perfect focusing can be achieved in the horizontal plane. This method of focusing (Fig 3:8) was proposed by Johansson (1933) and has been successfully used, although its use has been limited by the difficulty of preparation of the crystals and by the lack of suitable crystals having the correct properties for grinding and polishing. In the Johansson method, the W_1 term in equation 3/23 becomes zero, but all other terms remain the same. In the Johann and Johansson geometry, the detector flux compared to that in the Bragg method can be approximately given by the ratio of the horizontal curved crystal aperture to the Bragg slit width. This can typically

be several hundred for high resolution work.

3:7 Choice of Geometry and Selection of Crystals for a Focusing Spectrometer

A crystal selected for high resolution curved crystal spectroscopy must satisfy several conditions. It must have a high reflectivity for x-rays in the wavelength region of interest, the crystal spacing must be such that these wavelengths are reflected at suitable Bragg angles, it must be easily elastically bent and the plane crystal must have a narrow diffraction width which must not greatly increase after bending. Table 3:1 gives a list of commonly used diffraction crystals for plane and curved crystal spectrometers.

The approximate range of the $M_{\alpha, \beta}$ lines of thulium, ytterbium and lutetium is from 7.5 \AA to 8.5 \AA . From the Bragg equation it can be seen that the wavelength must be less than twice the lattice spacing of the particular reflecting planes of the crystal, and so from Table 3:1 that quartz ($10\bar{1}0$), PET(002), EDDT(020), ADP(101), gypsum (020), mica (002) and KAP are suitable. The soft synthetic crystals PET, EDDT, ADP and KAP are generally unsuitable for bending as they tend to undergo permanent plastic deformation as well as elastic bending. Quartz ($10\bar{1}0$) could also be eliminated as for the long wavelength end of the region a Bragg angle of eighty six degrees would be required, bringing the detector and source too close together.

This leaves only gypsum and mica as suitable crystals and neither of these can be ground as well as bent, as in the Johansson method. This also unfortunately eliminates the use of inclined crystal planes for the reduction of horizontal geometrical broadening in this wavelength range. The imperfect focusing technique based on the method of Johann was therefore used for the present study, but care was taken to minimise the

defocusing effects outlined in section 3:6:1, while still giving a reasonable optical efficiency.

3:8 X-ray Wavelength Units

X-ray wavelengths were originally calculated directly from the Bragg equation using a value for the spacing between reflecting planes derived from a knowledge of the density of the crystal, Avagadro's number and the reflection crystallography. Siegbahn (1919) suggested that an arbitrary wavelength standard based on the lattice spacing of sodium chloride should be used such that the lattice constant could be represented by 2814.00 units at 18°C. This unit was known as the XU and allowed comparative measurements to be made accurately in different laboratories. This was needed due to errors associated with the original measurement of the spacing between reflecting planes. The original sodium chloride standard was replaced by a new standard based on the lattice spacing of Icelandic calcite as the lattice constant of sodium chloride was found to be variable and the diffraction width was very large giving poorly resolved spectral lines. The lattice constant in this case was represented by 3029.04 X.U. at 18°C (Siegbahn, 1933). When measurements of x-ray wavelengths became possible with ruled gratings (Bearden, 1931, A) it was found that wavelengths measured using crystals were always 0.2% lower than those measured using gratings due to an error in the value of Avagadro's number. The wavelength scales were brought into agreement by a redefinition of the lattice spacing of calcite to be 3055.6 X.U. (Bearden, 1935). The calcite X.U. standard contained the flaw that it assumed that lattice constant did not vary between crystals. Bearden (1931, B) measured differences in lattice constant of the order of ten parts per million between different crystals and proposed that a new standard based on the wavelength of the tungsten K_{α} line be

used. The wavelength of this line was given as 208.5770 X.U. Tungsten was used, as the K_{α_1} line is symmetrical, narrow shows no chemical or isotopic effects, and is accessible to both the gamma-ray and x-ray regions. As an x-ray anode, tungsten can also withstand extreme power loading. Bearden (1967) calculated the conversion factor for X.U. on the tungsten scale and obtained a mean value of $1.002076 \pm 0.00005 \times 10^3$. This meant that the tungsten K line could be given as 0.2090100 \AA^* where \AA^* was the new unit of wavelength, but that \AA^* could differ from $\overset{\circ}{\text{\AA}}$ by up to 5 parts per million. Secondary standards were defined using Ag K_{α_1} , Mo K_{α_1} , Cu K_{α_1} and Cr K_{α_1} and from these most of the wavelengths of the diagram lines of the elements were established on the new absolute scale.

Table 3:1 Commonly used Crystals in X-ray Spectroscopy

<u>Material</u>	<u>Reflection Plane</u>	<u>$d(\overset{\circ}{\text{\AA}})$</u>
Ge	220	2.000
Si	220	1.920
	111	3.138
Calcite	211	3.035
Quartz	$11\bar{2}0$	2.458
	$10\bar{1}1$	3.343
	$10\bar{1}0$	4.260
Graphite	0002	3.35
PET	002	4.37
EDDT	020	4.401
ADP	101	5.320
Gypsum	020	7.59
Mica	002	9.947
KAP	100	13.85

The special problems associated with recording undistorted spectra of the heavy rare earths have been discussed in Chapter 2. The need to record weak overlapping components dictated the choice of curved crystal geometry in order to obtain both adequate resolution and a reasonable data rate. The reactive nature of the rare earth metals required the use of an ultra high vacuum sample environment and in situ sample preparation (Karnatak, 1971). To prevent contamination or alloying from the filament of the electron gun used as an excitation source, a method was developed in which electrons from the filament source were deflected through a small angle and focused into a horizontal line on the sample so that there was no direct line of sight from filament to sample. As discussed in Chapter 2, a knowledge of the dependence of spectral features on both the x-ray take-off angle and the electron incidence angle can lead to an elimination of self absorption effects. This is of particular importance in the rare earths where the $M_{4,5}$ absorption lines overlap in energy the $M_{\alpha,\beta}$ emission lines. The design of the ultra-high vacuum (UHV) sample chamber and electron gun allowed a full range of incidence and emission angles to be used by in situ movements of the electron gun and sample. The need for UHV sample environment required the development of a novel spectrometer arrangement in which the low vacuum spectrometer section was coupled to the UHV section by a rotatable vacuum vessel which contained the crystal. This alleviated the need for a completely UHV instrument, with only a small fraction of the total spectrometer vacuum system being pumped to high vacuum. This greatly reduced the cost of the instrument. Detection of x-ray photons was carried out using a new simple design of low noise proportional counter and throughout the design of the detection system special attention was paid to keeping noise levels to an absolute minimum whilst maximising

the detected signal. The design required the electronic coordination of the positions of the counter, crystal and x-ray source and so a motor system controlled by electronic interfaces and a micro-computer was developed. This was also used to automate the collection of data, record data on magnetic tape and transmit data to a central computer for rapid treatment and analysis. The system allowed several data collection and control algorithms to be used depending upon the experimental conditions encountered and was designed to be easily hardware extendable so that it could control other devices such as the electron gun or vacuum evaporator.

The spectrometer system was designed specifically to look at x-ray emission spectra from reactive metals in which it was expected that very low count rates would be encountered. This required that all the optical components, the source, crystal and detector were fully optimised and matched together and sources of noise reduced to a minimum. Because the system operated under computer control, it was possible to extend the geometrical range of the instrument and operate it under a wide variety of conditions from a wide wavelength range survey instrument to a high resolution line profile spectrometer. The physical arrangement of the external sample preparation facility allowed the possibility of investigating a wide variety of sample types, such as liquid metals, with only minor modifications. The complete computer control and data acquisition system is described in Chapter 4.

3:9:1 General Arrangement of the Spectrometer

The arrangement of the spectrometer was dictated by the need for an ultra-high vacuum sample target environment and a simple way of recording line shapes. From Fig. 3:5 it can be seen that the simplest method of scanning a spectral line would be to have the source at S on the Rowland circle and the detector at

the imperfect focal point F, also on the Rowland circle. When scanning wavelength the source S and the detector F would both move together such that the angle SAO equalled angle FAO with both source and detector on the Rowland circle. In this case the crystal would remain fixed. To record accurate line profiles, it is not desirable that the source and detector move together, as inaccuracy in the tracking mechanism can cause large changes in the observed profile. Over a fairly small wavelength region this can be overcome by having an extended source emitting uniformly over its surface, located so that the centre of the source approximately corresponds to the Bragg angle for the centre of the line profile to be examined. (Fig 3:6). The disadvantage of this method is that as the crystal is fixed, the vacuum chamber containing the source, detector and crystal would become very large if a reasonable wavelength range were to be covered. The geometrical arrangement of the present spectrometer is given in Fig. 3:9. The principal advantage of this geometry is that over a reasonable wavelength range, only the detector has to move and that if an adjacent wavelength region is to be scanned, then the crystal is moved to a new angle and the corresponding section of the Rowland circle is scanned by the detector. The design is therefore not continuously scanning throughout its wavelength range, but partitions it in such a way that the spectrometer mechanism becomes a reasonable size. The disadvantage of this method is that it relies on the broad x-ray source situated inside the Rowland circle giving even emission over its surface. If the source does not give even emission the line profile can be badly distorted. The use of a broad source over a point source situated on the Rowland circle has the advantage however of being able to allow much higher total power levels and consequently higher detected flux. The effect of moving the source away from the Rowland circle has been investigated theoretically and

experimentally (Didsman, 1961) and suggests that in this case many times more flux can be generated from the broad source situated between the crystal and the virtual point source on the Rowland circle than for a true point source.

For a particular crystal setting the counter moves along a small section of the Rowland circle from its mean position at D3, D2 or D1. These correspond to the crystal settings C3, C2 and C1 respectively and are generated by constructing a Rowland circle for each crystal angle and leaving the chord OD fixed. The length of OD is given by,

$$OD = R \sin \theta \quad 3/24$$

where θ is the Bragg angle and R is the crystal radius

This arrangement always gives equal angles at the detector mean position and the crystal such that

$$\angle TDO = \angle COD \quad 3/25$$

The number of positions needed along the chord OD is dictated by how wide the region of even illumination along the Rowland circle is, given by the extent of the broad source. The spectrometer was arranged so that in the wavelength region covering the $M_{\alpha, \beta}$ lines of thulium, ytterbium and lutetium, the crystal position did not have to change, giving very simple operation. The arrangement of components within the spectrometer is shown in Fig. 3:10. The length of the arc chosen was such that at the maximum chord length allowed, the broad source would illuminate approximately one quarter of the arc. The arc was followed by machining a section of the Rowland circle and mounting the detector on a block which was spring loaded against the machined arc. The detector mount also had a small portion of the Rowland circle machined into it. This arc could be rotated about its mean position on the chord (OD, OE) to satisfy equation 3/25 and moved along the chord (OD, OE) to satisfy equation 3/24. When the crystal, arc angle and chord were set so that the region

of interest was near the mean position of the arc (E,0), then the profile could be scanned by moving the counter along the arc.

The detector used was a proportional counter (Chapter 4), the wavelength window on the Rowland circle being defined by using an adjustable slit in front of the counter window. From Fig. 3:10 it can be seen that as the counter is traversed along the Rowland circle, the direction of the slit has to be continually altered to allow the counter always to face the crystal. The construction of the counter was such that over the narrow wavelength regions covered by an $M_{\alpha,\beta}$ doublet, the sensitivity of the counter did not change if it was fixed in a correct mean position. This was due to the fairly large counter window which allowed a wide interaction region. Traversing from one end of the arc to another required adjustment of the rotation of the counter and this was done by mounting the counter on a geared down stepper motor. The position of the counter along the Rowland circle and measured using an electrical micrometer, but the rotation of the counter had no associated measurement system. The counter once set to its correct angle was kept pointing at the crystal by rotating the correct amount calculated from the displacement from the set point along the Rowland circle and from a knowledge of the mean Bragg angle. The microprocessor control system (Chapter 4) controlled this relation so that once a set point had been established, the counter always faced the crystal centre. The control system also included an algorithm which rotated the counter until a maximum count was established and then found the angular range over which this maximum was constant within set limits. This was initially used to define the calibrated set point. A sufficiently accurate angle measuring system could not be used for the counter rotation as the rotation mechanism had to be very light and small and no commercial unit could be found.

The position of the Rowland circle arc along the optical axis and the angle of the arc to the optical axis were externally adjustable and were driven by geared down a.c. motors. The position and angle of the Rowland circle arc were measured using simple rotating disc light choppers which were calibrated from internally calibrated set points. The control of the motors and measurement of the positions is fully described in Chapter 4. The angle of the crystal tangent to the x-ray source was always kept equal to the angle of the crystal tangent to the optical axis. This was done by pivoting the x-ray chamber about the crystal centre and using a similar control system to that used for movement of the Rowland circle arc. To allow this movement, the crystal was supported on an arm attached to the main spectrometer table and the crystal chamber was simply a low vacuum extension of the ultra-high vacuum x-ray chamber which articulated with a cylindrical vacuum joint which was connected to the main spectrometer tank. The separation of the ultra-high vacuum system from the spectrometer low vacuum system was by a thin self supporting polypropylene window five microns thick. The whole x-ray chamber pumping system and ancillary apparatus was designed to rotate about the crystal centre. The x-ray chamber was pumped to ultra-high vacuum by a liquid nitrogen trapped diffusion pump and could readily reach pressures of 2×10^{-10} Torr after a 120°C bakeout. The chamber contained a water cooled anode which could be moved from zero to ninety degrees with respect to the crystal centre and a high intensity electron gun which could be moved between zero and ninety degrees to the surface normal. This movement was designed so that self absorption effects in the target material could be investigated and eliminated. The UHV chamber also included a clean metal evaporator and a crystal microbalance to determine evaporation rates. The crystal

could be externally rotated by a motor and the angle of the crystal from a set point was measured using an optical fringe counting technique.

To give acceptably large dispersions along the Rowland circle, a one metre curved crystal was used and to give a reasonably large wavelength range at one crystal setting, an arc length of 180 millimetres (mm) was used. In accordance with the minimisation of defocusing in the Johann case (Chapter 3:6:1), a crystal aperture five millimetres high by twelve millimetres wide was used. The width of the detector slit used for most work was 0.09 mm which corresponded to a broadening of 0.2 eV at the ytterbium M_{α} emission line using a gypsum crystal. Gypsum was used in preference to mica as it gave more convenient Bragg angles for the present study. Due to the unsuitability of gypsum for two crystal spectrometer measurements, no rocking width data exists and so the energy broadening due to the diffraction window could not be estimated. The diffraction width could only be estimated by setting the crystal aperture to a small value and observing the width of a well characterised line profile (characterised using a two crystal spectrometer) as a function of exit slit width. The electrical micrometer covering the full 180 mm range of the Rowland circle arc was linear to 0.005% and its output was digitised using an absolute accuracy twelve bit analogue to digital converter giving a true resolution of one part in approximately four thousand. This gave a spatial resolution of 0.045 mm or 0.1 eV at the ytterbium M_{α} line.

3:9:2 Mechanical Arrangement of the Spectrometer Table (Plate 1)

Plate 1(3) shows the general arrangement of the spectrometer table. The main feature of the design is the mounting of the crystal turntable on a long arm which was bolted to the spectrometer table. As shown in Plate 1(1), this allowed the crystal

turntable to be positioned at the centre of the crystal chamber but to be completely independent of it. Plate 1(4) shows the Rowland circle arc machined into a piece of heat treated high stability stainless steel. In Plate 1(4) the counter mechanism has been removed but can be clearly seen in Plate 1(2). In Plate 1(4) it can be seen that the counter was driven along the Rowland circle arc by a long ground stainless steel rod which was moved perpendicular to the rod axis by a leadscrew. The leadscrew was driven by a Mullard Slo-Syn motor through a Muffet 100:1 reduction gearbox, the leadscrew itself having thirty three threads per inch. The precision motion of the actuating bar was obtained by coupling the leadscrew nut to a precision balance bar arrangement in which a honed phosphor bronze bore passed over a ground high carbon steel rod. The honed bore, the leadscrew nut and the actuating bar were mounted in a single aluminium block. The position of the actuating bar was measured by mounting a ground stainless steel bar at a small angle to the balance bar on top of the aluminium block and using an electrical micrometer mounted at a right angle to the stainless bar to measure displacements from an initial set point. The inclined bar was used to give a more compact mechanical arrangement. The relation of the electrical micrometer output to the set point position was made by a precise mechanical measurement of the position of the driving edge of the actuating bar along the Rowland circle arc. The operation and decoding of the electrical micrometer is described in Chapter 4. Extensive tests of the reproduction of the actuating bar positions after a random movement gave an average error of ± 0.01 mm. In normal operation, the spectrometer scanned in one direction in small steps so that the positional precision of the counter slit would have been greater than after the random orientation test. The plate on which these components were mounted was made of a heat treated high stability aluminium alloy

(HP 30 WPS) which was ground and lapped to provide a good sliding surface for the counter to travel over. This plate was mounted on a second aluminium plate which could pivot about a bearing in the main baseplate. The top plate was adjustable so that the rotation axis could be accurately positioned on the Rowland circle arc and to allow for small deviations from the desired Rowland circle radius due to incorrect bending of the crystal. The fixed base plate and the second rotating plate were separated by precision ground cast iron plates lubricated with high vacuum oil. The bearing was a large plain type consisting of a hardened and ground pin rotating in a fixed phosphor bronze bush. The two components were lapped together and less than 0.005 mm side play could be measured. The drive for this rotation was carried out using a phosphor bronze worm and wheel arrangement, the wheel being mounted to the bottom of the moving pin and the worm being mounted on the base plate. Rotation of the table was measured at the worm by a rotating disc light chopper. The rotation was always initiated by first rotating back to a precision knife edge microswitch which was mounted on the base plate. At the other extreme of movement an override microswitch prevented possible mechanical damage caused by overrunning. All rotary devices were fitted with aluminium shear pins in case of a failure in the automatic system. The operation of the automatic motor control and measurement system is described in Chapter 4. The baseplate could move along the optical axis of the instrument supported on a vee and flat arrangement travelling along ground stainless steel rods mounted on the spectrometer table. The drive was provided by a Myford precision leadscrew and adjustable split nut mounted on the base plate which was driven by an external a.c. motor connected through the vacuum tank wall using a rotating wilson seal. Flexible couplings were used inside and outside the tank for this motion. A precision microswitch, an override microswitch

and a rotating disc light chopper were again used in the positional measurement system (Chapter 4). The drive for the rotation of the Rowland arc table also used a similar measurement system and an a.c. motor external to the vacuum tank. As the base plate could move along the spectrometer tank, the drive coupling to the worm and wheel arrangement also had to have a moveable drive connection which was provided using a sprocket keyed onto a rotatable shaft mounted on the spectrometer table (Plate 1(2)). This sprocket was connected to the worm drive by an adjustable chain. The rotatable shaft was coupled to a wilson seal shaft drive at one end of the tank by a sprocket and chain connection (Plate 1(1)). The spectrometer was fitted inside a close fitting rectangular vacuum tank and its attitude could be adjusted using a three point kinematic mount.

During the course of an experiment, after calibration using emission lines of well defined wavelength, the rotation and translation of the Rowland circle arc was left fixed, the crystal angle was fixed, the source was fixed and only the counter traverse moved. The accuracy and repeatability of the spectrometer, over the fairly narrow range of wavelengths used in line profile mapping only therefore depended on the accuracy of detector motion which has been shown to be much smaller than the total energy resolution due to crystal effects. This arrangement is therefore particularly suitable in experiments involving multi-scanning wavelength segments in an effort to eliminate non-random noise.

3:9:3 The Slit and Counter Mechanism

A gas flow proportional counter shown in Plate 3(1) was used to detect the x-ray photons and is described in Chapter 4. As mentioned previously the counter was collimated by a vertical

adjustable slit, the orientation of which had to be adjustable, as shown in Fig 3:10, as the counter scanned along the Rowland circle. The adjustable slit was mounted on a small table which had a plain pin bearing positioned below the slit axis. The pin bearing had a small hole through its centre so that the bottom of the slit could be viewed and centralised. This was done using a crosswire and a microscope to view the slit whilst rotating the slit assembly and it was possible using this technique to obtain an eccentricity of less than 0.02 mm. The bearing pin rotated in a honed bore, the table itself being guided by this and supported on four ground PTFE pads. The rotary drive for the counter table was from a geared down stepper motor which was connected to the pin bearing by a loose offset pin and hole coupling. Two simple microswitches were used to prevent possible overrunning and damage. The stepping motor was connected through a multi-way feedthrough in the vacuum tank wall to the microcomputer system. The whole assembly was mounted on a small cast iron block which had a section of the Rowland circle ground into it. This block and the stainless steel arc were ground and lapped together to a good optical finish. The base of the block had three small PTFE pads recessed which were machined together with the base of the stainless steel arc by surface grinding. In operation the counter block was spring loaded onto the arc by a long spring mounted off a short lever arm on the counter block and fixed at the other end on a pivot point towards the centre of the Rowland circle. As described before, the counter block was moved along the arc by a long ground stainless steel rod which pushed against a vertical ground steel pin. The counter slit body had two alignment holes equidistant from the slit centre which were used to align the crystal perpendicular to the optical axis using a laser. The slits themselves were manually adjustable, the slit gap being set using a feeler gauge.

3:9:4 Mechanical Arrangement of the Crystal Chamber and Crystal Block

Plate 2 shows the arrangement of the crystal block in the crystal chamber and the articulated vacuum joint. As previously described, the crystal block was mounted on an extension of the main spectrometer table and was completely independent of the vessel around it. Plate 2(3) shows the crystal block and scale and Plate 3(3) shows a breakdown of this into its component parts. The crystal block itself consisted of two halves, one with a concave cylindrical surface and one with a matching convex surface. The section with the convex cylindrical surface had an aperture approximately 8 mm high and 20 mm wide machined into it. The two blocks were lapped together to form an optically smooth surface. The two blocks were clamped together by four screws which held the gypsum crystal in place behind the rectangular aperture. The thin gypsum crystal was very lightly ground on its non x-ray reflecting surface and dyed black to eliminate reflections from the back surface during optical alignment. Extreme care was taken to avoid trapping dust between the convex and concave surfaces as these could severely alter the crystal focus. The quality of focus could be optimised by adjusting the tension of the clamping screws. The crystal mount in which the crystal block was held had tilt adjustments for both the saggital and meridian planes and allowed movements of $\pm 5^\circ$ in both directions. The crystal mount was itself attached to a graduated scale which could be read with an associated vernier mounted off the main support arm. The crystal mount could be moved by a geared down motor mounted directly beneath the crystal chamber. The connection was made through the base of the crystal chamber using a rotary shaft wilson seal. Inside the crystal chamber, the connection to the crystal mount was made by a loose off axis peg arrangement which although allowing smooth forward rotation was not mechanically connected

to the crystal mount. Movements of the crystal chamber and crystal block were therefore fully independent. The angle of the crystal to the optical axis was measured using a radial grating shaft encoder (Plate 4) and is described in Chapter 4. The encoder was highly stable and being an incremental encoder had a battery back up in case of a power failure. The encoder was calibrated so that zero corresponded to the crystal being perpendicular to the optical axis. Plate 2(1) shows the arrangement for coupling the shaft encoder and crystal mount. The coupling rod could be inserted into a spring clip arrangement in which the spring pressed the rod into light contact against a ground steel plate. The crystal and the encoder were therefore always rotated by the same amount. The radial grating encoder output was decoded as described in Chapter 4 and was connected to part of the micro control system. To keep the mean Rowland circle arc to crystal tangent angle the same as the x-ray source to crystal tangent angle, the crystal chamber connected to the x-ray chamber had to be able to rotate about the vertical crystal axis. This was done by mounting the x-ray chamber and its associated equipment on a carriage which rotated about a pivot point directly underneath the crystal. The shaft which rotated the crystal passed directly through the centre of this pivot point which used a plain steel pin and phosphor bronze honed bearing mounted in the rotatable carriage. The carriage itself was mounted on three large steel wheels which moved on a cast iron base plate, the base plate being kinematically mounted and laterally adjustable to allow the rotation axis to be positioned on the optical axis of the spectrometer. The optical axis was defined as a line running parallel to the spectrometer rails passing through the centre of rotation of the detector table. The drive for the carriage was by a leadscrew driven from an ac motor mounted on a vertical pivot point engaging with a pivot nut mounted on

the carriage. The rotation measurement and control was the same as for the counter table traverse and rotation, using a rotating disc light chopper and microswitches connected to the motor control system. Plate 2(2) shows this arrangement, although the ultra high vacuum pump arrangement has been removed for clarity. The ultra high pumping stack extended downwards through the circular gap visible in the cast iron base plate. To allow this rotation, the crystal chamber had to have an articulating vacuum joint to the spectrometer tank. The assembled arrangement can be seen in Plate 2(1) and the component parts can be seen in Plate 2(4). The crystal chamber had a large rectangular hole in it to accommodate the diffracted x-ray beam and the crystal mount support arm, this being surrounded by an O-ring seal machined into the chamber wall. The chamber engaged with a matching cylindrical shoe lined with PTFE which was connected to the vacuum tank through a large bellows. The two halves were forced into hard contact by a tensioned steel tape mounted on the shoe and passing around the chamber. The tape was kept out of contact with the crystal chamber by a further small PTFE lined cylindrical shoe. During rotation of the assembly, the shoe was prevented from rotating by pegs mounted on the shoe engaging with holes in an extension piece mounted from the spectrometer tank. This type of vacuum joint was found to be extremely reliable due to the use of PTFE sliding surfaces and during rotation no vacuum leak could be detected throughout the course of the work.

3:9:5 The X-ray Source Chamber

The x-ray source chamber is shown in Plate (5(1)). The source chamber was of all stainless steel construction using where possible standard conflat components. The chamber contained

the x-ray source comprising a moveable water cooled anode and a separate moveable electron gun, an ultra high vacuum metal evaporator and a quartz crystal film thickness monitor. The high vacuum source chamber was connected to the low vacuum crystal chamber by a five micron thick polypropylene window which was mounted on a conflat copper gasket. The window area of the source chamber was water cooled to prevent damage to the window material during bakeout of the vessel. The window could be valved off from the crystal chamber using a VAT gate valve, the interspace between the valve and window being pumped from the diffusion pump backing line. The pumping of the chamber was by a liquid nitrogen trapped CCT style Edwards E02 diffusion pump using Santovac 5 polyphenyl ether oil. The pressure in the chamber was measured using a Bayard-Alpert type of ionisation gauge. To achieve ultra high vacuums, the chamber was baked for over twenty hours at 120°C and whilst still at temperature the electron gun, sample target, evaporator and ion gauge were degassed. To degass the sample target the water cooling to the target was switched off and the electron gun was run at low current. The target was allowed to reach temperatures of over 1000°C and was kept at this temperature for several hours until the bakeout was switched off and the vessel allowed to cool. After this preparation and using liquid nitrogen in the trap a pressure of 2×10^{-10} Torr could be reliably achieved with the electron gun off and a pressure of less than 5×10^{-10} Torr with the electron gun running after many hours of degassing. The estimated pumping speed at the vessel was fifty litres per second for a vessel volume of three litres. As the source chamber and pumping system rotated with the crystal chamber the backing line was made of a section of convoluted flexible tubing. The backing line contained a bakeable foreline trap and was of all stainless steel bakeable construction. The x-ray source including the target and electron gun could be

removed and a separate O-ring sealed x-ray gun could be mounted inside the chamber on an aluminium lid. The x-ray gun was completely sealed having a thin melanex x-ray window and had it's own external diffusion pumping system. The rest of the volume of the x-ray chamber was pumped by the permanent diffusion pump, but the vessel was never baked in this configuration. The x-ray gun was a very simple copper water cooled target direct filament bombardment type and was used for generating calibration lines. To generate calibration lines it is usual to make a paste in alcohol or water of the materials to be used and then paint it onto the target surface. This is a dirty process and would have contaminated the UHV environment if a separate medium vacuum x-ray source had not been used. When calibration was complete, the x-ray gun was removed and the normal UHV anode and electron gun replaced it. The calibration x-ray gun gave emission currents of up to 250 mA at 17 KV and gave very intense calibration line profiles.

The geometry of the sample target is shown in Fig. 3:12. The target was made of stainless steel with the emitting surface ground and polished to a very good optical finish with diamond paste. This was welded onto the main target support bar which had a small water cooled resevoir at the back of the target area. Relative to the x-ray window port, the entire assembly was rotatable between zero and ninety degrees, this requiring that the water in and water out pipes had to be wound as counter spirals from 1.5mm bore stainless steel capillary. Internal connection of these pipes was by miniconflat flange connections. The target and electron gun geometry is shown in Plate 5 (2) and 5(3). The rotary motion of the x-ray target was actuated by a wobble stick pressing against a ratchet mechanism inside the vacuum system which gave five degrees motion for every ratchet notch. The electron gun was mounted off a swinging arm which

was pivoted at either end of the target and along a line passing across the centre of the target. Electrical connections from the electron gun were made using standard insulated vacuum feedthroughs and attached using copper braid insulated with ceramic fish beads. As shown in Fig 3:12, the electron gun could rotate through ninety degrees so that at one extreme electrons were at a slight grazing angle and at the other were impinging normal to the surface. This movement was actuated using a wobble stick by pushing against a notched arm attached to the electron gun swinging arm. A calibrated scale was marked on one end of the pivot bearings, so that the angle of incidence could be read through a window.

3:9:6 The Electron Gun and Power Supply

As stated previously, it was essential that for x-ray emission work on the reactive rare earth metals that all precautions should be taken to ensure a clean surface. One source of contamination of the sample surface in x-ray emission experiments is usually the filament electron source in the electron gun used to excite the x-ray emission. For higher electron energies this can be overcome by extracting the electrons from a filament over an optical shield and onto the target, the shield and filament usually being circular. For energies less than 5 KV this gives very low extraction efficiency and hence beam current and was therefore unsuitable for the present study. Plate 6 shows the arrangement used in the present study. Electrons were generated by thermionic emission from a single hairpin loop filament. (Plate 6(2)). The filament was sunk into a trough (grid) which was biased slightly negative with respect to the filament and the filament was held at the desired electron energy with respect to earth. Electrons were thus repelled from the trough and accelerated as they approached an earthed anode close to the front edge of the grid. The filament was held in position in the grid by mounting the loop end of the filament on a slider which was

tensioned by a small stainless leaf spring. (Plate 6(4)). The two ends of the filament were held by two large isolated copper blocks. The connections to the blocks were made by clamping the filament wire between sandwiches of tantalum foil. The filaments were made from 0.01 mm thoriated tungsten. After passing through the anode aperture, the electrons were deflected by a pair of parallel plates which were curved through a sector of sixty degrees. The inner plate was held at earth potential and the outer plate at an adjustable potential which was found to be approximately two thirds of the filament potential. On leaving the deflecting sector, the electrons passed through an earthed aperture before impinging on the earthed sample plate. The electrodes were made of molybdenum and stainless shim which were folded to shape and clamped together, isolated by 1 mm thick ground ceramic sheets and washers. Plate 6(2) shows the gun with the deflectors and exit removed for clarity and shows the arrangement of the grid, anode and filament. Plate 6(3) shows the individual component parts of the gun. A schematic circuit diagram of the electron gun power supply is given in Fig 3:13. The arrangement allowed the earth return current to stabilise the filament current and so stabilise the emission of the gun. It was possible to look at the loss currents in the gun due to electrons hitting the various focusing electrodes and so by adjusting the control voltages it was possible to minimise these losses. The performance of the electron gun was tested in a separate vacuum system and the sample target was replaced by an insulated one millimeter thick molybdenum plate. At sufficiently high emission currents the plate glowed bright red, and an estimate of the focal quality could be obtained from the shape of the glowing spot. An attempt was made to predict the behaviour of this type of electron gun using a finite elements method computer calculation using a relaxation method. (Hornsby, 1963). The program modelled the

behaviour of electrons for low current beams in the electron gun, but for high currents the behaviour of the gun appeared to be governed by space charge effects. The complexity of including space charge effects into the computer model meant that the basic model was only of limited use. An apparent effect of high space charge could sometimes be seen in the gun causing the electron beam size to slowly grow and then start to oscillate with a period of a few seconds. This usually happened when the gun was not sufficiently well outgassed possibly causing the formation of a large ion current. If the oscillation became too big the electron beam would strike an electrode and cause damage, an example of which is the final exit aperture in Plate 6(3). Once sufficiently degassed, the emission current and beam position were very stable giving beam currents of up to 100 mA between 1 and 5 K.V. beam energy. The gun was of UHV construction throughout and did not allow line of sight between the filament and the sample. In operation with the water cooled target the pressure was less than 5×10^{-10} Torr if the power level was kept beneath 75 Watts. If this power level was exceeded then the pressure rose rapidly due to the production of steam in the anode reservoir. The cooling rate was badly limited by the need to use small capillary pipe inside the vacuum vessel.

3:9:7 The Vacuum Metal Evaporator

The samples to be evaporated were contained in a small tantalum tube which was hung from a molybdenum rod electrically isolated from a conflat flange on which it was mounted. The tantalum tube was held at an adjustable high voltage and a straight tungsten wire filament held 2 mm from the tantalum tube was used for electron bombardment heating. The deposition rate was monitored by an AT cut quartz crystal microbalance which oscillated at 6 MHz when clean. The crystal was mounted

close to the sample target and enclosed in a metal case with a small aperture in the front surface. The difference between the frequency of oscillation for the clean crystal and the coated crystal was proportional to the evaporated layer mass. Assuming that the density of the bulk metal is the same as an evaporated thin film then the mean thickness of the film can be calculated. Accumulated layers of evaporants on the target surface could be cleaned off by running the electron gun with the water cooling to the anode turned off, allowing the target to be flashed to white heat.

3:9:8 The Spectrometer Vacuum System

A schematic of the vacuum system is given in Fig. 13:11. The main spectrometer tank was pumped using a 150 l/min. single stage rotary pump which was connected to the tank by a copper vacuum line which included a magnetic shut off valve and a bakeable foreline trap. The pressure at the pump and at the tank could be measured using pirani gauges and the foreline trap could be isolated during bakeout by low vacuum diaphragm valves. The foreline trap prevented most of the oil from the rotary pump diffusing into the spectrometer vacuum tank. The spectrometer tank had a removeable lid which had an O-ring seal machined in its surface to provide a vacuum seal. The walls and lid of the tank were made of 20mm thick aluminium alloy and was of all welded construction. Rotary vacuum connections were made with rotary wilson seals and electrical connections were made by setting wires into an epoxy resin mould in an O-ring sealed flange. The proportional counter high tension connection was made through the tank by fitting an O-ring over the outer sleeve of the cable and making a fixed wilson seal. The crystal chamber was directly pumped from the main vacuum tank and used O-ring seals in all of its sealing joints. The crystal chamber could be valved off

from the thin polypropylene window by a manually operated VAT valve, the interspace formed being pumped from the diffusion pump backing line. As previously described, the UHV system was of all stainless steel construction and pumped by a liquid nitrogen trapped diffusion pump. The diffusion pump was backed by an all stainless steel bakeable backing line pumped by a 50 l/min. double stage rotary pump. Typical base pressures for the two vacuum systems were 0.05 Torr for the main spectrometer tank and 2×10^{-10} Torr for the UHV system.

3:9:9 Adjustment and Calibration of the Spectrometer

Many gypsum crystals were examined for obvious flaws and a good well cleaved piece was selected and clamped between the concave and convex surfaces of the crystal block. The four screws holding the two halves of the block together were also used to make small adjustments in the bending of the crystal. The crystal was first adjusted optically by observing reflections from its surface from a parallel source of light at an angle of incidence θ to the crystal normal. A line image was produced at an angle of reflection θ at a distance given by

$$\frac{1}{V} + \frac{1}{U} = \frac{2}{R \cos \theta}$$

U = Object distance
 V = Image distance
 θ = Angle of incidence
 R = Radius in meridian plane

for $U = \infty$

$$V = \frac{R}{2} \cos \theta$$

A point source of light was arranged at the focus of a convex lens and the resulting parallel beam of light was allowed to strike the curved crystal at an angle θ . The image was viewed with an eyepiece and the clamping screws were adjusted until a good line image was observed. Often the main line image was accompanied by several faint lines at small angles to the principal line and these could be removed by placing metal shim pieces over the vertical edges of the crystal to restrict the horizontal aperture.

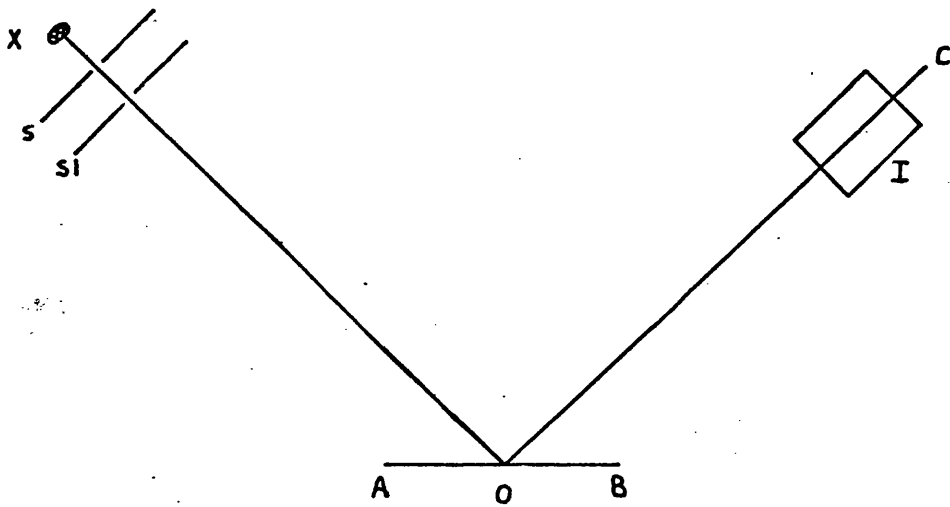
These stray lines were caused by imperfect bending at the edges of the crystal aperture. When the best image had been obtained the image distance was measured from which the radius of curvature could be calculated. The crystal block was then mounted in the spectrometer and using the calibration x-ray source, the copper $K_{\alpha,2}$ lines were recorded photographically by placing a small section of x-ray film on the appropriate part of the Rowland circle. Several different crystals were tried before a good sharp doublet was obtained.

The crystal was now optically aligned in the spectrometer. All the rotation and translation mechanisms were adjusted mechanically into their correct positions and then a prism was attached to the counter table to allow laser light, from a small laser mounted on the rotateable spectrometer table, to pass through one of the two alignment holes equidistant from the slit centre (Plate 3(2)). Light was reflected from the crystal towards the second hole and the crystal mount was adjusted until the light fell exactly on this second hole. The spectrometer mechanism was now moved towards the crystal and the process repeated. This was done many times until traversing the spectrometer did not cause the reflected light beam to move up or down on the second hole. A more precise adjustment was made by opening one side of the counter slits up fully and observing a strong emission line photographically so that the line appeared in the position of the slit centre. The crystal tilt was adjusted slightly until the shadow cast by the half slit jaw and the x-ray line were parallel by successive adjustments and exposures. Once aligned the dispersion of the instrument was measured by measuring the chord length which corresponded to the best image quality of an emission line.

$$x = R \sin \theta \quad \text{where} \quad \begin{array}{l} x \text{ is the chord length} \\ R \text{ is the crystal radius} \\ \theta \text{ is the Bragg angle} \end{array}$$

The crystal was rotated so that the chosen emission line would be on the optical axis of the spectrometer, and by a succession of photographs, the chord length corresponding to the best image was obtained. From the above equation the crystal radius could be calculated. Further checks were made using doublet line separations.

A calibration line should be well defined with a sharp peak, well resolved from neighbouring lines and chemically stable. Unfortunately in the long wavelength region few of these lines exist and it was necessary to record short wavelength lines in higher orders, correcting for refraction. The $K_{\alpha_{1,2}}$ doublets of Ni, Zn, Fe, Mn, Ti, Cu and Co were measured together with many K_{β} lines of these elements. From $7.5\overset{\circ}{\text{A}}$ to $9.0\overset{\circ}{\text{A}}$ thirty five lines were recorded in higher order to check the linearity and calibration of the spectrometer, and Aluminium $K_{\alpha_{1,2}}$ was recorded in the first order as a test of resolving power. As no crystal window function data was available the resolution could only be estimated against the same spectrum recorded on a double crystal instrument (Hall, 1979). As no difference could be detected between the two spectra and the double crystal resolution was less than 0.5 eV, the resolution of this spectrometer must have been similar. The degree of accuracy with which the wavelength scale could be established in the region of the profiles to be mapped was only limited by the resolving power of the spectrometer and the accuracy with which the calibration line wavelengths had previously been measured. In the regions of the $M_{\alpha,\beta}$ lines of thulium, ytterbium and lutetium, the energy scale was established to an accuracy of ± 0.1 eV.



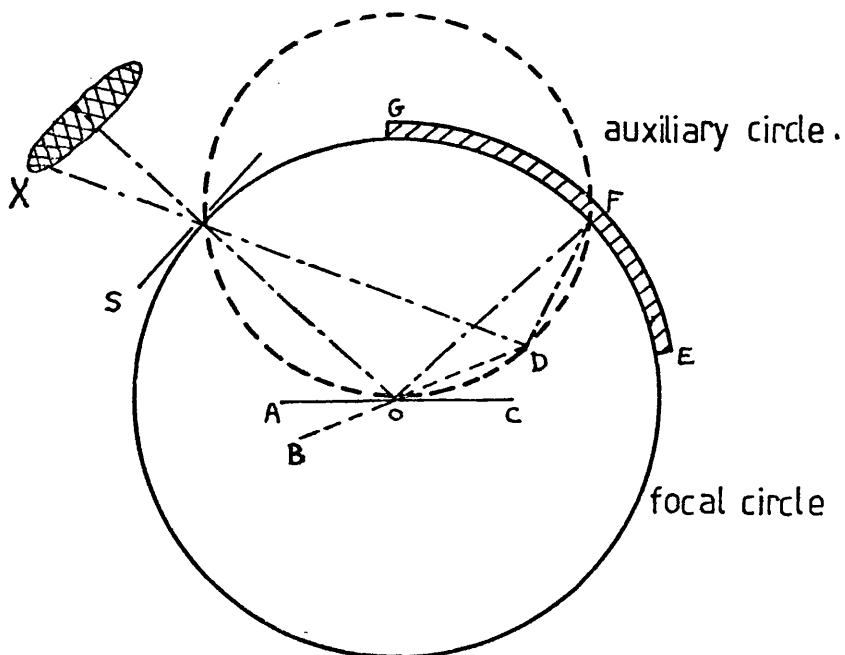
X, point or small source.

S, entrance slits

AB, crystal

I, detector

FIG 3:1 SIMPLE BRAGG GEOMETRY.



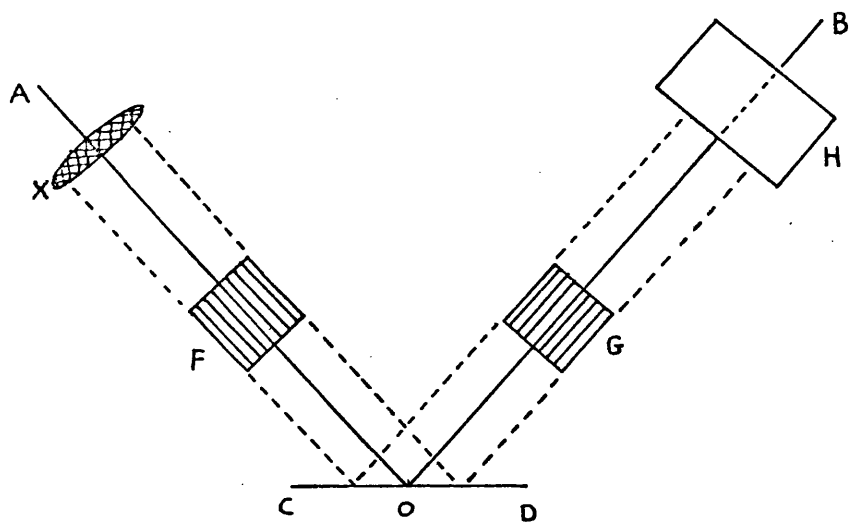
X, extended source

S, entrance slit

AC, crystal

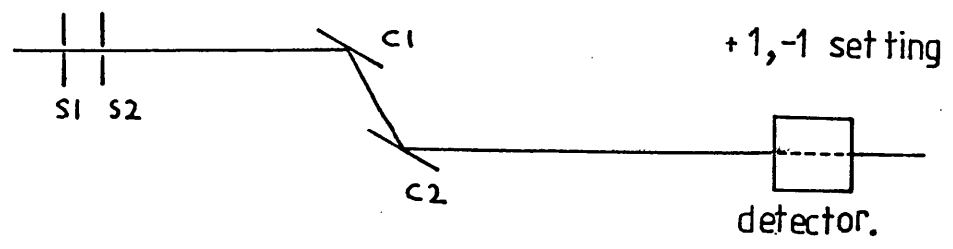
GF, film

FIG 3:2 OSCILLATION SPECTROGRAPH.

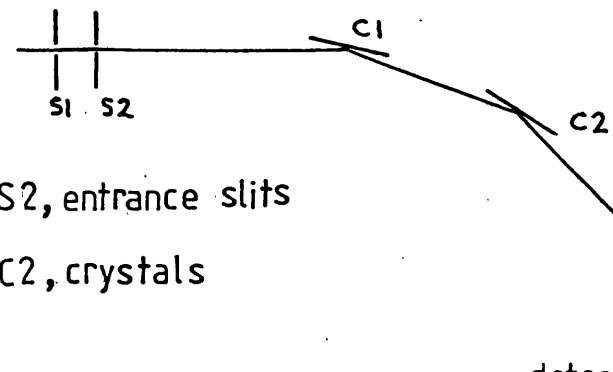


X, extended source F, entrance collimator G, exit collimator
 CD, crystal H, counter $\angle AOC = \angle BOD$

FIG 3:3 SOLLER SPECTROMETER



+1, -1 setting

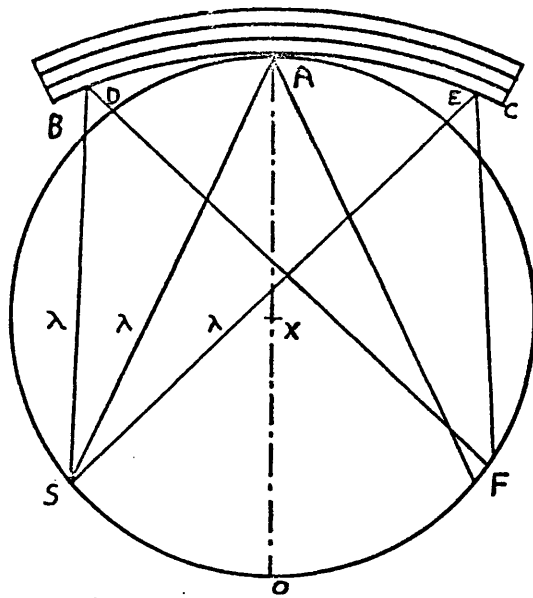


+1, +1 setting

S1 S2, entrance slits
 C1 C2, crystals

detector

FIG 3:4
 DOUBLE CRYSTAL SPECTROMETER POSITIONS.



crystal radius = $AO = 2.XA$ XA : rowland circle radius
 S: point source F: approximate focus BC: curved crystal

FIG 3:5 JOHANN GEOMETRY FOR CURVED CRYSTAL FOCUSING.

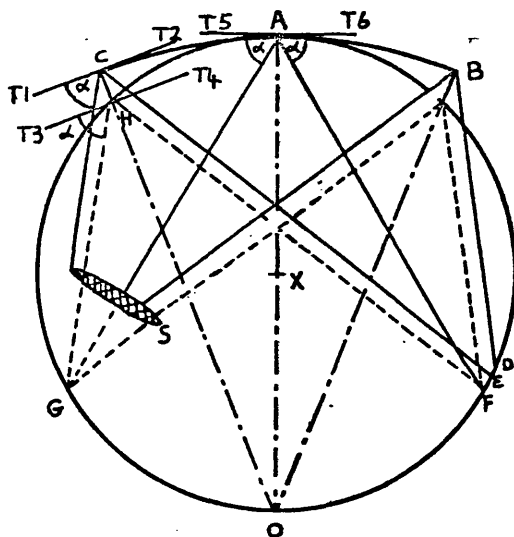
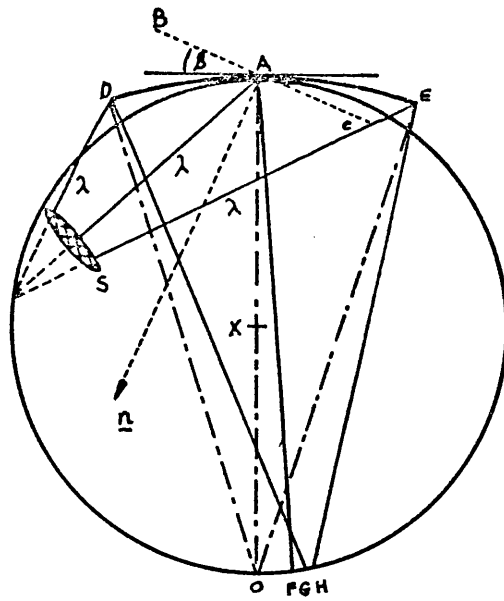


FIG3:6 ABERRATIONS PRODUCED BY A FINITE HORIZONTAL CRYSTAL APERTURE (JOHANN).



S: extended source FGH: approximate focus DAE: crystal
 AO: crystal XA: rowland circle radius $AO = 2 \cdot XA$
 BC: crystal planes at angle β to surface. n : normal to BC

FIG 3:7 REDUCTION OF APERTURE BROADENING BY THE USE OF INCLINED CRYSTAL PLANES.

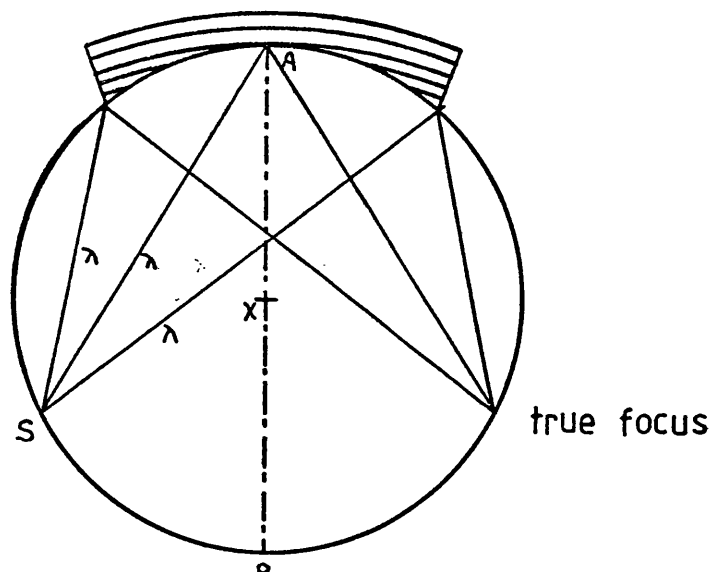


FIG 3:8

crystal bent to radius OA and optical surface ground to radius XA.
 $OA = 2 \cdot XA$

METHOD FOR PRODUCING A TRUE FOCUS.

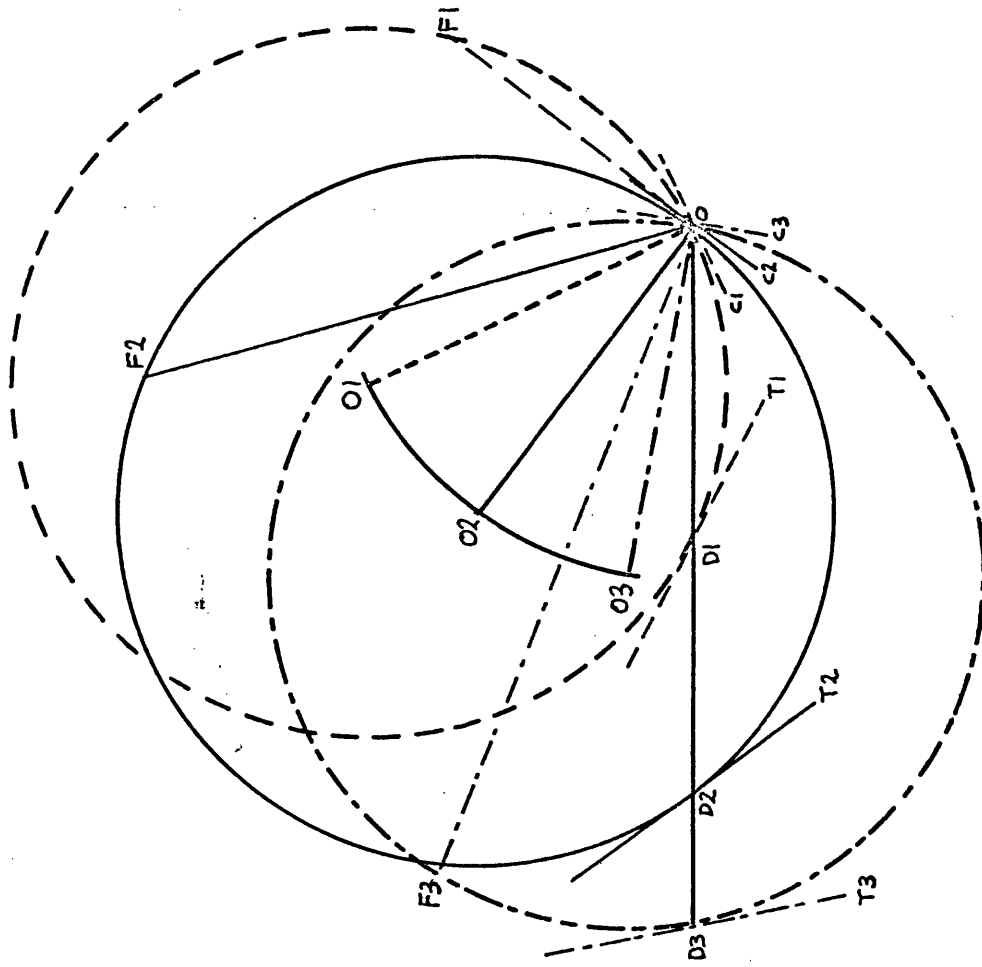


FIG 3:9 GEOMETRICAL ARRANGEMENT OF THE SPECTROMETER .

c1-4 : proportional counter in positions along the Rowland circle.
 arrows show slit direction.

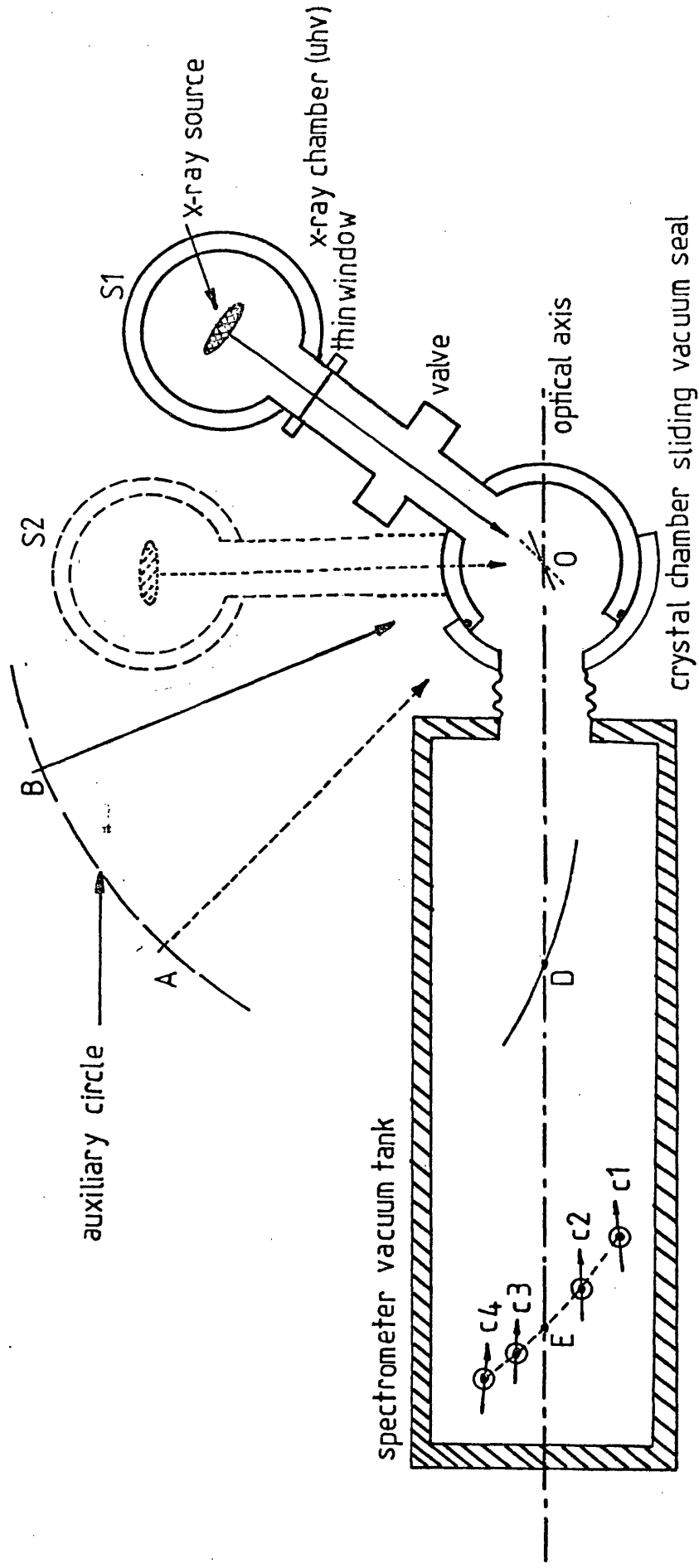
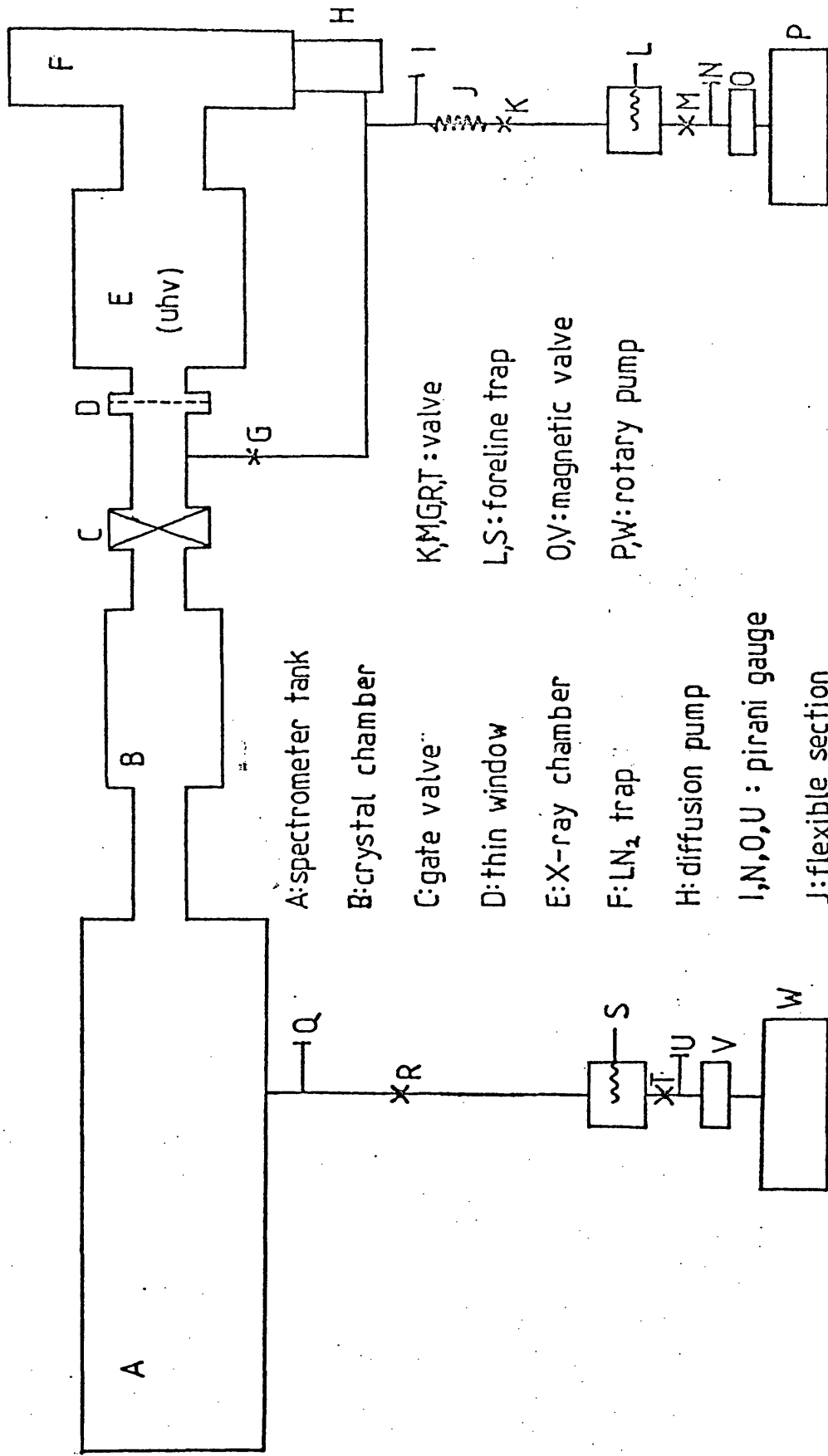


FIG 3:10 LAYOUT OF SPECTROMETER WITH COMPONENTS IN TWO MAJOR POSITIONS.



A: spectrometer tank

B: crystal chamber

C: gate valve

D: thin window

E: X-ray chamber

F: LN₂ trap

H: diffusion pump

I, N, O, U : pirani gauge

J: flexible section

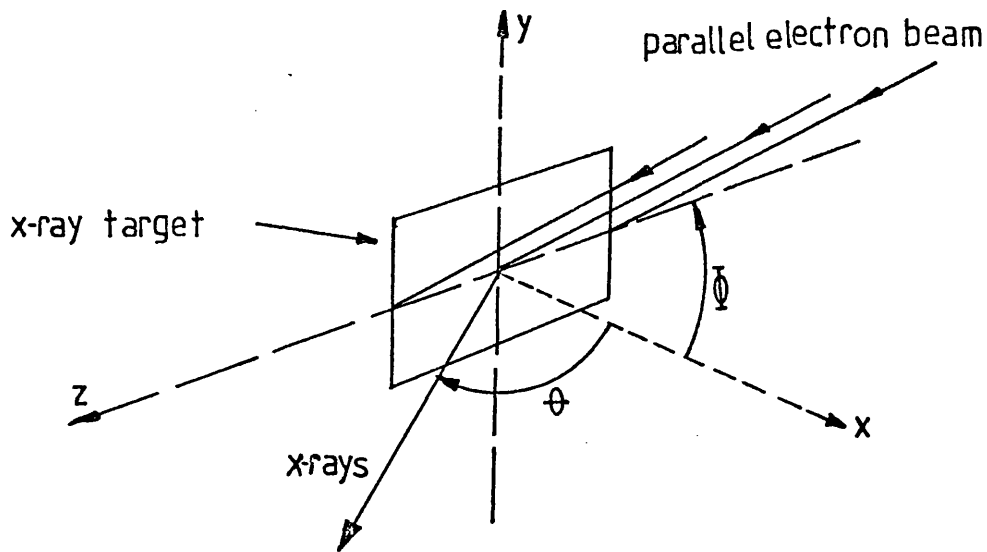
K, M, G, R, T: valve

L, S: foreline trap

O, V: magnetic valve

P, W: rotary pump

FIG 3:11 SPECTROMETER VACUUM SYSTEM.



fixed exit direction (crystal fixed in xz plane).
 electron incidence angle ϕ and x-ray take off angle θ
 variable between 0° and 90° .

FIG 3:12 GEOMETRY OF SAMPLE TARGET

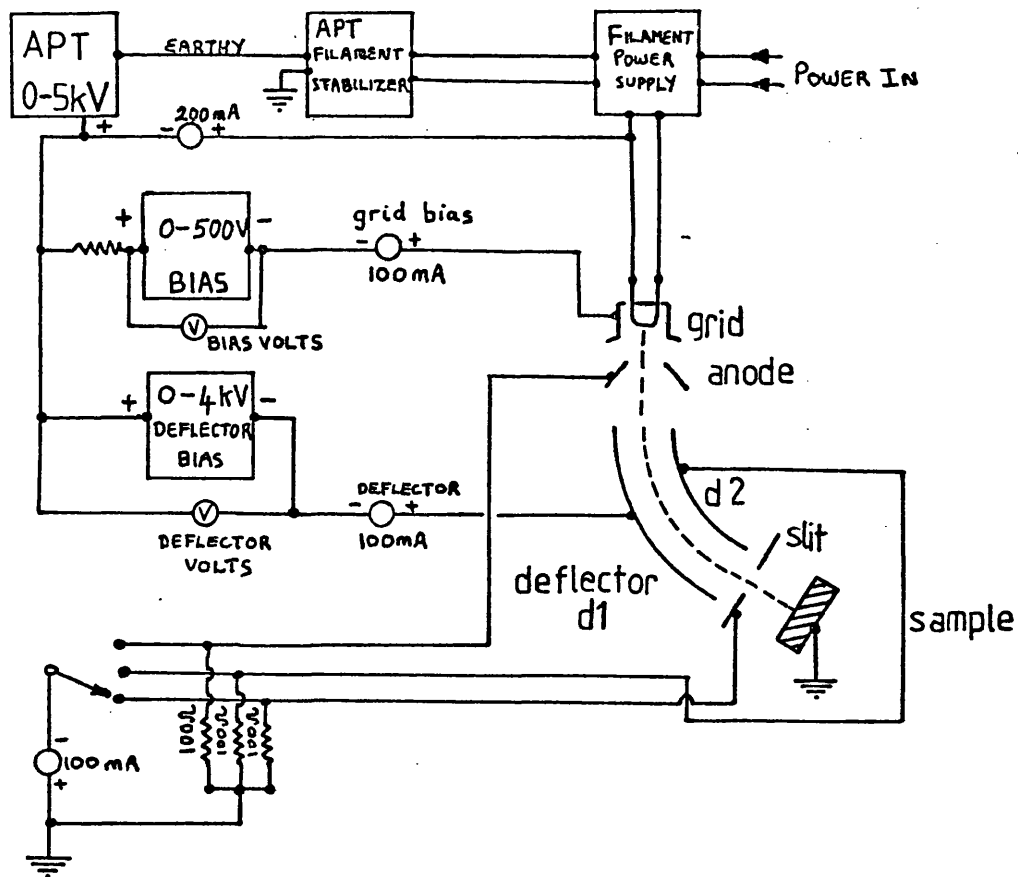


FIG 3:13 ELECTRON GUN POWER SUPPLY

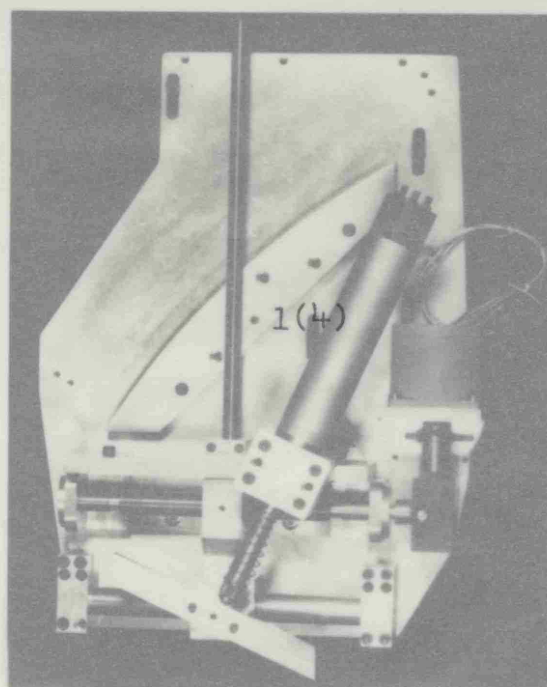
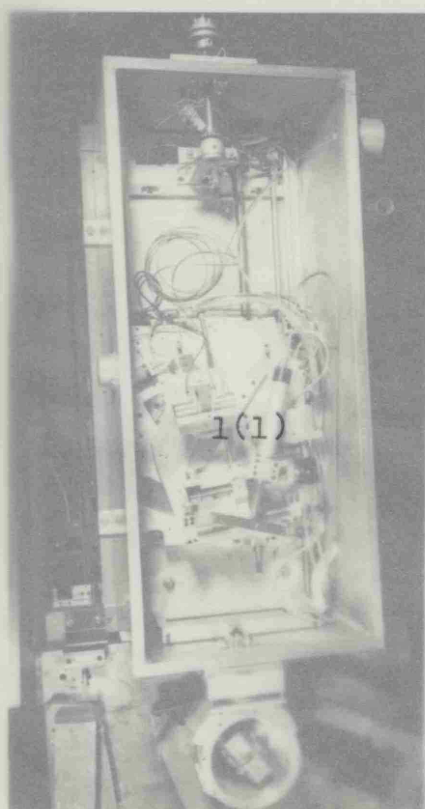
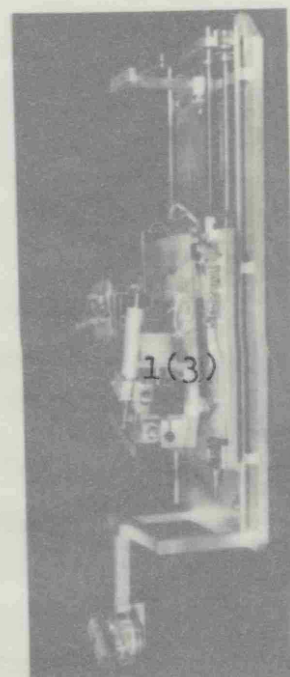
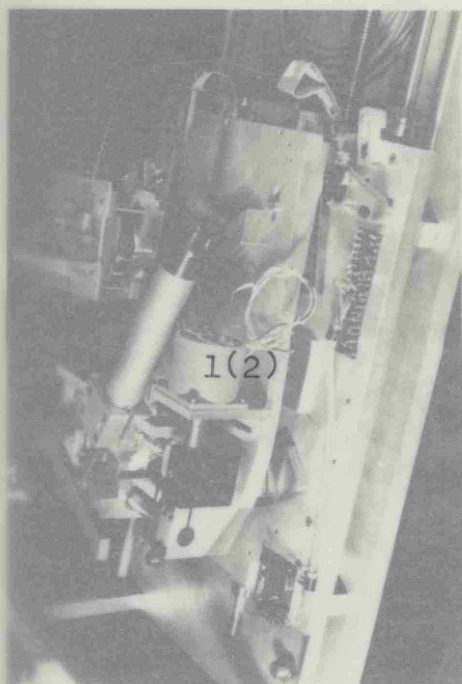
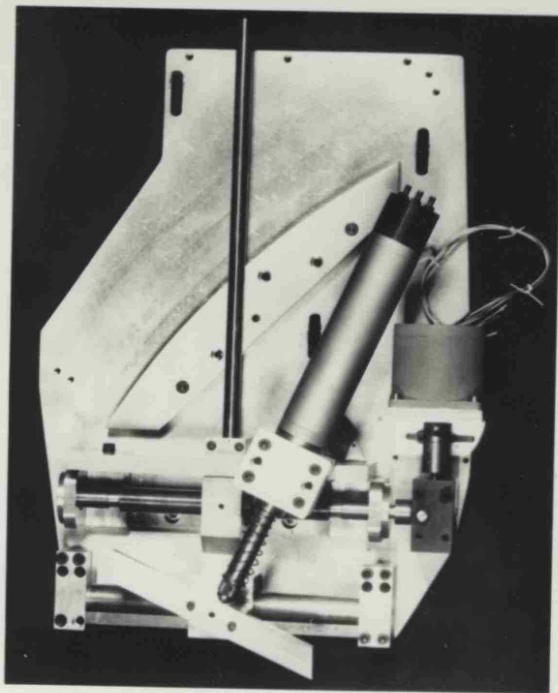
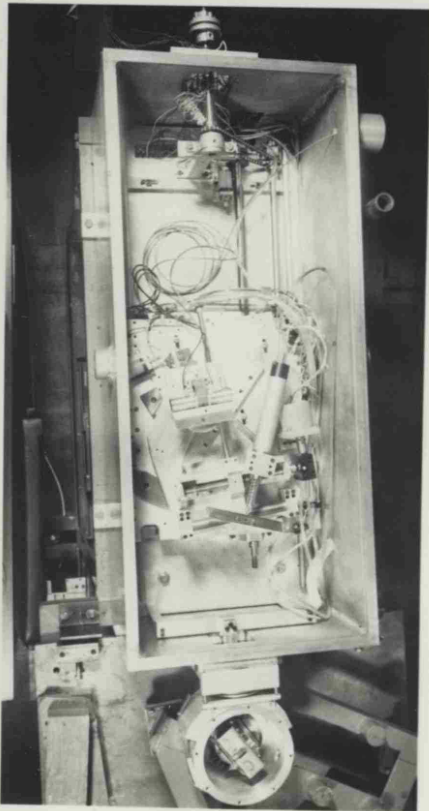
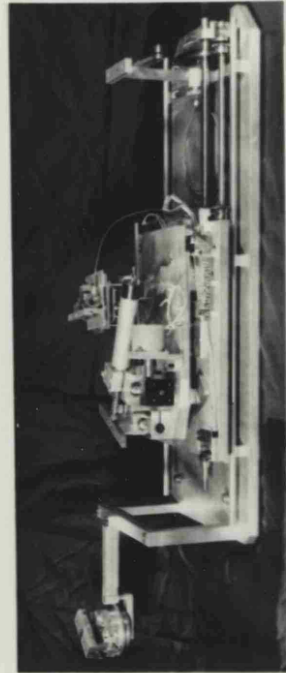
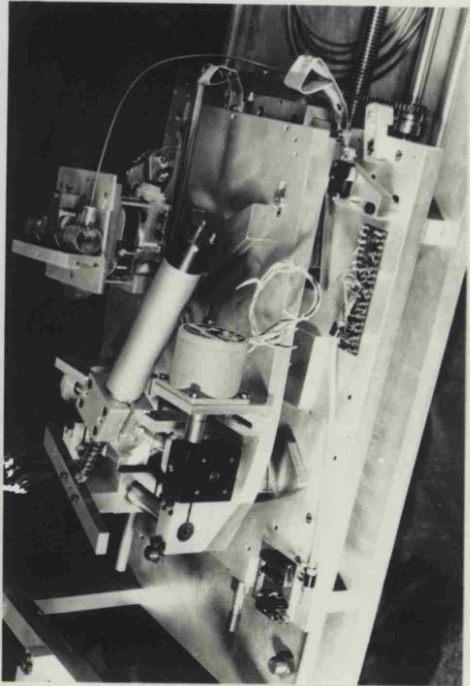


PLATE 1: MECHANICAL ARRANGEMENT OF THE SPECTROMETER TABLE.



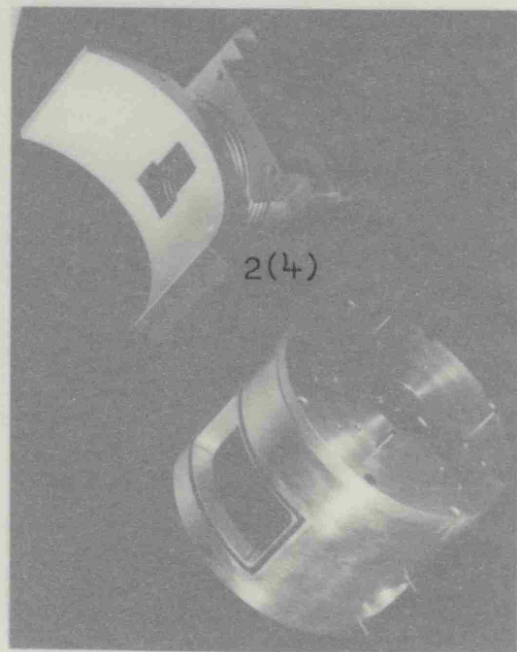
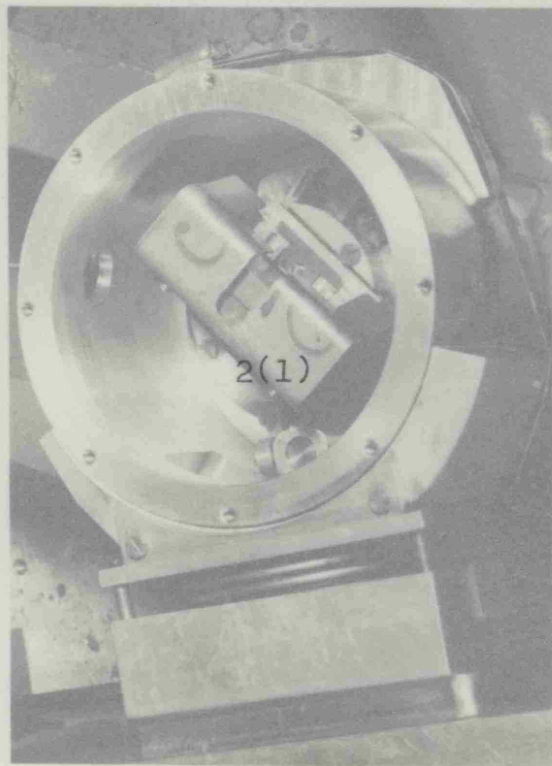
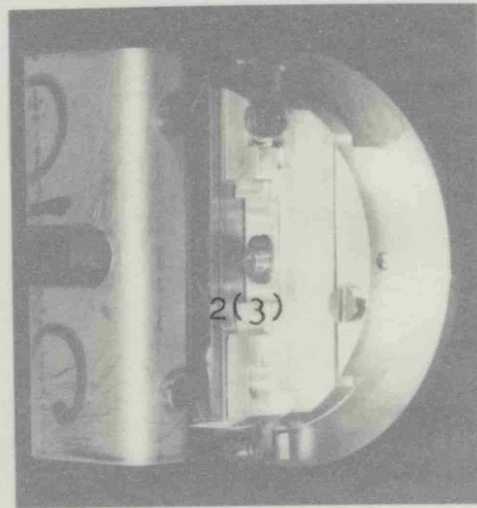
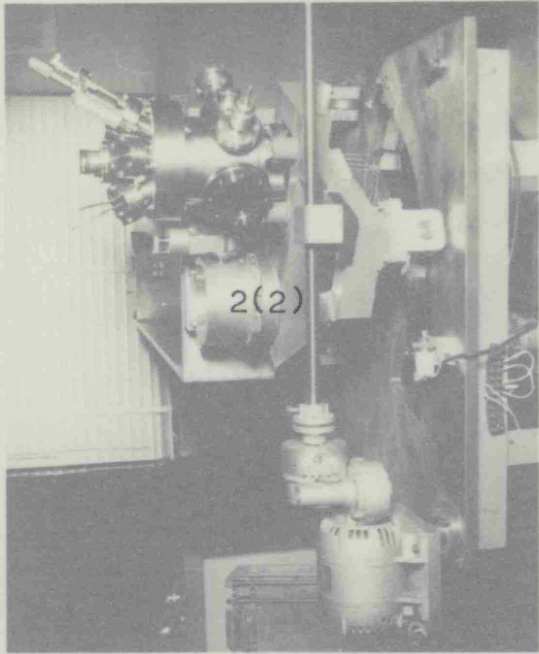
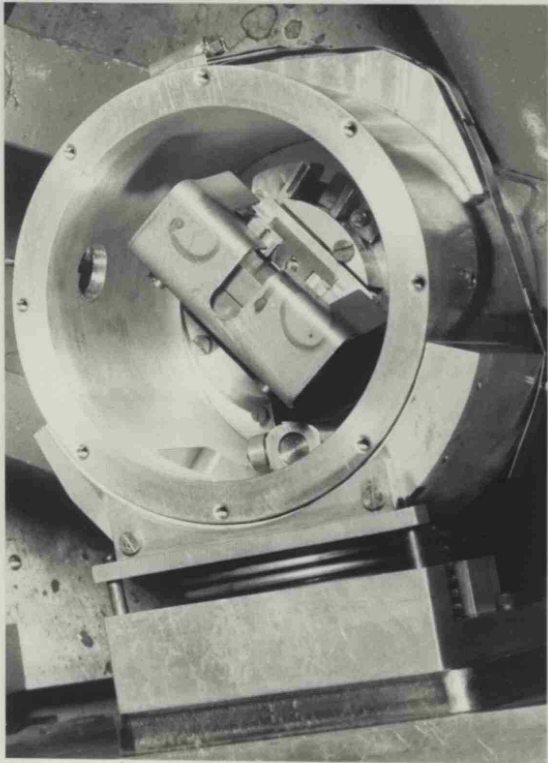
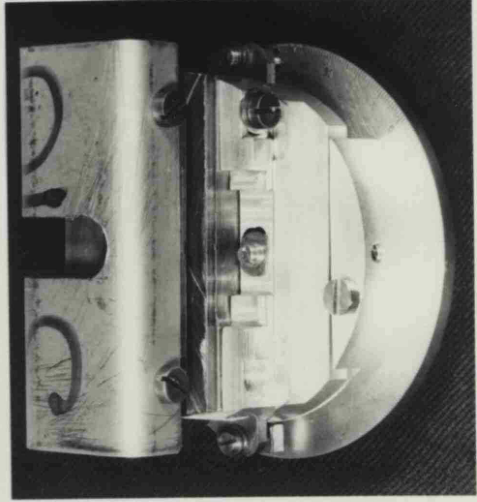
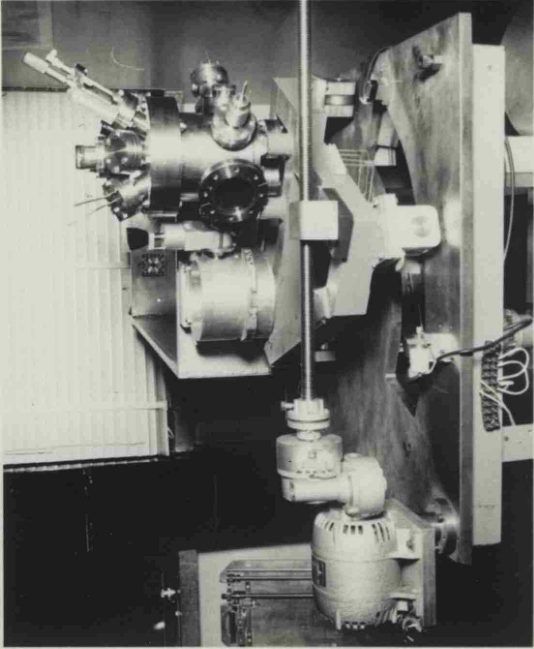


PLATE 2: THE CRYSTAL CHAMBER AND CRYSTAL BLOCK



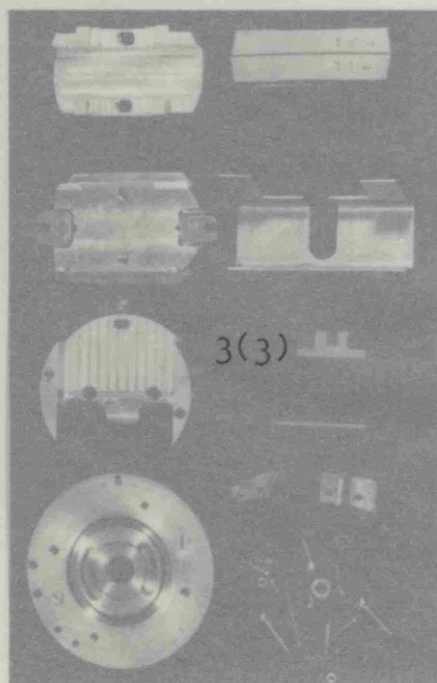
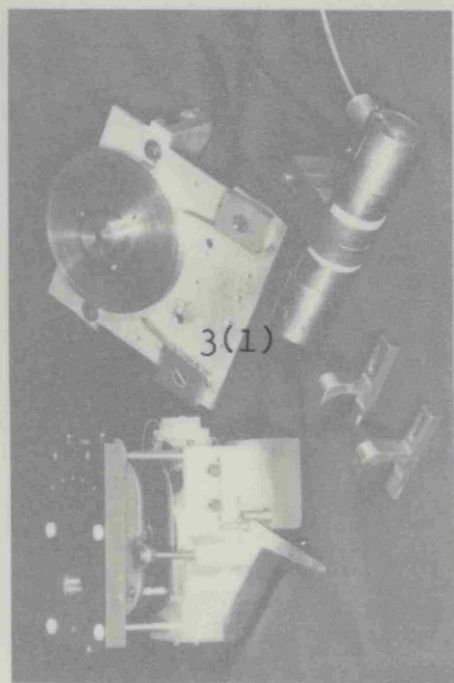
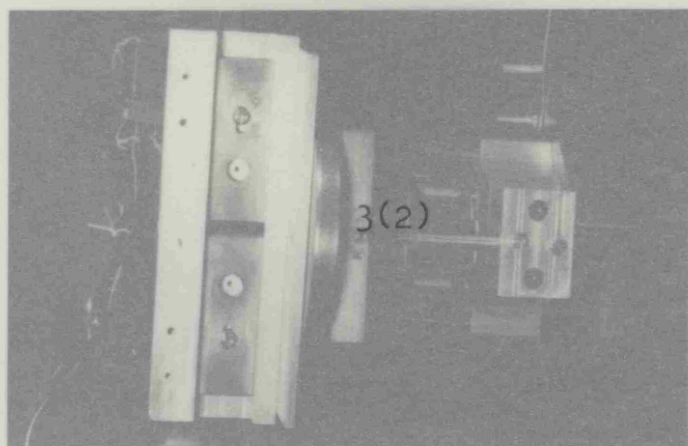
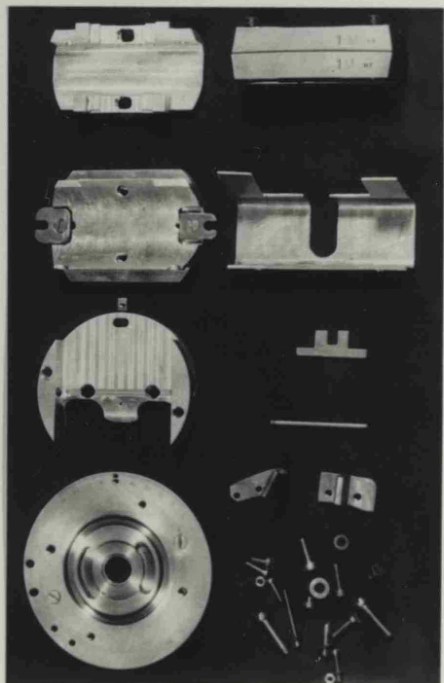
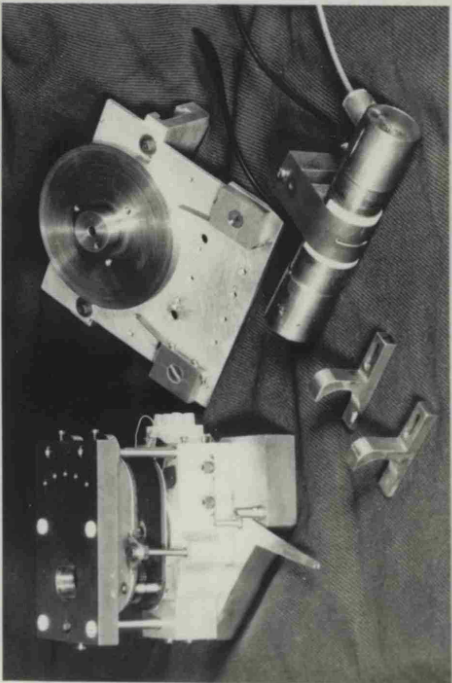
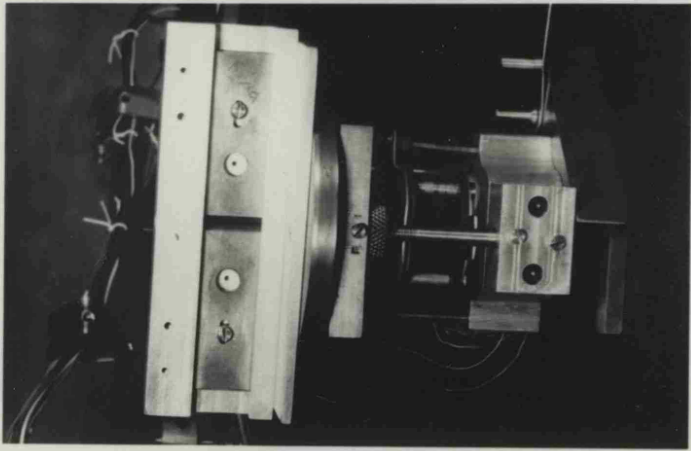


PLATE 3: ARRANGEMENT OF THE COUNTER
SLIT AND CRYSTAL BLOCK.



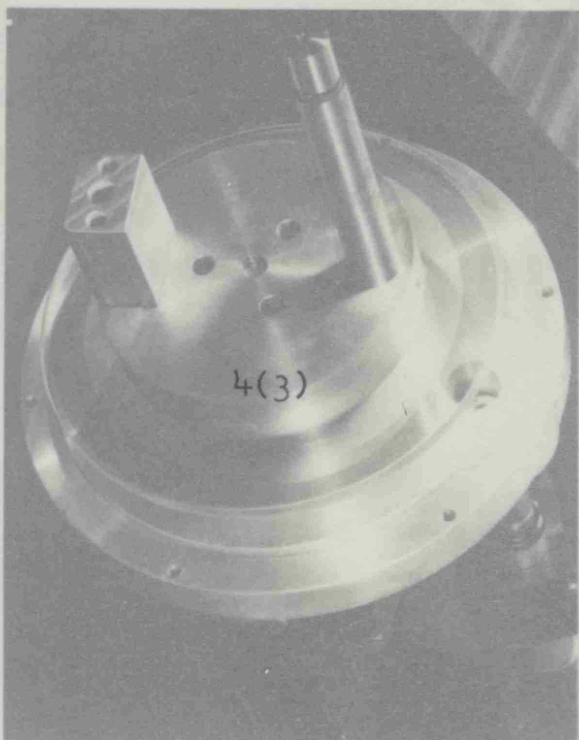
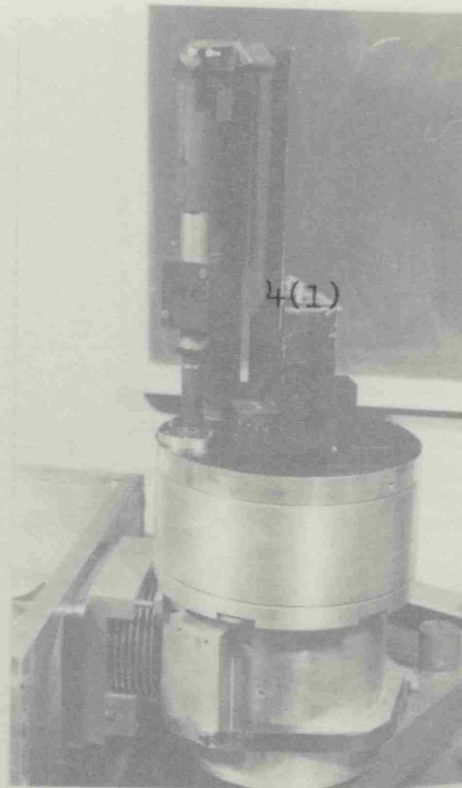
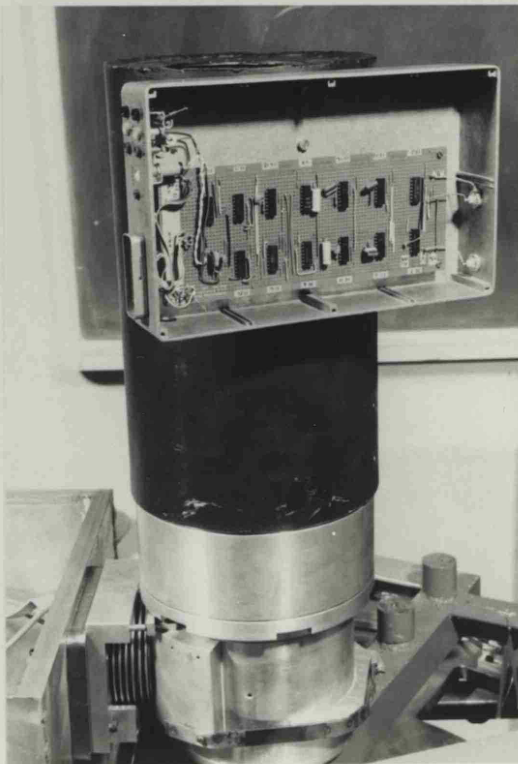
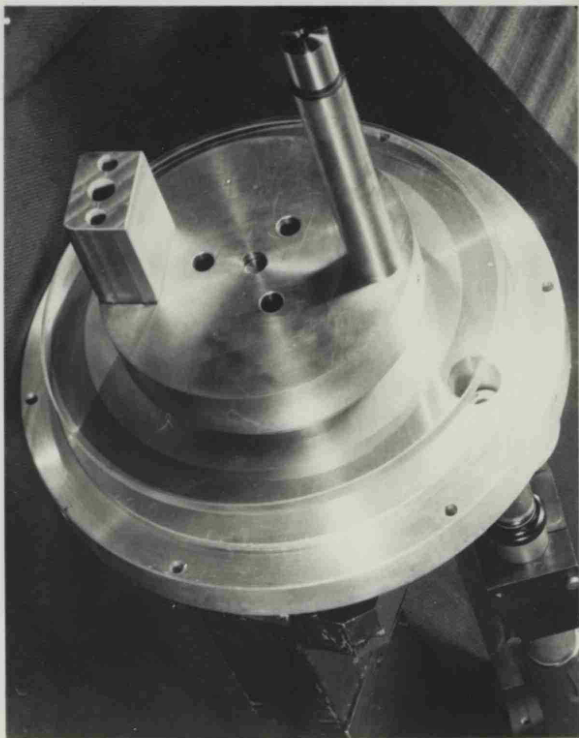
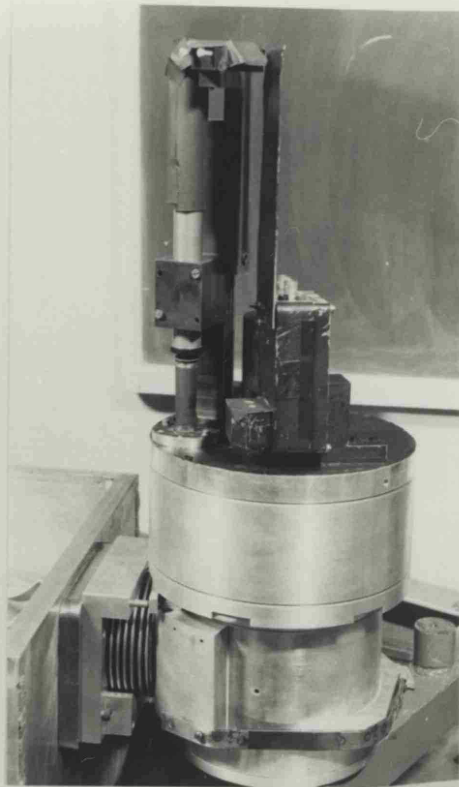
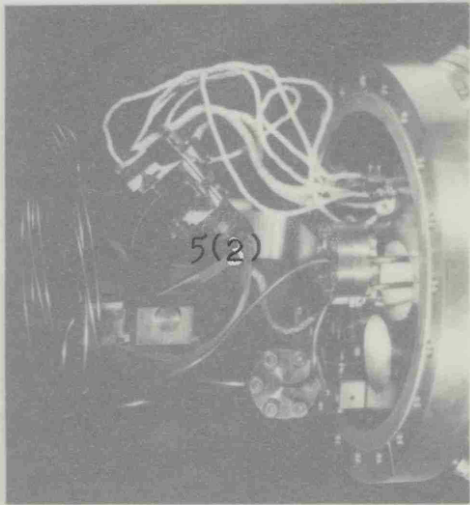
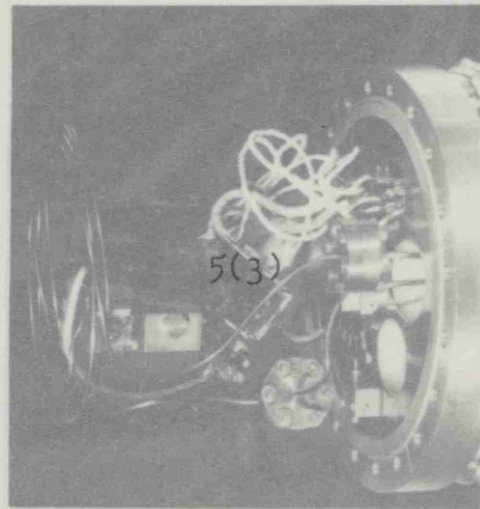


PLATE 4: THE RADIAL GRATING ENCODER

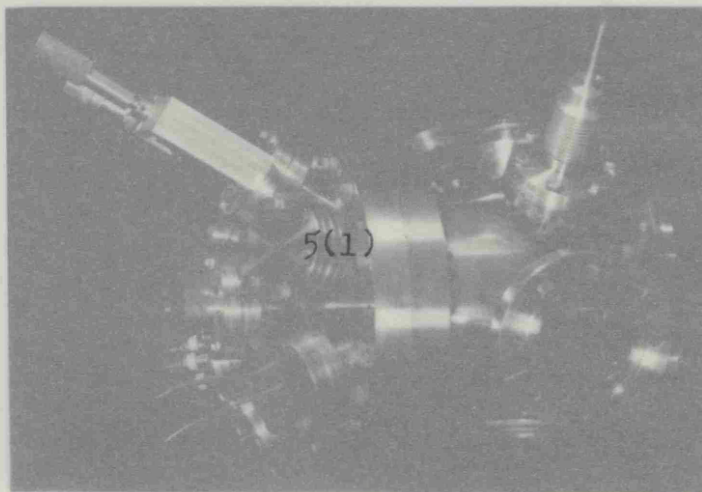




5(2)

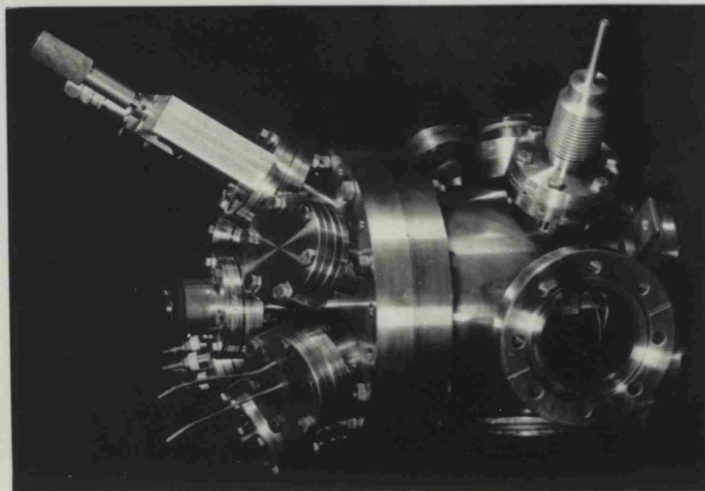
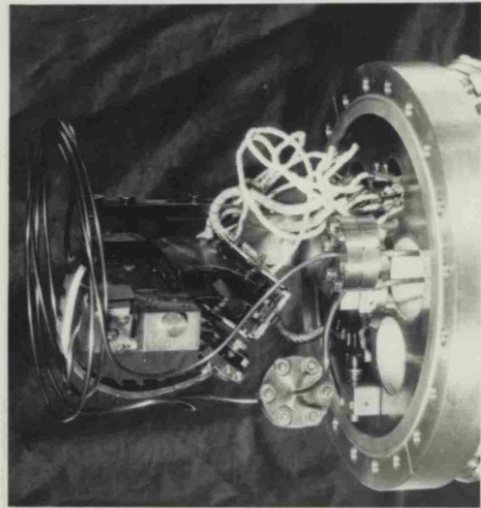
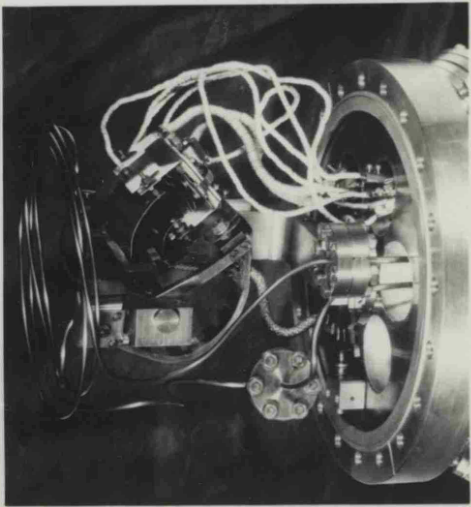


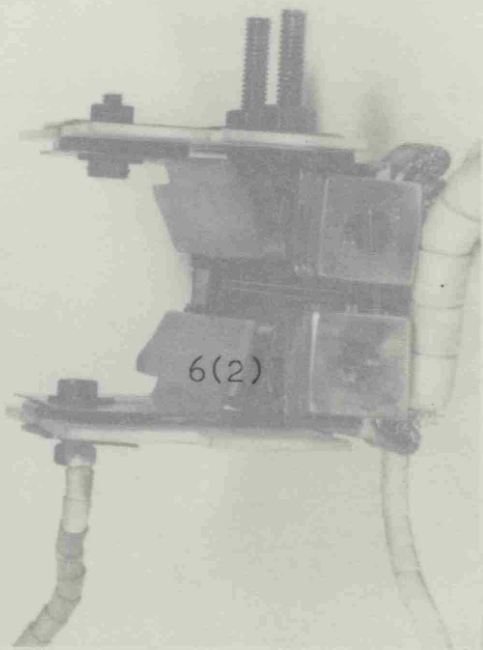
5(3)



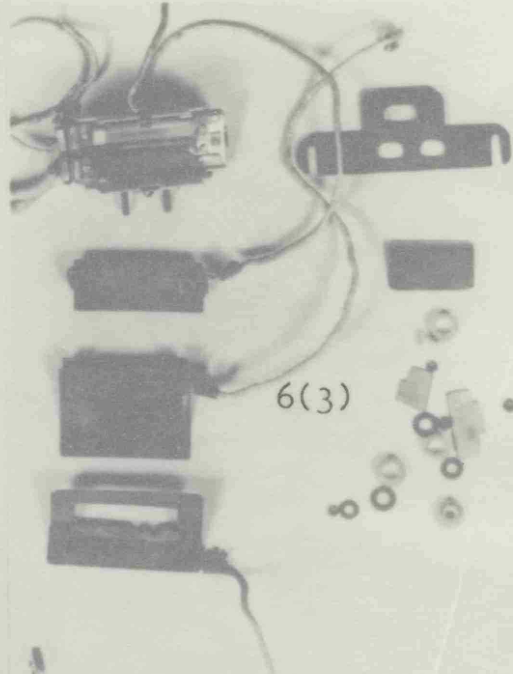
5(1)

PLATE 5: THE X-RAY SOURCE CHAMBER AND TARGET ARRANGEMENT

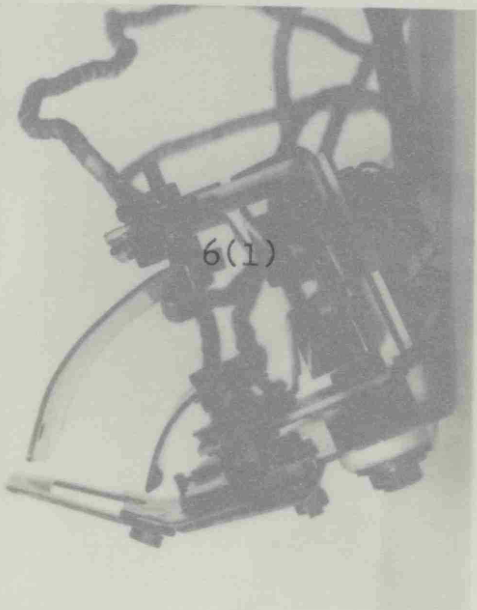




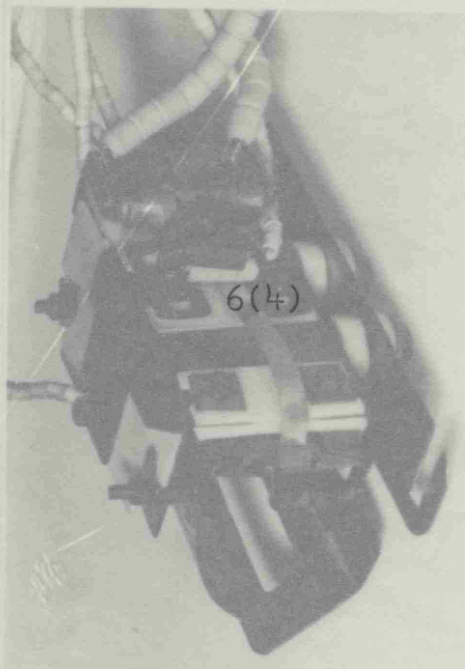
6(2)



6(3)

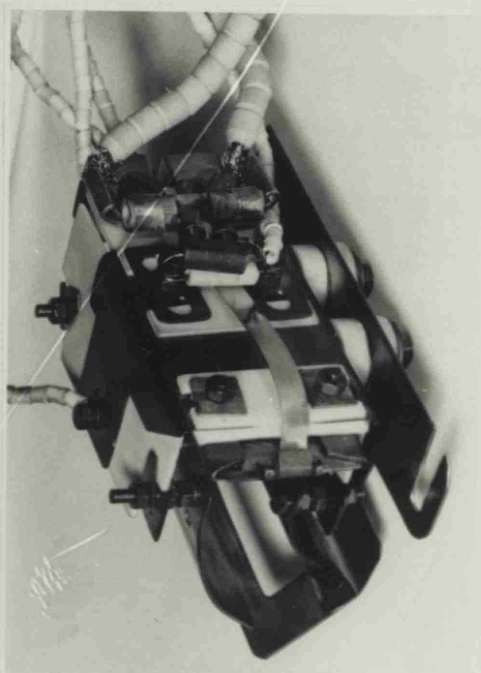
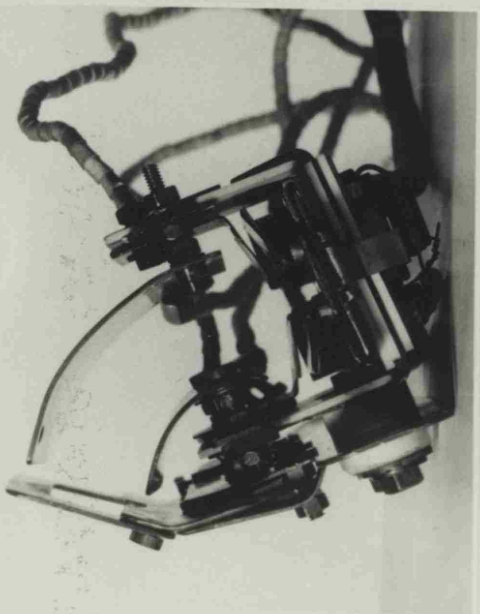
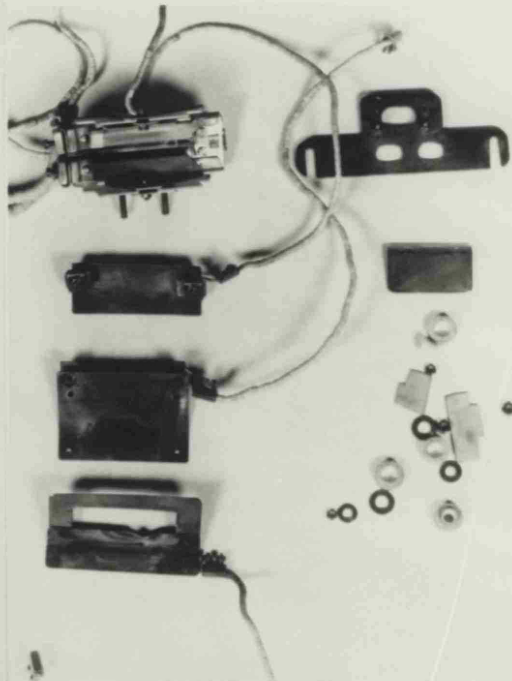
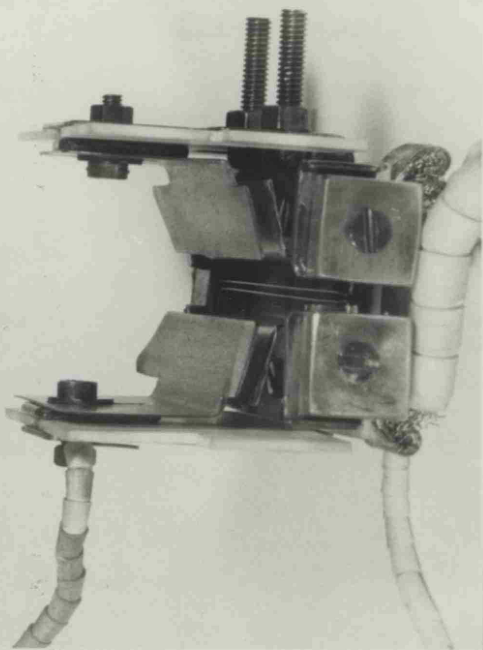


6(1)



6(4)

PLATE 6: THE ELECTRON GUN



CHAPTER 4

THE SPECTROMETER DETECTION AND CONTROL SYSTEMS

	<u>Page No.</u>
<u>Introduction</u>	67.
4: <u>Part a</u> The Microprocessor Controlled Data Acquisition System.	67.
4:a(1) Stepping Motor Oscillators and Interfaces.	73.
4:a(2) Crystal Angle Measurement	74.
4:a(3) Unit 1: The Data Sampler, Display and Formatter	76.
4:a(4) Unit 2: The Digital Tape Recorder	77.
4:a(5) The a.c. Motor Control System	78.
4:a(6) The Microprocessor Hardware	81.
4:a(7) The Microprocessor Software	82.
4: <u>Part b</u> The X-ray Photon Detection System	83.
4:b(1) The Gas Flow Proportional Counter	84.
4:b(2) The Detection Electronics and Gas Supply System	86.
4: <u>Part c</u> Operation of the Spectrometer Detection and Control Systems	87.

THE SPECTROMETER DETECTION AND CONTROL SYSTEMSIntroduction

The detection and control system requirements for an x-ray spectrometer vary according to the conditions under which an experiment is conducted. If the experimental conditions are stable and there is a low noise high count rate signal, simple plotting of the data using suitable integrators may be adequate. If however the experimental conditions are unstable or a low count rate signal with a high background noise level is to be expected, then a more precise data acquisition procedure must be used.

In general, the $M_{\alpha,\beta}$ structures of the rare earths are weak and contain complex overlapping features which are difficult to resolve. The spectra of some of the rare earth metals have been shown to be sensitive to small amounts of contamination (Parrott 1965) and it was expected that ageing effects would be seen due to oxidation even in an ultra high vacuum environment. It was decided therefore that while the control system should have certain data acquisition routines built in, it should be easily reconfigured to suit different experimental conditions. This flexibility meant that a microprocessor had to be used to execute the data acquisition algorithms and control the logging of data. Particular care was taken in the design of the photon detection and counting system to reduce the background noise level to a minimum

Part (a) The Microprocessor Controlled Data Acquisition System

The arrangement of components within the data acquisition system is shown in Figure 4(1). In this system the task of the microprocessor is to control the movement of the counter stepping motors in accordance with a specific algorithm, control the

logging of raw data onto tape, provide information on the progress of the algorithm on the visual display unit and to dump data produced by the algorithm into the university computer file store. The data stored on magnetic tape or in the university computer file store was analysed in detail after each experiment on the university CDC Cyber 73 main frame computer. The data acquisition routines were contained in machine code microprocessor software and could be executed by typing simple control commands on the visual display unit. The microprocessor would then execute the particular algorithm selected and provide information on the visual display unit of the state of execution within the algorithm. The main control program contained four basic algorithms and is listed in Appendix A. Many other data acquisition and test programs were written but these could not be contained in the main program because of shortage of microprocessor memory.

To demonstrate the operation of the system we must use a particular data acquisition algorithm and follow through the actions of each component. We will use the SCAN3, POINT BY POINT (COUNTS) routine as listed in Appendix A. Pulses corresponding to detected x-ray photons were accumulated for ten seconds in a pulse counter (R.C.S. Electronics). The accumulated count was then displayed for one second before resetting and repeating the process. The pulse counter was modified by fitting buffer electronics into the six digit display so that a six digit binary coded decimal (B.C.D.) output was provided. Also a 'data ready' line was provided which went to logic 1 when the counter was displaying the accumulated counts. The timing for the ten second accumulation period was divided down from a crystal oscillator and was used as a timing signal throughout the whole system. The position of the counter along the Rowland circle was measured by an electrical micrometer as described in

Chapter 3, the output from which being fed into a signal conditioning unit which gave a linear zero to ten volt output as a function of displacement. The six digit B.C.D. encoded count rate with a display command line and the electrical micrometer analogue signal were fed into unit 1 of figure 4(1). The function of unit 1 was to convert the micrometer signal to a twelve bit binary signal, decode to fifteen bit B.C.D., and every ten seconds to convert this and the six digit B.C.D. count rate into a 110 baud ASCII format serial signal. The unit also introduced space characters after each group of characters and a line feed and carriage return characters after twelve groups. Twelve groups represented six data points. The unit had a four digit decimal display to show the output from the electrical micrometer analogue to digital converter. A twelve bit binary analogue to digital converter was used giving a resolution of 1 part in 4096 which is in accordance with the resolution requirements stated in Chapter 3. The 110 baud serial signal was fed into unit 2 of Figure 4(1) which consisted of a data buffer, timing circuitry and a tape cassette (Memodyne Corporation type 440) which used digital encoding based on the ECMA 34 and Texas Instruments format. The choice of digital encoding over audio encoding was dictated by the need for compatibility with the university computer centre's tape cassette reader and the low error rate which was required. Extensive buffer memory and timing electronics had to be used with the tape cassette unit to modify its action so it could be used as a constant data logger. The operation of units 1 and 2 are described in detail later in this chapter.

The system described so far continuously logs positional and intensity data at fixed intervals. This operation could be stopped by depressing a switch on unit 1, or by the microprocessor

sending a logic 1 signal to unit 1. The four digit B.C.D. encoded electrical micrometer signal, the six digit B.C.D. encoded accumulated counts signal and the data display signal from the counter were relayed from unit 1 to the microprocessor peripheral interface adaptors, P.I.A.'s as shown schematically in figure 4(2). These P.I.A.'s were wired and programmed to act as inputs, so that if polled, the information on the inputs at that time would be latched so that the microprocessor central processing unit (C.P.U.) could read the data. The P.I.A. input ports can be thought of as memory locations controlled by the input of four digit B.C.D. encoded crystal angle information and for data ready or calibration signals. All the other P.I.A. ports were outputs. The data enable signal was sent from one bit of an output port and two halves of one P.I.A. part were used to select control signals to the two stepping motor driver decoders. The options were stop/start, forward/reverse, very fast/fast and slow/very slow oscillator speeds. Communication to and from the microprocessor was handled by a 4800 baud serial interface at Port 0, and communication to and from the university central computer was handled by a 1200 baud serial interface at Port 1. The detailed operation of the microprocessor is described in Part a(6) of this chapter.

In the algorithm chosen to demonstrate the sequence of operations of the microprocessor controlled system the execution is as follows:-

Step (1) Ask the operator via the serial interface at Port 0 the micrometer readings on unit 1 which correspond to the start and finish of a scan. Ask for the increment distance on a scale between the start and finish micrometer readings and the number of counts to be accumulated before incrementing takes place.

Step (2) Remove the backlash in the counter drive by advancing

the counter to a preset distance past the requested start position and back again to the correct position, the overshoot distance being more than the mechanism backlash.

Step (3) Switch on the digital recorder by sending a signal from Port 6B

Step (4) Clear a section in memory for the count signal from unit 1.

Step (5) Wait for a display signal to appear at Port 3B

Step (6) Add the count signal to the count stored in memory.

Step (7) Check to see if the count stored in memory is greater than the requested minimum. If the count in memory is greater than that requested, print a message on the visual display unit (V.D.U.) using the Port 0 serial interface, to inform the operator that counting has stopped and that the counter is advancing to its next position.

Step (8) Switch off the recorder by sending a signal from Port 6B.

Step (9) Calculate the requested increment subtracted from the current micrometer position. If this is less than the requested finishing value, end the routine and print a message on the V.D.U. to tell the operator that the routine has terminated. Also print the data memory pointer position.

Step (10) Store the accumulated count and the current micrometer position in a data table in memory by storing the data at a position indicated by a memory pointer. Advance the data memory position.

Step (11) Advance the counter to the new position as calculated in Step (9).

Step (12) Go to (3)

At the end of the routine control is handed back to the monitor which is a program that controls the basic operations of the micro-processor such as the examination of a segment of the

memory, instructing the microprocessor to execute instructions starting at a particular address in memory or execution of the loader program. The loader program is responsible for dumping information from memory to the university central computer file store and the loading of program code from the file store into memory. Both the monitor and loader programs were written on erasable programmable read only memories (EPROM), which are memory chips that allow the program to be retained when the power to the device is off, and may only be erased by exposure to a high power ultra violet lamp. Programming of the EPROMs was done externally to the microprocessor system using a purpose built EPROM programmer. The microprocessor was wired so that when the power was turned on execution would start at the beginning of the monitor program which would then wait for instructions to be given through the v.d.u.

In the example given of the execution of a data acquisition algorithm, the data set stored in memory could be dumped into the university file store by execution of the loader program and then analysed and plotted immediately using the central computer. In the example algorithm the object was to equalize the number of counts associated with each data point, so that each point would have equal statistical significance. This was done approximately in the routine by altering the number of ten second blocks counted. Because of the large amount of memory required, the information stored in memory consisted of only the accumulated count, the micrometer reading and the number of ten second periods used. The tape contained information on every ten second period and so each micrometer data point made up of many ten second accumulations could be examined as a time series. It was therefore possible to remove to some extent short term and long term non statistical variations in the data. As an example, long term

variations could be caused by drift in the lower level setting of the pulse discriminator in the counting system and short term variations could be caused by a discharge in the x-ray gun. Although the memory dump integrated these effects, it was good enough to be used as a guide to the course of a set of experiments and in practice was found to be invaluable. Using Fourier filter and auto-correlation techniques (Chapter 5) the signal to noise ratio of tape data could be greatly increased.

As well as the routine described above several more routines were written, each specifically designed to suit particular experimental conditions and perform simple real time analysis tasks. The extent of real time analysis was limited by the small amount of microprocessor memory available.

4:a(1) Stepping Motor Oscillators and Interfaces

The microprocessor control system (Fig. 4(1)) used two oscillators and microprocessor interfaces to drive the motors associated with the counter rotation and counter traverse. The circuits were essentially the same for both motors except that the final drive transistors had a higher power rating for the counter traverse motor than for the counter rotation motor. The counter traverse motor was a Texas Instruments Slo-Syn motor type MO61-FD301, and the counter rotation motor was an Impex type 9904-112-07-101 motor. Both motor control units had switch selection of forward/reverse, on/off, and in addition the Slo-Syn unit had selection of four stepping speeds. Speeds of 1, 4, 40 and 400 steps per second could be selected, each step being 1.8 degrees of rotation on the motor shaft. The oscillator driving the Impex motor had a fixed speed of 50 steps per second, each step being six degrees. Both units could be switched from manual to microprocessor control, the control being from a five wire input in the case of the Impex unit. All seven wires were

connected to the peripheral interface at Port 6A of the microprocessor.

4:a(2) Crystal Angle Measurement

The angle between the crystal and the optical axis of the spectrometer was continuously monitored using a radial grating shaft encoder. Figure 4(10) shows a schematic of the detection system. The grating was supplied by Ealing Beck and had 4800 radial lines, a small fraction of which were projected onto a detection device so that they were magnified to a period of 23 millimeters. As the optical system was fixed relative to the optical axis of the spectrometer, when the grating was rotated the dark and light fringes projected onto the detection device moved across the detectors giving signals which were identical in amplitude but which were phase shifted. The detection devices were two light sensitive switching transistors separated by 8 millimeters, each transistor being collimated by a 2 millimeter diameter circular aperture. This arrangement produced a simple way to decode the detector signals. Each groove on the radial grating was associated with a number from 0 to 4800 and 0 was selected so that the crystal was normal to the spectrometer axis. From figure 4(10) (View from A) it can be seen that if the radial grating is stationary the decoder will have in its memory the number which uniquely defines the last light fringe encountered but if the disc is now rotated, when a new light fringe appears the decoder has to recognise if the disc has been travelling clockwise or anti-clockwise. The decoder adds or subtracts one from the total in memory when a new fringe appears depending on whether the disc was travelling clockwise or anti-clockwise. A direction change would be detected if a level change (i.e. light to dark or dark to light) occurred sequentially in the same channel. If the disc were rotating in one direction only, level changes would occur first in one channel

and then in the other. This simple detection system would however introduce cumulative errors as detected transitions should be from dark to light for clockwise rotation and light to dark for anti-clockwise rotation. Thus, if the decoder sensed sequential level changes in one channel then the direction of the current detected transition would be reversed. The logic circuitry used to do this is shown in Figure 4(8). The twelve bit binary output from the three cascaded 74LS 193 binary up down counters was fed to the motor control unit which had a twelve bit binary to four digit B.C.D. decoder and display. The twin channel optical detectors and associated high stability amplifiers (Figure 4(9)) were mounted together in a screened box to reduce the chance of transient pickup and were linked to the decoder module mounted less than six inches away by double screened low noise cable. The detectors and decoders were run off a high capacity car battery which was connected to an automatic mains supply charging unit. This ensured that during a mains failure calibration of the device was not lost.

The use of an optical grating meant that great attention had to be paid to the overall mechanical stability of the system. For the rotation of the grating high precision phosphor bronze bearings were used giving a sideways play of less than one ten thousandth of an inch. All the optical components were mounted in a magnesium alloy frame to give high rigidity. The whole shaft encoder assembly was covered by an aluminium cylinder closed at one end and painted with optical black on the inside to act as a light shroud and protective covering.

The unit was found to exhibit no drift over several weeks of testing and could count accurately up to eighty fringes per second, four times the required maximum.

The job of Unit 1 in the system was to convert the 0V to 10V signal from the electrical micrometer to a digital signal, to format this signal and the binary signal from the counter for transmission to Unit 2, the digital recorder. The flow of information to Unit 2 was in serial ASCII Form but also a parallel output existed for the microprocessor interfaces. The sampling period of the system was determined by a crystal controlled ten second gate in the counter, which was modified to give a six digit B.C.D. output and a data ready signal. The data ready signal was necessary as the B.C.D. output was unlatched and gave the count as it was being accumulated. The accumulation cycle lasted for ten seconds followed by a one second display period. During this one second period, the data ready line would go to a logic 1 level (high). The circuit diagram of the counter half of Unit 1 is shown in Fig 4(12). The six digit B.C.D. output of the counter is connected to the inputs of six 74173 tristate buffers and the data ready signal from the counter is used to enable the 74173 input latches. Thus, by enabling the tristate outputs in turn, (when not enabled, tri-state outputs are high impedance) each digit in B.C.D. form appears on the output bus and is converted into ten wire decimal form. This ten wire signal is buffered and fed into a diode matrix which is constructed so that a decimal number input appears at the output as a seven wire ASCII signal. The timing for the serial conversion is provided by a master clock in Unit 2. A 74197 binary counter and a 74154 4 to 16 wire convertor acting together are used as a digit counter, and when the seventh digit pulse is received from the master clock an ASCII space is outputted. This also occurs after twelve digits, the gap of four digits between the spaces being for the 4 digit B.C.D. output of the analogue to digital convertor (Fig. 4(11)). This information is clocked onto the same bus for serial conversion as that from

the counter, again using tristate buffers. The inputs to the ten tristate buffers are looped to two output sockets on Unit 1 for connection to the microprocessor PIA's. Figure 4(11 shows the analogue to digital converter, binary to B.C.D. decoder and display and the associated tristate buffers for sampling. The input latch enable again comes from the counter data ready signal. The analogue to digital converter used was a Datel type EK-12B 12 bit device. Care was taken with the associated circuitry to achieve good long term stability and testing showed that the maximum drift was 1 bit in 4096 over many hours.

The unit therefore provided both a parallel B.C.D. output and a serial ASCII output of the two input signals, the serial output being a string of six ASCII characters for the accumulated count, a space, a string of four ASCII characters for the electrical micrometer and a space. The sampling of the data by the tristate buffers could be interrupted by a signal from the microprocessor which held the digit counter clear. The microprocessor signal could in turn be disabled by a switch on Unit 1 so that entirely manual data logging could be done.

4:a(4) Unit 2: The Digital Tape Recorder

The digital tape recorder consisted of a Memodyne type 816 tape transport, drive and formatting electronics together with an interface and timing electronics for Unit 1. The formatting was in ANSI/ECMA34 standard which allowed compatibility with Texas Instruments tape reading equipment. The interface to Unit 1 required the use of a 256 bit shift register memory to overcome the unusual timing requirements of the Memodyne formatting system. The system was made compatible with Texas Instruments tape readers as the University Central Computer facility was of this type and allowed very fast reading of tapes into direct access computer file space.

4:a(5) The A.C. Motor Control System

The traverse of the counter table, the rotation of the counter table, the rotation of the x-ray chamber about the crystal axis and the rotation of the crystal assembly were all powered by capacitor start a.c. motors. In the case of the latter, the motion was monitored by a radial grating shaft encoder as described in Chapter 4: a(3), and in the other cases by means of simple light chopper shaft encoders. These consisted of a disc with holes drilled at a fixed radius at a small separation, on one side of the disc there being a lamp and on the other side a phototransistor detector. As the measurement was done on the driving shaft, to ensure that the object being moved would always be in the correct position, movement was always from a known calibrated zero position. This eliminated backlash and always ensured a calibrated position. Figure 4(4) gives a schematic picture of the a.c. motor control system. In this system high precision knife edge microswitches were manufactured to a closing repeatability of 0.002 inches. All calibration measurements were done from an open to closed transition. At the other extreme of movement of the mechanisms from the calibrated position override sensing microswitches were fitted. The light choppers used RS type 305 - 435 switching transistors designed to give T.T.L. compatible output levels.

To reverse the direction of a capacitor start a.c. motor the neutral input has to be changed from one side of the capacitor to the other. If this is done instantaneously to a motor connected to a large gear reduction chain then damage can result both to the motor windings and the gears and it is therefore usual to allow the motor to stop before reversing the neutral feed. In the motor control system the reversing of the neutral feed was done using a Triac based switching circuit (Figure 4(7)). The triac control units had a two wire logic input by which forward

reverse or stop could be selected. The circuit works by having two triacs one connected to each side of the capacitor and fed by the mains neutral supply. If the logic inputs have states which correspond to an off option then both triacs are switched off. If either the forward or reverse options are selected either one or the other of the triacs will be switched on. Both triacs are never on together even when the logic inputs are removed. To protect the circuit from the large transients produced by this type of motor, 1200 volt triacs were used which were protected by surge limiting non-linear resistors. As the triac circuitry had to float at mains potential, logic signal inputs were made using optical isolators. These consisted of an infra-red transmitting and receiving diode pair which were electrically isolated from each other.

The manual operation of the four motors, the display of the shaft encoder positions and the automatic operation of three of the motors during operation of the override or calibration switches were all handled by the motor control unit. This consisted of three identical circuits to control operation of the counter table traverse, counter table rotation and x-ray chamber rotation, a similar circuit to control the crystal rotation and power supplies for the logic circuitry, shaft encoders and triac units. The operation of the systems associated with motors one, two and three were identical, each channel having reverse, stop and forward push buttons, a four digit position display and associated calibration and override microswitches. If the forward option was selected when the motor was travelling in reverse (or vice versa), the unit would first select stop, wait for three seconds and then select the option requested. This was to prevent motor or gearbox damage due to instantaneous changeover. If the stop option was selected while a motor was running any subsequent command would only be acted on after a three second delay. The

pulses from the shaft encoders were counted using an RS type ZN 1040E four decade decimal up down counter driver and displayed on seven segment displays. The up/down line to the counter was derived from the state of the logic output to the triac units. If a motor was left in a forward direction so that the mechanism being driven actuated the override microswitch, the motor control unit would select stop, wait for three seconds, reverse the motor direction and wait for the microswitch to close. At this point the control unit would select stop. This prevented any accidental damage to the spectrometer mechanism due to incorrect use. If a particular movement required calibrating, the reverse option was selected so that the mechanism moved towards the calibration microswitch. This was a normally closed switch and when the contacts were opened the control unit would select the off option, wait for three seconds, reverse the motor direction and wait until the microswitch contacts closed. On closing, the counter was reset to zero and the motor stopped. Any forward movement of the mechanism was now calibrated, the position being indicated on the motor control unit display. The logic diagram of the three identical motor channels is given in Figure 4(6).

The crystal rotation motor had its own associated radial grating shaft encoder (Chapter 4 a(2)) and so it was unnecessary to have circuitry for override and calibration microswitches. The logic diagram is given in Figure 4(5). The twelve bit binary output of the radial grating shaft encoder was decoded in the motor control unit using cascaded 74185 binary to B.C.D. decoders and displayed on four seven segment displays. The twelve bit binary output was also buffered and looped to an output socket on the motor control unit for connection to a microprocessor P.I.A.

4: a(6) The Microprocessor Hardware

The microprocessing system used was a South West Technical Products system based on the Motorola 6800 microprocessing unit (M.P.U.) This included the M.P.U. and associated timing electronics, eight thousand eight bit words of memory (8K bytes), provision for up to seven peripheral interface adaptors (P.I.A.'s), a serial interface for communication with a visual display unit (V.D.U.), provision for up to two more serial interfaces, provision for up to five 8K bytes of erasable programmable read only memory (E.P.R.O.M.) and a read only memory (R.O.M.) monitor program with an associated 128 bytes of random access memory (R.A.M.). The monitor ROM in a microprocessor system simply contains a program which allows an operator to examine and change the contents of memory locations using a VDU. The monitor program was changed to allow more complex memory transfer tasks to be executed.

The configuration of the microprocessing system is shown in Figure 4(2), and the addresses which the components correspond to are shown in Figure 4(3). Communication with the microprocessor through the VDU was handled by an Asynchronous Communications Interface Adaptor (A.C.I.A.) at Port 0 which operated as an RS232 serial interface running at 4800 baud. Port 1 contained an ACIA working in the same manner but running at 1200 baud and was connected to the Cyber 73 university main frame computer. The Port 0 interface ran at a higher speed than the Port 1 interface because if the system allowed information to be transmitted from the Cyber 73 to the VDU with the VDU interface at Port 0 running at a nominal 1200 baud, characters would occasionally be lost due to the Port 0 baud rate oscillator slowing relative to the Cyber 73 baud rate oscillator. By using a substantially faster speed on Port 0 this problem could not occur. As the memory and function map shows (Figure 4(3)), the next highest addresses above the two serial

ports were occupied by eight PIA's which allowed the microprocessor to communicate with parallel encoded peripheral devices. The functions of each PIA are shown in Figure 4(3), and it can be seen that some were used as inputs and some as outputs. The PIA's were simply bi-directional data buffers in that they utilised latched inputs connected to the data bus and latched outputs connected to a peripheral device. If the PIA was being used as an output, information from the data bus would be dumped at the address of the PIA data register. Execution of a monitor program would then transfer the information from the latched input register to the latched output register. The PIA's had to be hardware configured as either inputs or outputs and this selection had always to agree with the software selection contained in the status register of the PIA. As shown in Figure 4(3), the next highest address was occupied by 4K bytes of EPROM, which was used for the permanent storage of the monitor and control software. The devices used were type Texas Instruments TMS 2708L. The purpose of the EPROM was to provide non volatile storage for the monitor program and control program so that restarting the system after a power failure was automatic. At higher addresses in memory was a section of RAM for use by the monitor program only.

Thus, under control of software located either in the main RAM memory or in EPROM, the microprocessor could drive the stepping motors using the PIA at Port 6A, inhibit the transmission of information to the digital recorder using the PIA at Port 6B, or interrogate the crystal position decoder, the accumulated counts, the electrical micrometer decoder and the state of the data ready line.

4:a(7) The Microprocessor Software

The main control software used is reproduced in assembled

form in Appendix A. Once loaded into memory it could be run by starting execution at address \$0100. The routine then issued information on the available routines and issued prompts to indicate how to use particular routines so that to operate the system a user did not have to have any knowledge of microprocessors or assembly language programming. Six routines were written ranging from a simple counter calibration procedure to automatic point to point scanning and dumping of data to both cassette and the Cyber 73. The control software allowed the addition of up to three more control sub routines without any alteration to the overall program layout. All programs were written in Motorola assembly language for compactness and speed of execution.

Part (b) The X-Ray Photon Detection System

The detection system used for the spectrometer was similar to that used for most soft x-ray work, except that particular attention was paid to reducing the background noise level to an absolute minimum. The background noise level is made up of counts due to cosmic rays passing through the counter, counts generated in the charge sensitive preamplifier and counts produced by noise in the counter and signal lead. It was found that in the energy region of interest (one to ten KeV) the main source of noise was the counter and associated signal lead. In most soft x-ray spectrometers, connection to the gas flow proportional counter is made using a screened high voltage coaxial connector which has to carry several kilovolts to the central counter wire. If the vacuum surrounding the counter is sufficiently good, connections can be made in the high voltage coaxial line. In the spectrometer described in Chapter 3 however, a vacuum of only 0.1 torr was achievable due to the type of construction and materials used. At this pressure the sparking potential of air is sufficiently low to cause arcing between any high voltage point and earth. During subsequent testing in a separate vacuum system it was

found that only at pressures below 0.025 torr could exposed high voltage connectors be used without causing intermittent discharging. It was also found that the counter background noise level was dependent upon the smallest traces of dirt or dust in the counter and on the type of material used in the construction of the counter itself. As an example the use of perspex in the high voltage feedthroughs caused an increase in noise of a factor of thirty compared to the final design. The counting electronics consisting of a charge sensitive amplifier, main amplifier, ratemeter, single channel analyser and counter were completely conventional, the amplifier, single channel analyser and ratemeter being manufactured by Ortec and the counter by RCS electronics. The testing of the system was done using a Tracor Northern multichannel analyser working in pulse height analysis mode and irradiating the counter with a radioactive source so that the energy spectrum of the counter could be observed. Using an Fe 55 source and an argon methane counter gas mixture two peaks appear in the energy spectrum the higher energy peak corresponding to the detection of manganese $K\alpha$ radiation at 5.98 KeV and the lower energy peak being due to $K\alpha$ excitation in argon at 3.0 KeV. Thus the separation of these peaks gives an absolute energy scale and so the energy resolution of the counter can be measured by measuring the width of the higher energy peak.

4: b(1) The Gas Flow Proportional Counter

The counter was of cylindrical construction as shown in Figure 13. The stainless steel counter body had a 2.5 mm wide 10 mm deep slot cut in it to allow x-ray photons to enter the counter and stainless steel end caps welded on at both ends. The inside surfaces of the counter were machined to a high finish and then etched prior to polishing to a mirror finish. The counter

body and end caps were welded in an inert gas atmosphere to prevent oxidation and great care was taken to ensure that dirt did not enter the counter at any stage. The gas pipes were welded in before the end caps so that any roughness produced in the counter wall could be easily polished out. Glass insulators with a central hollow nichrome tube were used as high tension feedthroughs, and these were glued onto the counter end caps using a low vapour epoxy resin, type AT 101. The assembly was then baked at 60°C for six hours. The detector wire was eight micron diameter gold coated tungsten wire (Luma) which was fed through the counter and soldered to the nichrome tubes at each end of the counter using a solder paste. Both stainless steel end sleeves were then pressed into position and the cable clamp and wire fitted. The high voltage wire was then soldered and crimped to one of the nichrome tubes. The whole assembly was then ultrasonically cleaned in butyl alcohol and baked at 60°C for twelve hours. To prevent discharges from the high voltage nichrome tubes, each end of the counter was encapsulated in a commercial high voltage potting material. (Solithane 113, manufactured by Thiokol, New Jersey, U.S.A.) The potting mixture was vacuum degassed to remove absorbed air before use and each encapsulation was baked for twelve hours at 60°C . In testing prototype counters it was found that microphoney effects caused induced noise in the charge sensitive amplifier due to loosely bound earth braid moving causing the cable capacitance to alter. This was overcome in the final design by using miniature cable with a very tightly woven earth braid consisting of silver plated copper strands and a PTFE dielectric.

The counter was found to have a proportional region 250 volts wide centred on 1200 volts with an upper noise level corresponding to photon energies of 300 volts. If all pulses

above 500 volts were counted the background count rate was given by a poisson distribution peaking at 0.12 counts per second. The width of the manganese K line using an iron 55 radioactive source expressed as a percentage of the peak energy was 16.5% using a 90% argon 10% methane counter gas which was used throughout this work.

4:b(2) The Detection Electronics and Gas Supply System

A schematic diagram of the detection electronics and gas supply system is given in Figure 13. The electrical connection to the counter was made outside the vacuum tank and a double screened coaxial cable was used for connection to the charge sensitive amplifier which was mounted as close as possible to the termination point. The high voltage supply to the charge sensitive pre-amplifier and counter wire was from a modified Ortec 0 to 5KV power supply which had extra smoothing and transient suppressing components. Pulses from the preamplifier were amplified using an Ortec spectroscopy amplifier which had adjustable rise and fall time constants for the rejection of transients, and pole zero cancellation for accurate fast counting. Amplified pulses lying within the acceptance window of a single channel analyser generated TTL compatible signals which were counted by an RCS electronics counter. A Tracor Northern multichannel analyser used in pulse height analysis mode was used as previously described to examine the energy resolution of the system.

The gas supply system bled a constant low volume supply of argon methane mixture through the counter, the argon being the detector gas and the methane the quenching gas. As the counter window was made of ten micron thick polypropylene, there was a chance that the window could rupture and so the counter gas would be pumped into the vacuum system. This was prevented by using

an anti suckback valve and by having a valving arrangement which allowed the counter to be evacuated when not in use so reducing the strain on the thin window material. The counter window itself was glued in position and prevented from tearing off by a cylindrical rubber backed clamp.

The counter system was almost completely noise free and counting rates up to 10^5 counts per second were recorded with no limiting. The energy resolution of the counter was almost the same as the theoretical maximum for this type of counter and long term statistical tests revealed no perceptible long term sensitivity drift.

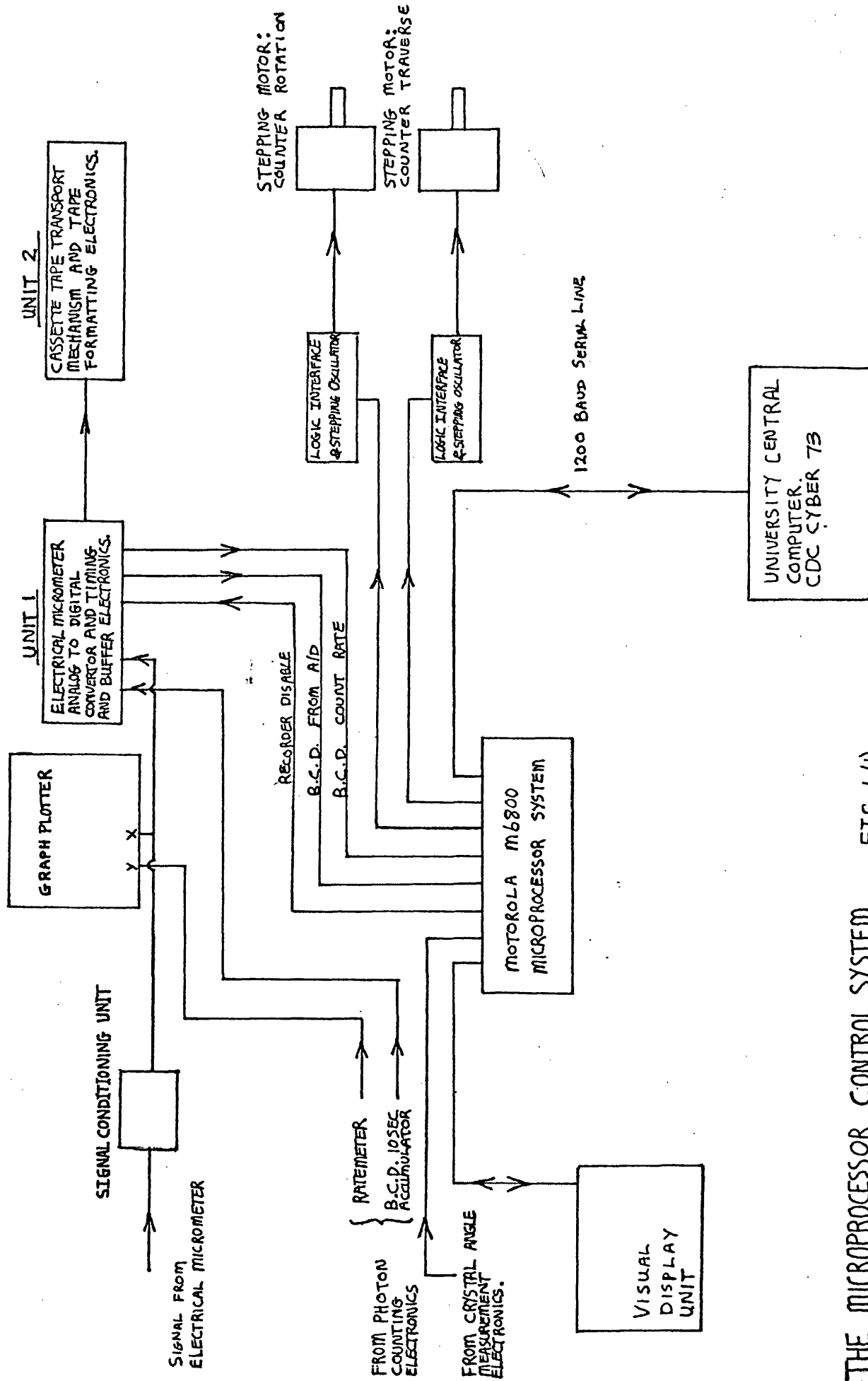
Part (c) Operation of the Spectrometer Detection and Control Systems

This section describes the setting up of the spectrometer to scan a particular wavelength region using the microprocessor controlled data acquisition system. The Bragg angle was set by moving the correct number of light fringes as registered on the optical encoder from the zero position, which corresponded to the crystal being normal to the spectrometer optical axis. Each number registered represented 4.5 minutes of arc and to obtain a calibrate measurement the crystal was always rotated back by one degree and then forward by one degree to remove backlash from the encoder coupling. As the counter rotation, counter table and x-ray chamber all had calibration points of known position and shaft encoders, the geometrical relations in Chapter 3 could be used to set their required positions using the motor control unit. The counter could now be driven to a position on the optical axis of the spectrometer and rotated to optimise the signal. As the counter slits were on the centre of rotation of the counter and were finely ground to a V shape the dependence of the count rate on counter angle was **only** a slowly varying function.

With the counter set on the optical axis, the

count rate was finally optimised by rotating the x-ray chamber about the crystal chamber axis. To scan the particular wavelength region required, the required acquisition program could be selected which in a typical case would traverse the counter, rotate the counter, log data onto magnetic tape and dump data into the main computer file store.

During the course of this work the software routines were continually altered to suit particular experimental needs. For example, during the work on ytterbium metal a routine was added which allowed multiscanning of a small section of wavelength. This was easily written and implemented using existing sub routines and without altering the program structure. The system was therefore very flexible and allowed expansion without large software or hardware alterations. The system could quite easily have been expanded to control the motor and encoder systems and the x-ray gun if that had been necessary. After transfer of data to the main computer, the ability to be able to perform simple analysis within typically fifteen minutes was found to be very useful and was often used to dictate the course of a set of experiments.



THE MICROPROCESSOR CONTROL SYSTEM. FIG 4(1)

PERIPHERAL INTERFACE ADAPTORS (PIA)

INTERFACES TO PARTS OF THE DATA ACQUISITION & CONTROL SYSTEMS

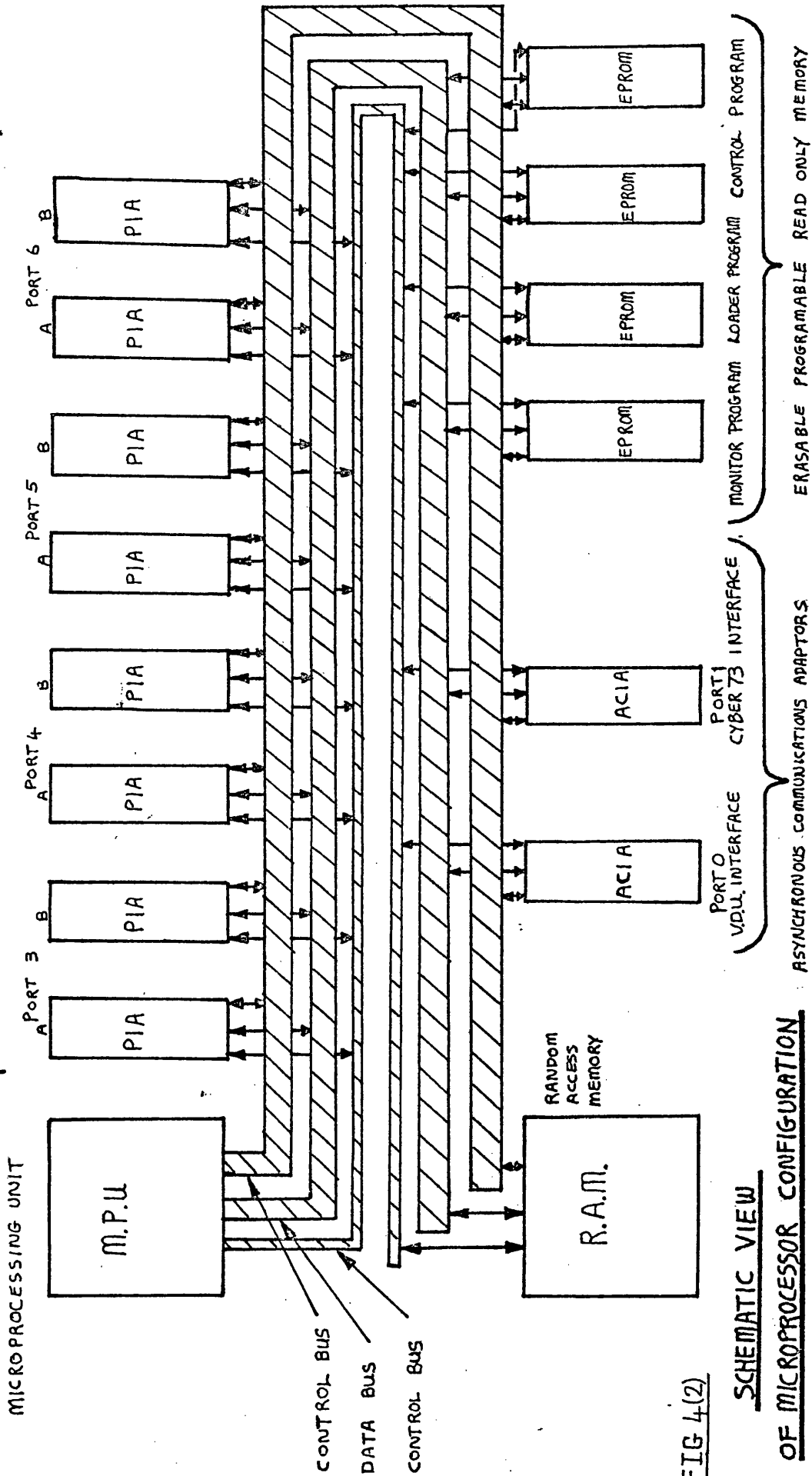


FIG 4(2)

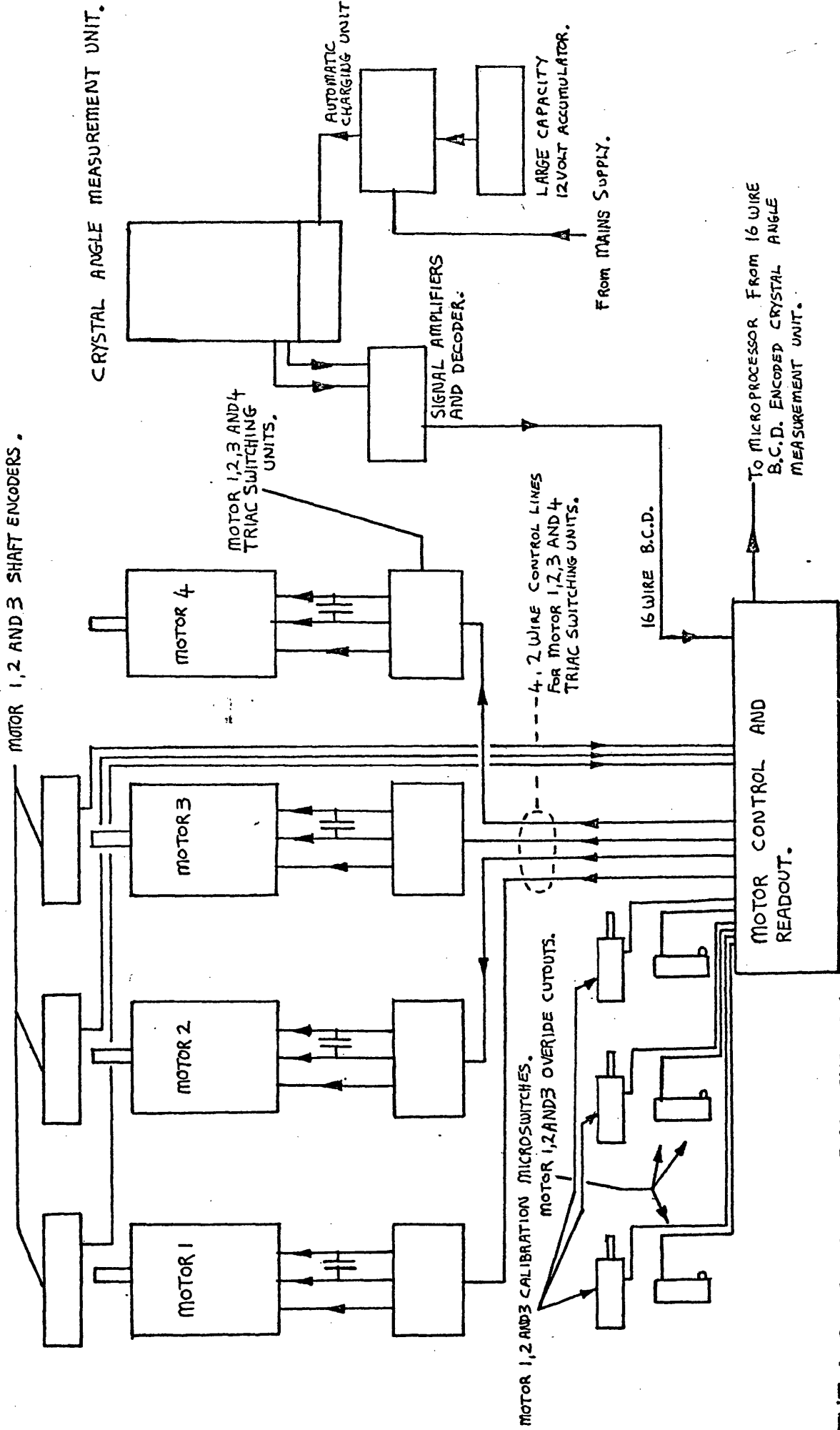
SCHEMATIC VIEW

OF MICROPROCESSOR CONFIGURATION

<u>Address</u> (Hexadecimal)	<u>Device</u>	<u>Function</u>
§ A080		
§ A000	RAM	Memory for monitor and loader
§ EC00	EPROM	Control program
§ E800	EPROM	Control program
§ E400	EPROM	Loader program
§ E000	EPROM	Monitor program
§ 8020 Port 6B	PIA	Output to enable on recording unit
§ 8018 Port 6A	PIA	Output to stepper motors logic controller
§ 8016 Port 5B	PIA) Input from digits 1,2,3,) and 4 of the analog to) digital convertor
§ 8014 Port 5A	PIA	
§ 8012 Port 4B	PIA) Inputs from digits 1,2,3,) and 4 of the counter)
§ 8010 Port 4A	PIA	
§ 800E Port 3B	PIA	Input from display command line in counter
§ 800C Port 3A	PIA	Input from digits 5 and 6 of the counter
§ 8004 Port 1	ACIA	1200 Baud serial interface to university computer (Cyber 73)
§ 8000 Port 0	ACIA	4800 Baud serial interface to visual display unit
§ 1FFF		
§ 0000	RAM	Main working memory

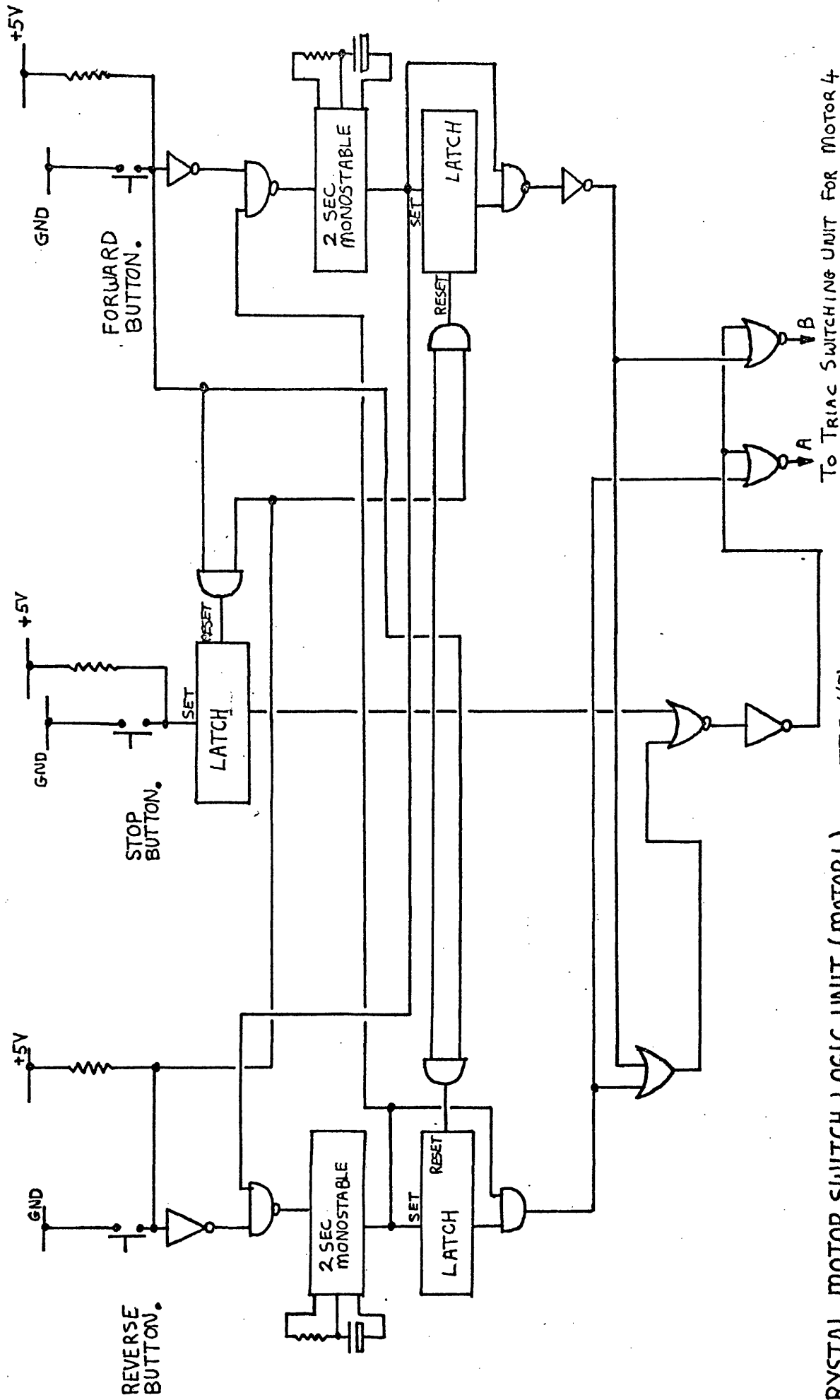
MICROPROCESSOR MEMORY AND FUNCTION MAP

FIG. 4(3)



THE A.C. MOTOR CONTROL SYSTEM

FIG 4(4)



CRYSTAL MOTOR SWITCH LOGIC UNIT (MOTOR 4)

FIG 4(5)

To TRIAC SWITCHING UNIT FOR MOTOR 4

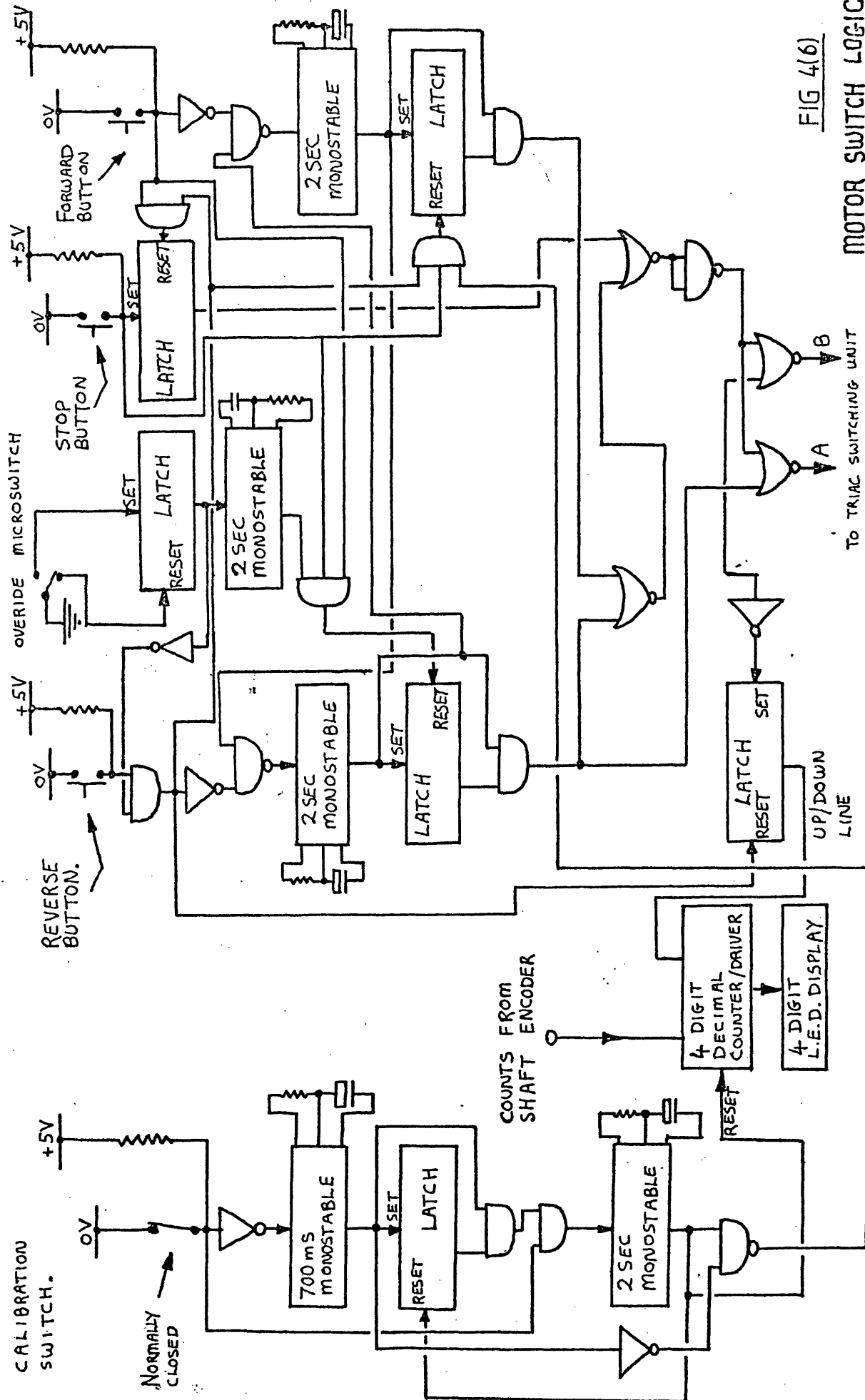


FIG 4(6)

MOTOR SWITCH LOGIC

TO TRIAC SWITCHING UNIT

UNIT AND SHAFT ENCODER DISPLAY. (MOTORS 1,2 AND 3)

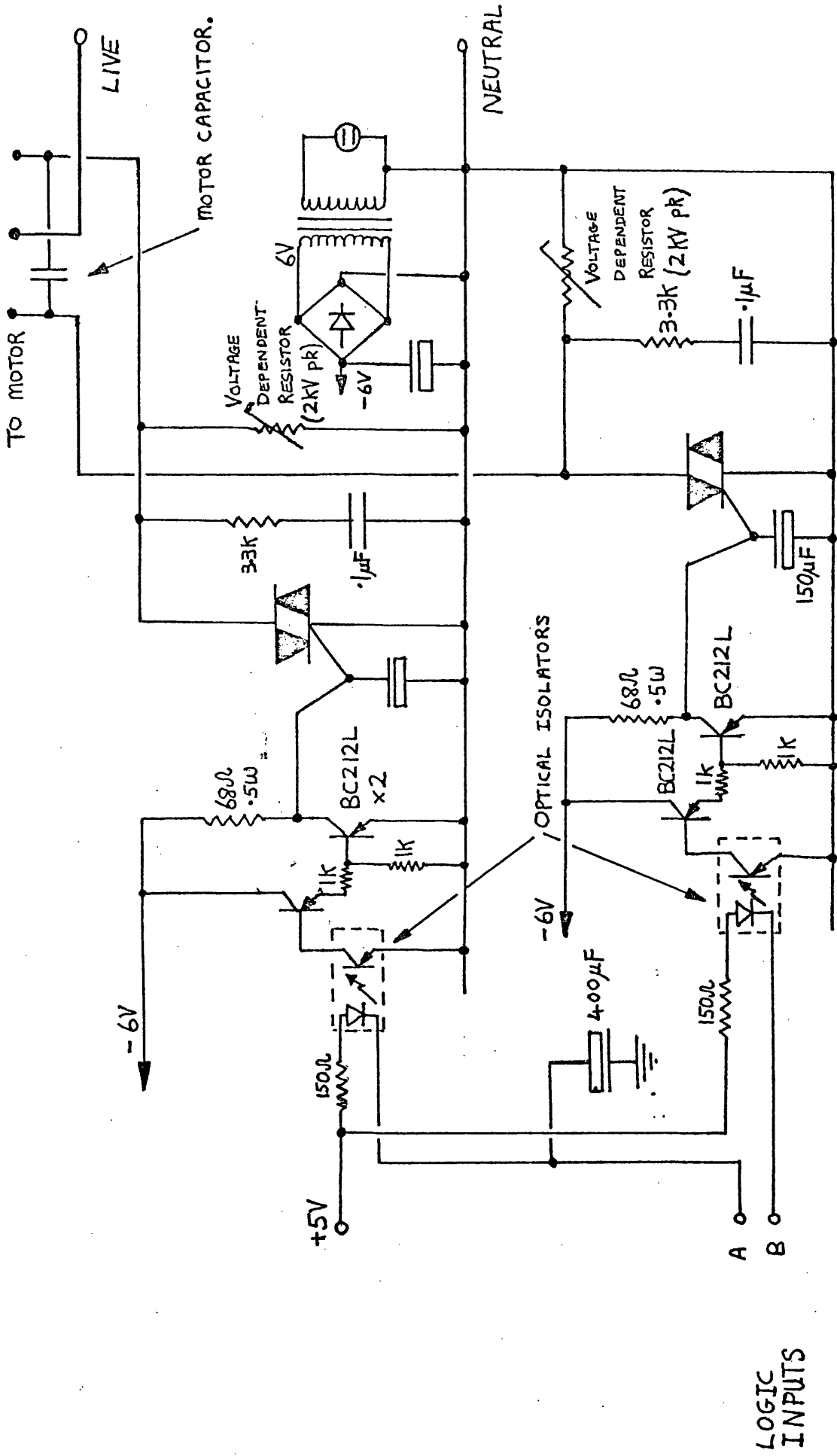
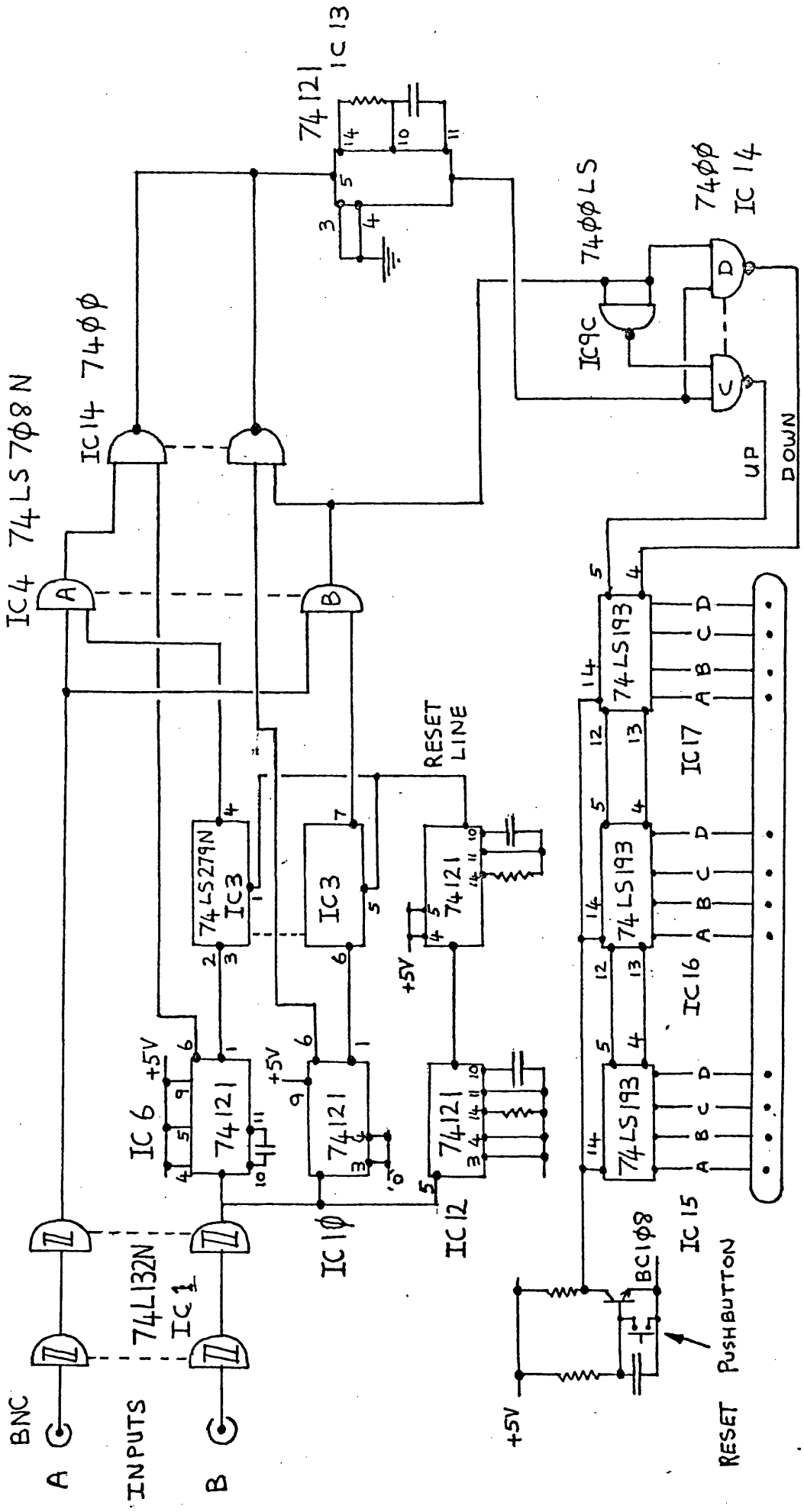
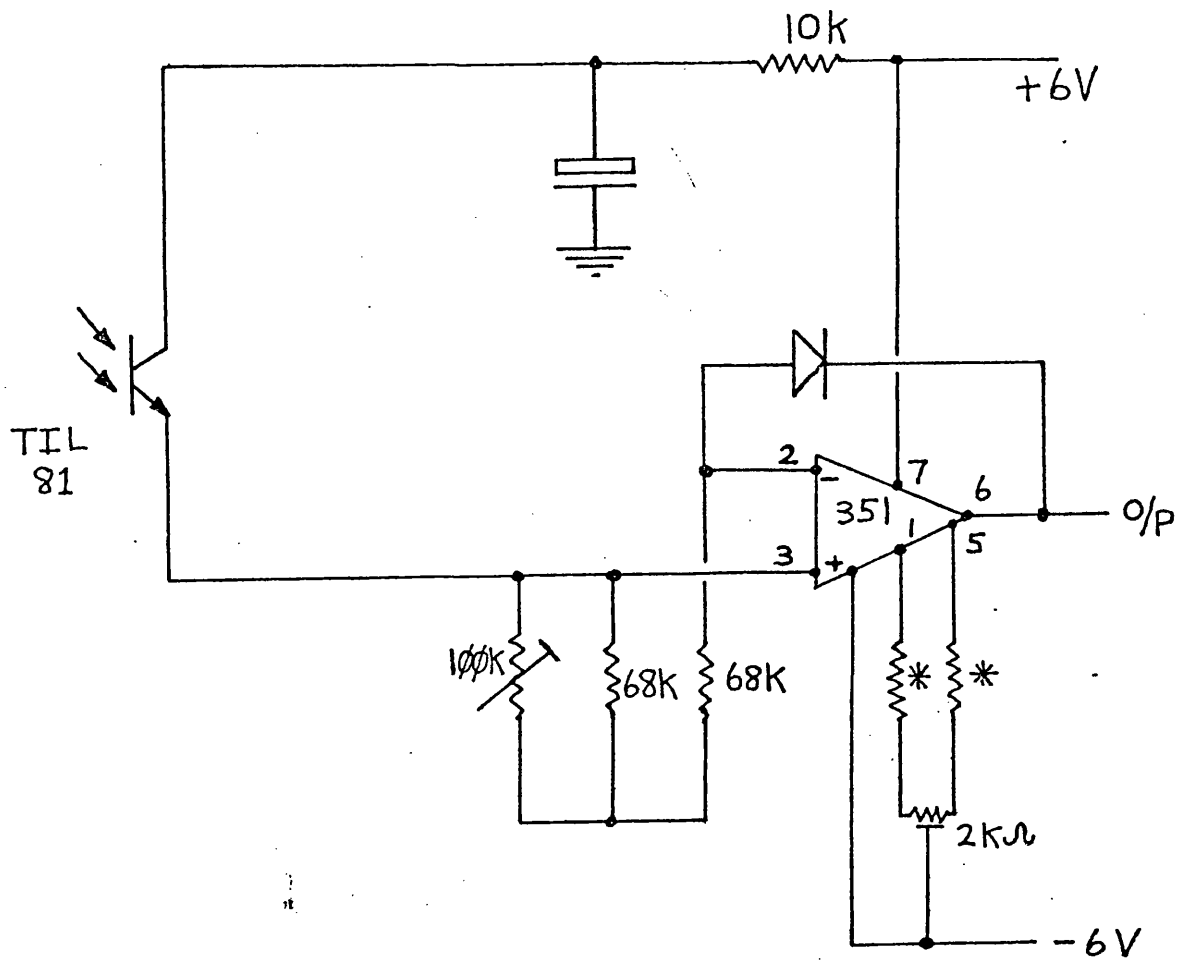


FIG 4(7)
TRIAC CONTROL UNIT FOR A CAPACITOR START A.C. MOTOR



D TYPE SOCKET
12 BIT BINARY OUTPUT

CRYSTAL ANGLE MEASUREMENT DECODER FIG 4(8)



* TEMPERATURE DEPENDENT RESISTOR

LIGHT DETECTOR AND SIGNAL AMPLIFIER FIG 4(9)

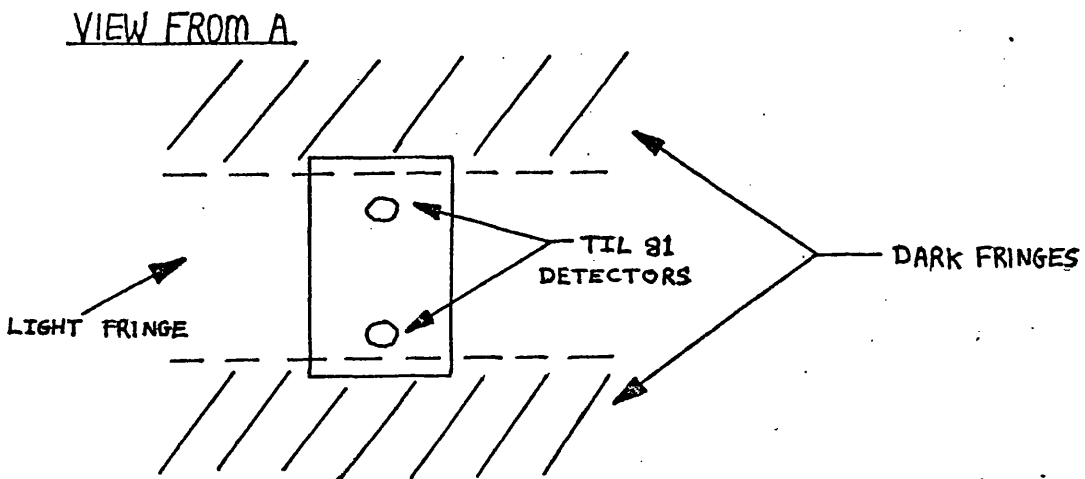
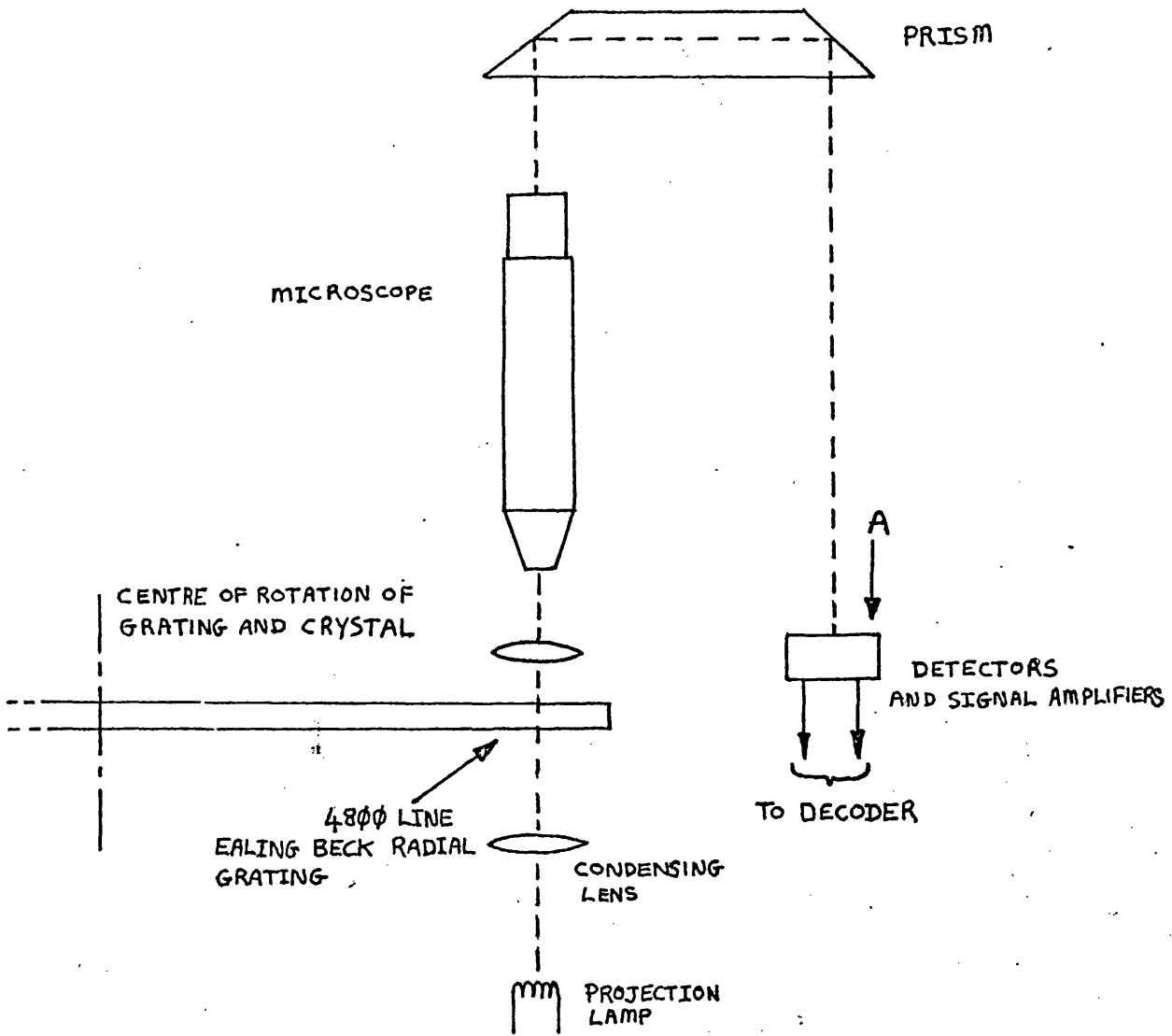
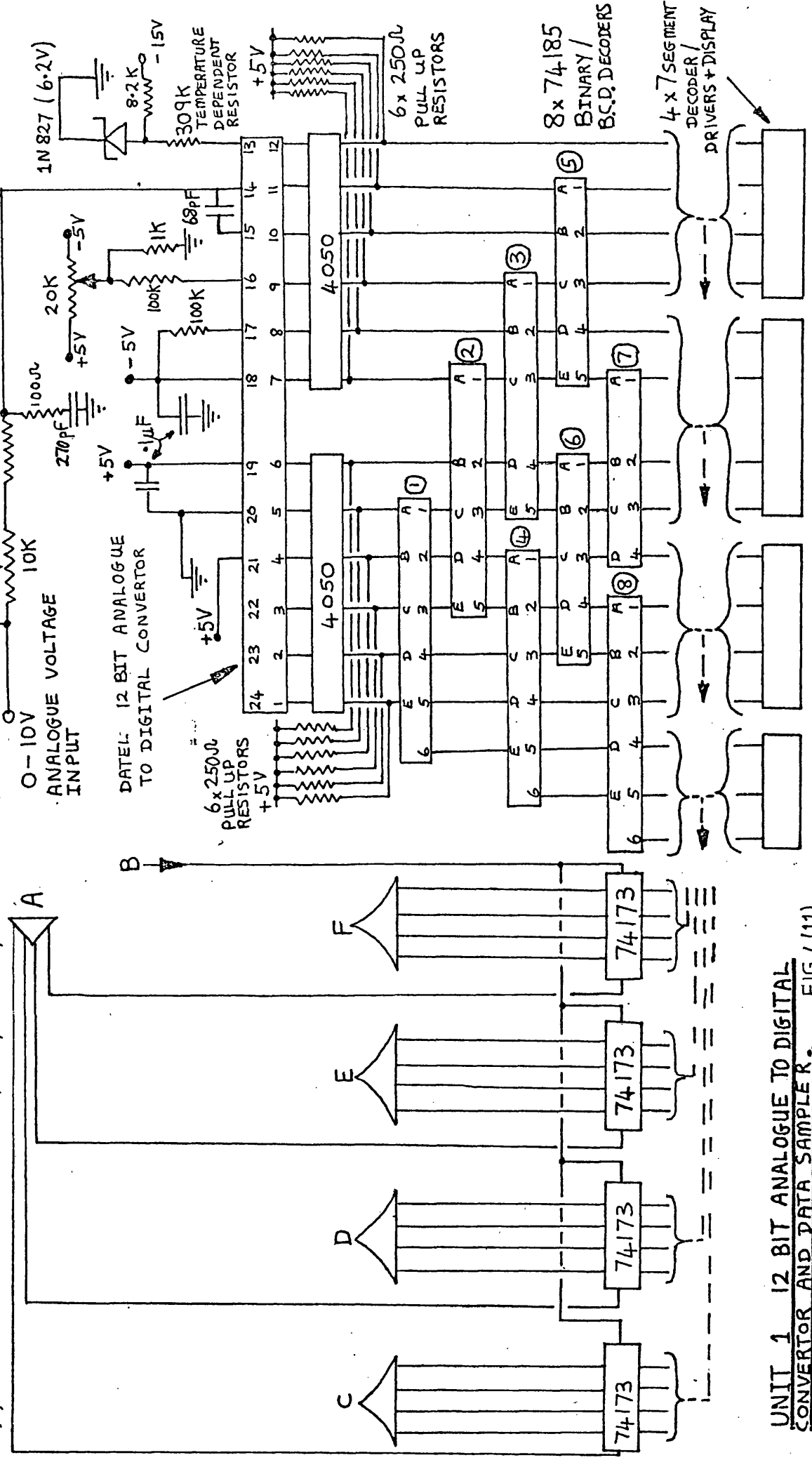


FIG 4(10)

DETECTION SYSTEM OF RADIAL GRATING SHAFT ENCODER.

A & B TO TIMING ELECTRONICS IN UNIT 1.
 C, D, E AND F FROM TRI-STATE BUFFERS (74173) TO B.C.D. DECIMAL DECODERS IN UNIT 1.



UNIT 1 12 BIT ANALOGUE TO DIGITAL
 CONVERTOR AND DATA SAMPLER. FIG 4(11)

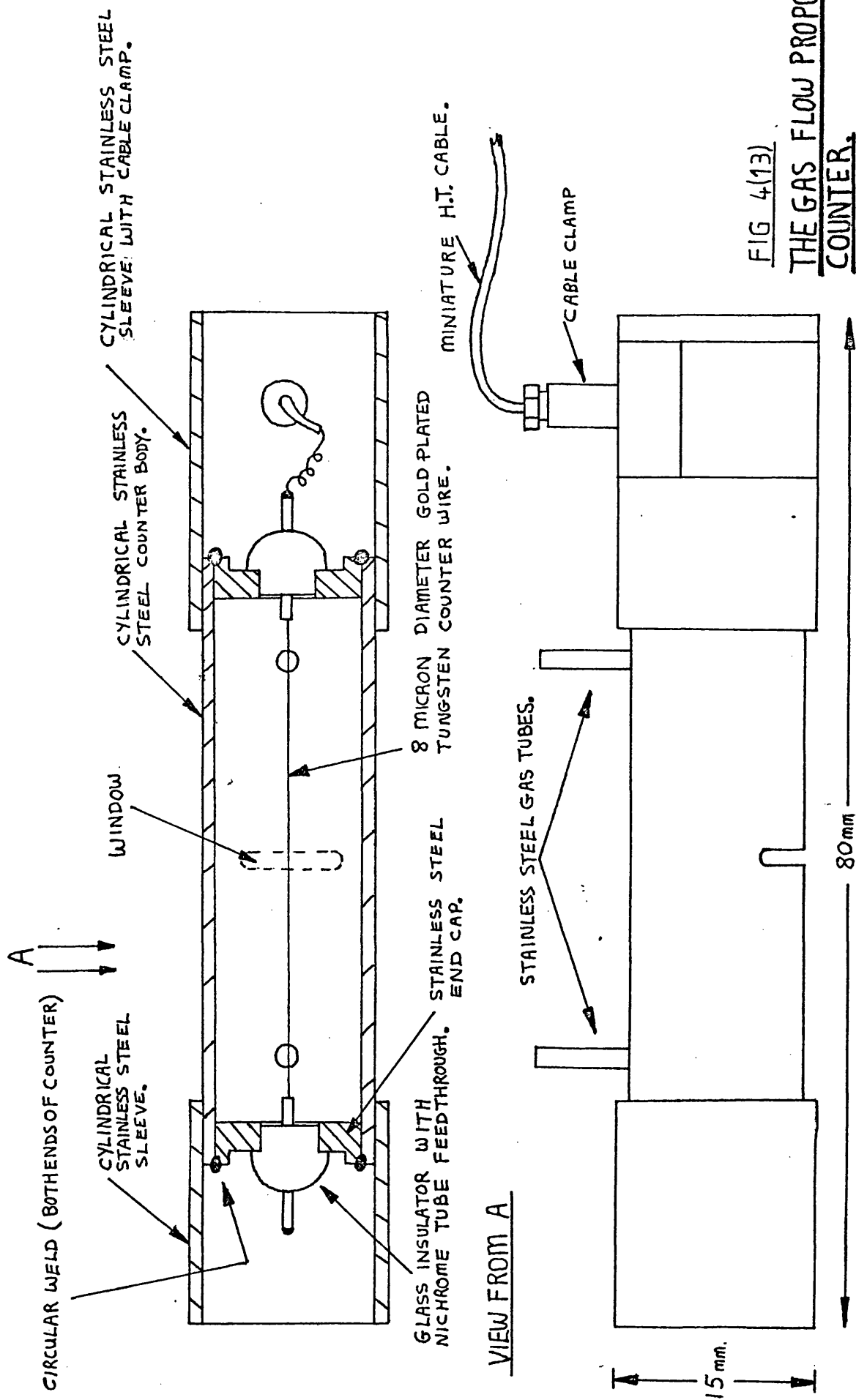


FIG 4(13)
THE GAS FLOW PROPORTIONAL COUNTER.

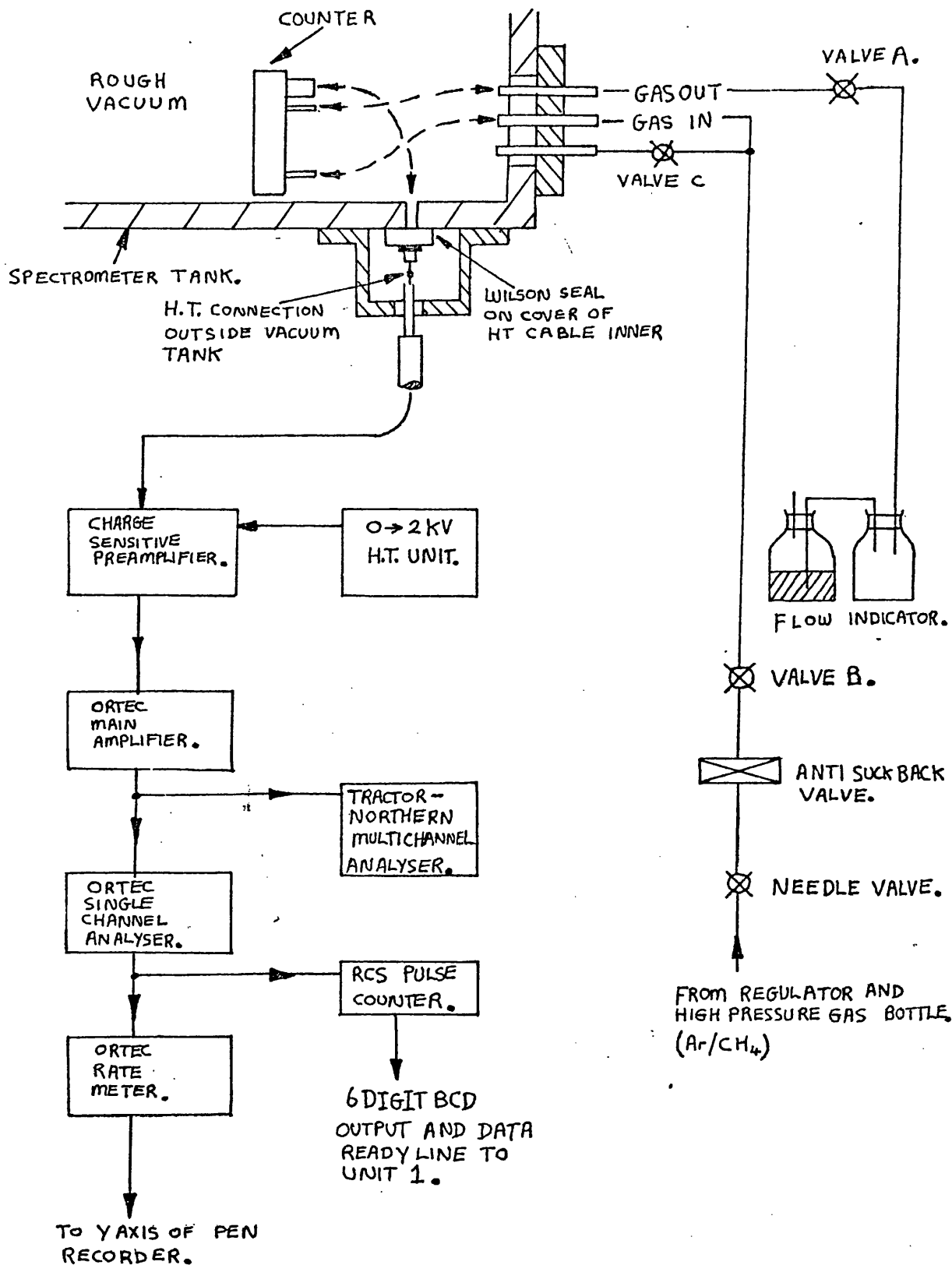


FIG 4(14)

COUNTER DETECTION ELECTRONICS AND GAS SUPPLY SYSTEM.

CHAPTER 5

Experimental Techniques and Results

	<u>Page No.</u>
Introduction	90.
5:1 Donconvolution of self absorption effects in the spectra of the rare earths.	92.
5:2 Treatment of data.	94.
5:3:1 The m_{α} emission spectrum of ytterbium metal.	96.
5:3:2 The $m_{\alpha,\beta}$ emission spectra of ytterbium in ytterbium fluoride	98.
5:3:3 The $m_{\alpha,\beta}$ emission spectra of lutetium in lutetium fluoride.	100.
5:3:4 The $m_{\alpha,\beta}$ emission spectra of thulium metal.	101.
5:3:5 The $m_{\alpha,\beta}$ emission spectra of thulium in thulium fluoride	101.

CHAPTER 5Experimental Techniques and ResultsIntroduction

The $m_{\alpha,\beta}$ spectra of lutetium in lutetium fluoride were recorded first in this work using the spectrometer described in chapters three and four. This was because lutetium fluoride is a stable compound which was easy to evaporate and did not suffer from marked decomposition under electron bombardment in vacuum. Lutetium in lutetium fluoride has a full $4f$ shell and therefore was not expected to show overlapping line absorption. For this system therefore sample preparation was easy and no correction had to be made for self absorption. During the course of the work on lutetium, the properties of the electron gun and target arrangement were investigated. As the vertical aperture of the crystal and detector was limited to give good energy resolution, this corresponded to an effective vertical aperture on the sample surface. The electron current flowing to the sample was stabilised as described in Chapter 3, but as the beam voltage was altered, although the beam current remained stable, the current density distribution on the sample could alter. The absolute amplitudes of features in the spectra could therefore not be measured as a function of beam energy, only the ratio of intensity of spectral features could be compared as a function of beam energy. This was due to the electron beam being relatively broad in the vertical direction instead of being a line of less than the vertical aperture defined by the crystal and detector. The work on ytterbium fluoride and thulium fluoride was similar to that for lutetium fluoride except that account had to be taken of self absorption due to the presence of overlapping spectral lines. A procedure to eliminate self absorption was developed for the simple case

of ytterbium fluoride where only one symmetrical absorption component was expected. The same procedure was then adopted for thulium fluoride where three components were expected. The procedure for removing self absorption features is described later in this chapter. The spectra of metallic ytterbium and thulium were difficult to record due to ageing of sample during the length of time needed to record the profiles to a high enough statistical accuracy. For both metallic thulium and ytterbium a technique was developed in which after a new thick metallic layer had been evaporated, a very small wavelength region was recorded to a good statistical accuracy and then a well defined feature was recorded to at least the same statistical accuracy. In this way a spectrum was constructed from many normalised recordings over very small wavelength regions. These spectra were significantly different from the best fresh metal film data. The reliability of the fresh film data was assessed by recording first from low to high energy and then after the evaporation of a new film recording from high to low energy. In this way, the same energies in the two data sets corresponded to different film ages. The data recorded for ytterbium and thulium in both the metallic and compound state were treated using a suite of computer programs that were developed to allow interactive data analysis of rare earth spectra. The programs included many generally applicable routines such as fast fourier filtering and deconvolution of overlapping spectral lines but also included specific routines such as self absorption deconvolution.

5:1 Deconvolution of self absorption effects in the spectra of rare earths

As previously discussed, self absorption effects in rare earth materials can give seriously distorted emission spectra. Fig. 5:1 shows the geometry of excitation and absorption. An electron at an incidence angle θ to the sample surface penetrates the surface and interacts with an atom at O to produce an x-ray photon which emerges from the surface at an angle ϕ . During passage from the interaction point O to the surface, the x-ray photon can be reabsorbed. This is important in rare earth materials as the $M_{4,5}$ absorption lines overlap the region of the $m_{\alpha,\beta}$ emission lines. The extent of the self absorption depends on the primary beam energy, the electron incidence angle, the x-ray take off angle and the sample thickness. The primary beam energy determines the effective penetration length λ_0 , this length increasing with beam energy. It is therefore advantageous to operate as near threshold as possible while still having a reasonable data rate. To minimise the distance an x-ray photon has to travel to reach the surface, the electron incidence angle should be near ninety degrees, so that electrons only penetrate very small distances. In order to further reduce the distance the x-ray photon has to travel to the surface, the emission angle can be decreased to zero so that detected photons only emerge normal to the surface. The sample can also be made thin in an attempt to further reduce the effective penetration depth. Although the effects of self absorption can be minimised using these techniques, the extent of self absorption under these conditions is unknown.

Using the electron gun and anode described in Chapter 3 it was possible to study the self absorption features as a function of entrance and emission angles. In principle, the probability of an absorption event occurring should be (Fig. 5:1),

$$P \propto 1 - e^{-at}$$

$$\text{where } t = L(E) \cdot \frac{\cos \emptyset}{\cos \Theta}$$

a is related to the mass absorption coefficient and is therefore wavelength dependent.

t is the average absorption path length.

\emptyset is the incident electron angle.

Θ is the take-off angle.

E is the energy of the incident electron beam.

L is the average penetration depth of incident electrons.

P is the self absorption probability.

In practice both the emission and incidence angles are broadened due to the angular spread of the electron gun and the collection geometry of the curved crystal spectrometer. In both cases the angular spread was less than $\pm 5^\circ$. Equation 5(1) represents an idealised case where there is a fixed interaction depth L which is a function of electron energy. In reality the interaction length can be a large spread centred on the average L . The form of the function describing the interaction length has been described by Packwood (1981) and a method of deconvolution using this function has recently been successfully applied (Crisp, 1983). By correcting for the alteration in electron density on the target as a function of incidence angle, the self absorption component could be extracted from the data by varying \emptyset and Θ . By measuring the extent of the self absorption component at several angles it was hoped that the measurement could be extrapolated to give conditions of zero self absorption. It was found that equation 5(1) did not hold in practice due to the microscopic roughness of the surface. If the average penetration depth was not very much longer than the average surface roughness then there would be an effective non zero minimum self absorption at any incidence or emission angle.

The fit of the measured self absorption to equation 5(1) was improved by repolishing the sample target to a very good optical finish. At grazing incidence electron angles the range in magnitude of the self absorption component as a function of emission angle was such that a reasonable fit could be obtained to equation 5(1). In subsequent experiments the data rate was improved by working at low incidence angles knowing the magnitude of the self absorption component to be removed. It was found that the absolute magnitude of the self absorption component was not reproduceable between evaporations. This was probably due to different types of crystal growth being formed giving differing island or defect sizes. The absolute levels of self absorption were much more reproduceable after the sample anode had been cleaned by heating to over 1000°C as described in Chapter 3.

5:2 Treatment of data

The data presented in this chapter represent two different types of data processing. The data for lutetium in lutetium flouride are presented with no filtering or smoothing, only with vertical error bars marking the standard deviation of a series of values taken for each energy increment. No attempt was made to examine whether a series of values representing a single data point corresponded to a normal error distribution and no attempt was made to correlate the measured rise and fall rates between adjacent data points with the experimental band width. These procedures were adopted however for all the data for ytterbium and thulium both in metallic and compound form. The comparison of the very large changes between the ytterbium and thulium spectra with the lutetium spectra did not require any enhancement whereas the small features observed within the ytterbium and thulium spectra themselves and also for comparisons between the two required detailed statistical treatment.

The data collection method used for the metals is described later in this chapter. The data collection algorithm used for ytterbium and thulium flouride was the same. Once the level of statistical accuracy required had been established, the computer system calculated the total number of events per channel which represented a normal error distribution. This was usually then divided by a hundred and the system would stay recording numbers of events recorded in ten second intervals until the minimum figure had been established. The computer would then increment the counter position and then repeat the procedure until the full energy range had been covered. The whole procedure would be repeated a hundred times when the required number of events per channel would be reached on average. For each energy position the data sets consisted of up to a hundred bins, each containing several individual measurements. Each bin was analysed in terms of a normal error distribution for short term non statistical noise and the bins themselves were examined for long term drift (Tukey, 1977; Eadie, 1971). The response of the spectrometer was modelled using a digital filter technique, the bandwidth of the filter representing at the high frequency end the maximum resolving power and at the low frequency end a constant background. A fast Fourier transform method was used in conjunction with a Hanning bandpass function (Brigham, 1974) to model the spectrometer response. Considerable enhancement of the signal to noise ratio was achieved by the application of these techniques. An attempt was made to deconvolute some of the spectra, particularly ytterbium flouride and thulium metal, into overlapping component lines. The standard techniques of least squares minimisation and Fourier deconvolution (Stone, 1962; Carley, 1979) were both applied to these spectra but were found to be unsatisfactory. The range of possible solutions for these heavily overlapped lines was too large to be of use and these techniques although widely

applied in photoelectron and infrared spectroscopy have to be used with caution. For the Fourier filtered spectra, no best fit line was used as the cubic spline or polynomial techniques commonly used can distort the data and in this case the spectral features are easily distinguishable.

5:3:1 The M_{α} Emission Spectrum of Ytterbium Metal

The work on ytterbium metal required the best possible vacuum conditions with typical pressures while running the electron gun of better than 10^{-9} Torr. The procedure for baking the vacuum system and outgassing the evaporator and electron gun have been described in Chapter three. The sample anode was cleaned before evaporation by electron bombarding the surface, the gun running at high voltage and current with the anode water cooling turned off. After cleaning, as soon as the pressure was less than 10^{-9} Torr, a sample was evaporated, the thickness of which was monitored by a crystal microbalance. For ytterbium metal, in which no self absorption was expected, a thick layer was always deposited. During evaporation, the pressure never exceeded 5×10^{-9} Torr. A spectrum recorded using one of the multi-scanning routines is presented in Fig 5:2. This spectrum has been analysed and filtered as described in section two of this chapter. This shows a peak at 1518.0 eV which is a good fit to a Lorentzian with superimposed high energy components giving shoulders at 1519.3eV and 1521.3eV. Between different spectra of the same region, the shape and intensity of the double shoulder changed and it was found that as the sample aged, the intensity of the high energy structure grew. The sample was deliberately oxidised by an admission of air into the chamber and it was found that the high energy structure became very much larger. A dip in the high energy structure at around 1520.0eV could be correlated with self absorption at the M_5 absorption line in ytterbium oxide.

(Karnatak, 1971).

It was concluded therefore that at least some of the high energy structure was due to emission and absorption in ytterbium oxide. The oxidation could not be eliminated by improving the vacuum and it was concluded that the oxidation rate was being enhanced by the electron beam. This effect has been observed for thulium (Curzon, 1972) at higher beam energies but the case for ytterbium has not been previously reported.

The rate at which the high energy structure grew as a function of time and beam current was investigated. From this study it was apparent that the data was only reliable for ten minutes after evaporation at an average beam current of 20mA. To achieve the necessary statistical accuracy it was therefore necessary to split the energy range into ten segments which were each measured after fresh evaporation. In each measurement, the peak output at 1918.0 eV was measured to a standard deviation of 0.5% so that the individual segments could be normalised. In this way the measurements in each segment could be normalised to other segments so that a total spectrum could be reconstructed. The M_{α} spectrum of ytterbium metal excited by 3.0 KV electrons recorded in this way is shown in Fig. 5:3. On the low energy side of the main peak at 1518.0eV, the data is very similar to that recorded from a single ytterbium film. Between energies of 1518.0eV and 1530.0eV there is a considerable change with a substantial part of the higher energy structure having diminished. In particular, the structure around 1520 eV identified as self absorption in ytterbium oxide has largely been eliminated. This spectrum was remeasured many times and within statistical limits all the spectra were identical. The remaining high energy structure could therefore be attributed to satellites and not contamination. The main feature at 1518.0eV could be fitted with a Lorentzian curve of full width at half maximum of 2.8 eV

which gave an error between 1512.0eV and 1518.0eV within statistical limits. Due to poor count rate the spectrum could not be recorded at a lower excitation energy.

5:3:2 The M_{α} Emission Spectra of Ytterbium in Ytterbium Flouride

Due to the incomplete 4f shell in ytterbium flouride, self absorption can occur and so the deconvolution procedure outlined in section one of this chapter was followed. The M_{α} region of this material has previously been measured (Parrott, 1965) but although thin target layers were used some residual self absorption remained in the spectra. The m_{β} region does not suffer from self absorption as the corresponding M_{β} absorption transition is forbidden by selection rules. The M_{γ} absorption in ytterbium oxide has been previously measured (Combley, 1963; Karnatak, 1971), the spectrum being shown to consist of a single symmetrical line centered on 1520.0 eV. Fig. 5:4 shows the peak of the m_{α} region recorded with a thin target ($10 \mu\text{g}/\text{cm}^2$) but under conditions of slight self absorption. The dip at 1519.8eV was due to self absorption and can be correlated with the previous measurements of the M_{γ} absorption. The m_{α} region of ytterbium in ytterbium flouride recorded at 3.0 KV and 2.0 KV excitation energy corrected for self absorption are shown in Figs. 5:5 and 5:6 respectively. These show that the self absorption component has disappeared and that the position of the two peaks at 1520.6 eV and 1522.8 eV are independent of excitation energy although strongly modulated in intensity. The highly asymmetric double peak at 3.0 KV excitation energy suggests that an unresolved component exists between the two peaks at approximately 1521.8 eV. Several other unresolved features can be seen on the high energy tail but their energy positions cannot be accurately determined. An attempt was made to resolve the spectra into lorentzian components but this was unsuccessful due to the

components being too overlapped. The minimisation procedure adopted gave many possible solutions to the number, intensity, width and position of the various components each of which was as probable as another. In this type of minimisation procedure many local minima can occur, the true solution being represented by the deepest minima. The quality of the solution can be assessed by a comparison of the size of the true minimum in parameter space to the average size of other minima. In this case the minima were all approximately equal and so the problem was insoluble. Parrott (1965) has obtained a solution to the overlapping components using a least squares minimisation method, but this only represents one minima. Once a local minima has been found, the program must restart at a different place in parameter space and then further minima may be found.

The overall trend on lowering the excitation voltage was to reduce the high energy components above the main line at 1520.6 eV. A further unresolved component appeared at 1517 eV on lowering the voltage to 2.0 KV.

The m_{β} region of ytterbium in ytterbium fluoride recorded at 3.0 KV and 2.0 KV excitation energy is shown in Fig. 5:7 and 5:8 respectively. The main feature is an asymmetric peak at 1567.7 with a high energy tail consisting of unresolved overlapping components. On reduction of the excitation voltage to 2.0 KV the intensity of the integrated high energy components drops with respect to the main peak and some new unresolved components appear.

In both the m_{α} and m_{β} spectra the general trend is that on reduction of the excitation voltage, the intensity of the components on the high energy side of the main line decreases. The number, position and shape of the high energy components could not be assessed due to them being too highly overlapped but individual components appear to modulate differently as a

function of excitation energy.

5:3:3 The $m_{\alpha, \beta}$ Emission Spectra of Lutetium in Lutetium Fluoride

The m_{α} region of lutetium in lutetium fluoride recorded at an excitation voltage of 3.0 KV and 2.0 KV is shown in Fig. 5:9 and 5:10 respectively. As previously described in this chapter the spectra shown are unfiltered, the vertical error bars representing the standard deviation of a set of measurements for each point. Similarly to ytterbium metal, lutetium fluoride has a full 4f shell and so $m_{4,5}$ self absorption could not take place. The main peak at 1581.3 eV is well fitted by a Lorentzian line of full width at half maximum of 2.5 eV. The fit to the low energy tail of the spectrum is good with a small departure between 1572 eV and 1578 eV where some small structures are observable. On the high energy side of this profile some complex overlapping structures can be seen. On reduction of the excitation voltage to 2.0 KV, the peak has become asymmetric with the main feature at 1581.8 and the asymmetry towards slightly lower energy. A comparison between the 3.0 KV and 2.0 KV cases shows that the low energy tails are identical apart from near the asymmetric peak and that the high energy structure decreases on reducing the excitation voltage. A Lorentzian fit to the low energy profile of the 2.0 KV excited spectrum gives a full width at half maximum and a peak position identical to the 3.0 KV case. The apparent peak shift is therefore probably due to a sharp unresolved component at 1581.8 eV which decays less rapidly than the feature at 1518.3 eV on reducing the excitation voltage.

The m_{β} region of lutetium in lutetium fluoride recorded at an excitation voltage of 3.0 KV and 2.0 KV is shown in Fig. 5:11 and 5:12 respectively. The structure is asymmetric with a main peak at 1631.1 for 3.0 KV excitation moving to 1631.2 eV for 2.0 KV excitation. The low energy tail in both

cases has some small unresolved components below 1530 eV. On reduction of the excitation voltage to 2.0 KV, the high energy structure decreases with respect to the main feature which becomes more symmetrical. The best fit lorentzian to the low energy tail of the 2.0 KV curve gave a full width at half maximum of 2.2 eV.

5:3:4 The $m_{\alpha,\beta}$ Emission Spectra of Thulium Metal

The $m_{\alpha,\beta}$ spectra of thulium metal were recorded using the multiple evaporation technique used for ytterbium metal. As in the case of ytterbium, spectra were collected only for 3.0 KV excitation. Due to the incomplete 4f shell similar techniques were used as in the case of ytterbium flouride to eliminate self absorption features. The m_{α} spectrum of thulium metal recorded at 3.0 KV excitation energy is shown in Fig. 5:13. The spectrum is made up of a main peak at 1462.1 eV with weak unresolved components at 1458 and 1464 eV. An unconstrained fitting of the spectrum with lorentzian peaks at these three energies revealed that above 1467 eV a large residual structure existed.

The m_{β} spectrum of thulium metal recorded at 3.0 KV excitation energy is shown in Fig 5:14. This shows a main feature at 1502.5 eV, the low energy tail of which can be well fitted with a lorentzian curve of full width at half maximum of 3.6 eV. An unresolved feature at 1504.4 eV can be seen and again if an unconstrained lorentzian fitting is carried out for the two principle peaks then a large residual structure can be identified above 1508 eV.

5:3:5 The $m_{\alpha,\beta}$ Emission Spectra of Thulium in Thulium Flouride

The $m_{\alpha,\beta}$ spectra of thulium in thulium flouride recorded at 3.0 KV corrected for self absorption are shown in Fig. 5:15 and 5:16. The m_{α} region appears to be very similar to that in the metal with a small shift from 1462.1 eV to 1462.3 eV

for the main peak. A small feature 1.8 eV above the main peak has appeared but the overall full width at half maximum of the structure has remained approximately constant at 8.5 eV. The $m\beta$ spectrum recorded at 3.0 KV excitation energy is again very similar to the metallic spectrum with slightly more emission on the high energy side of the main feature, but with a very similar overall full width at half maximum of approximately 6.0 eV.

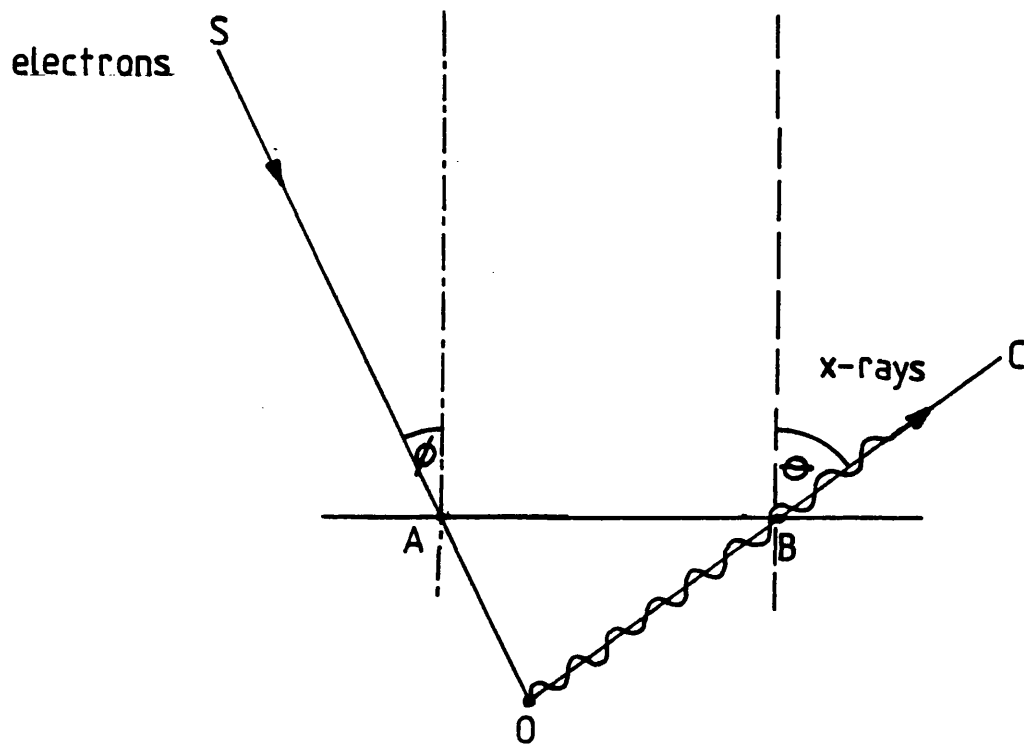
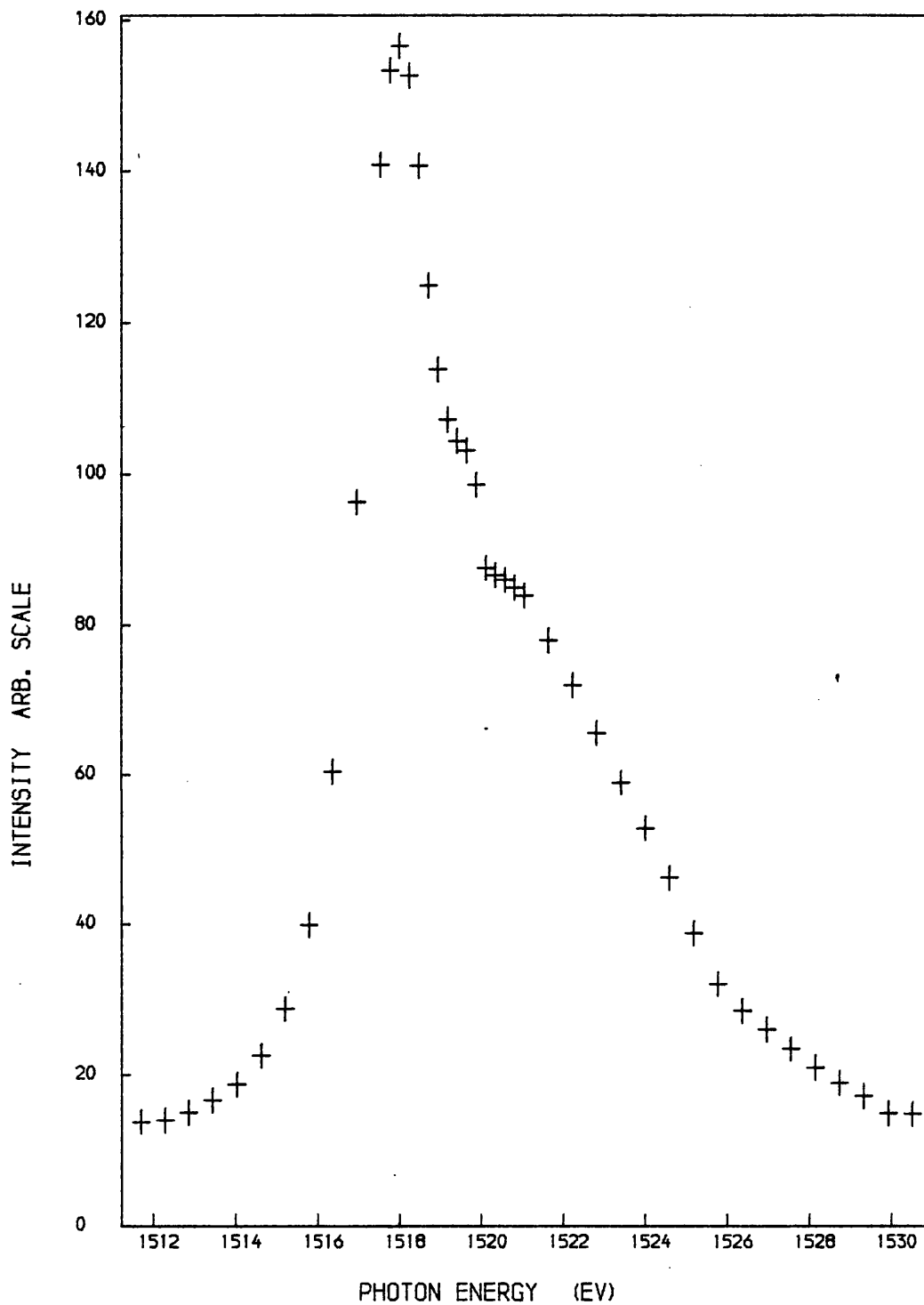


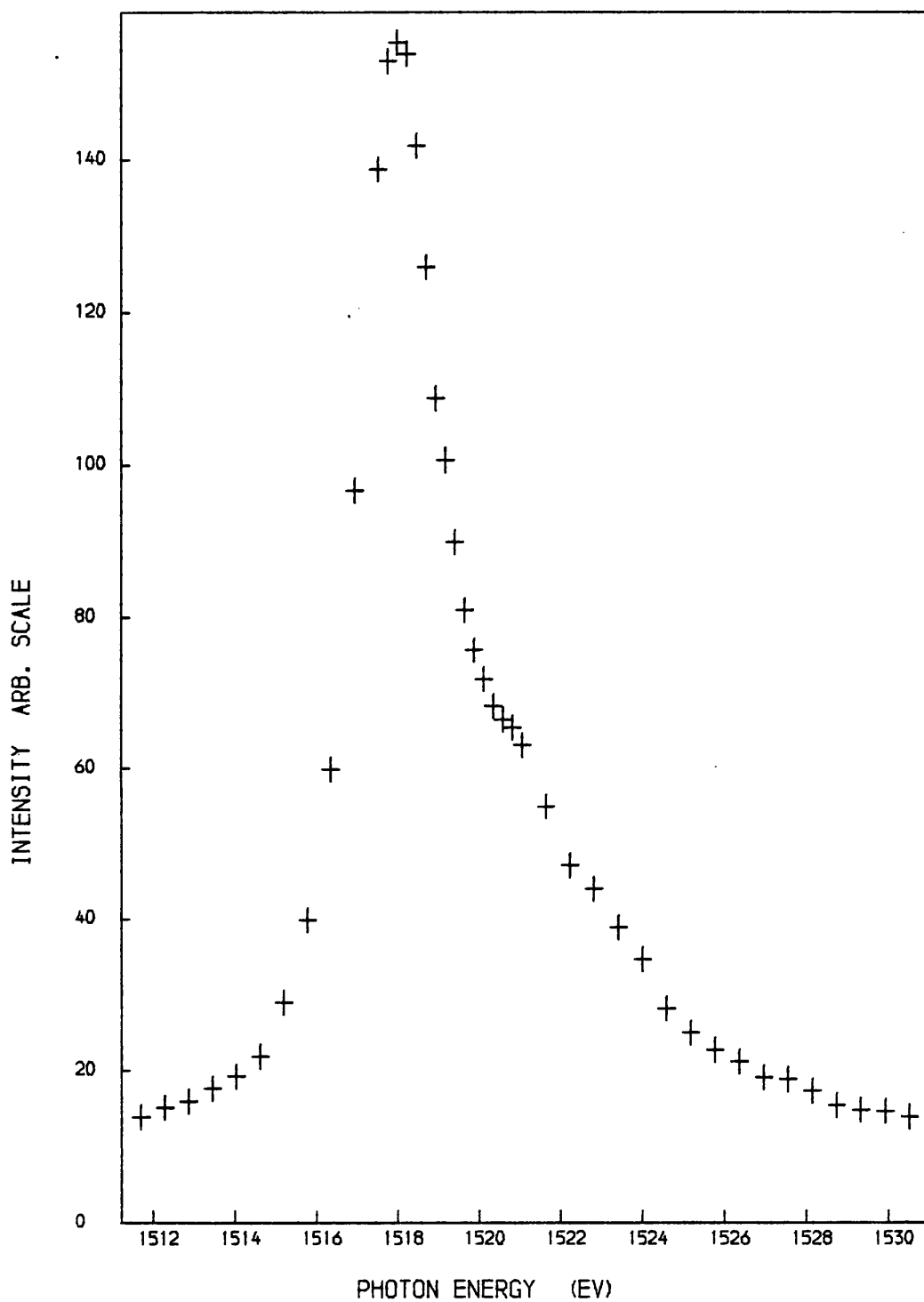
FIG 5:1 SELF ABSORPTION GEOMETRY.



M ALPHA REGION OF YTTERBIUM METAL.

EXCITING VOLTAGE 3.0 K.V. , MAX. STANDARD DEVIATION 2%.
FRESH YTTERBIUM FILM.

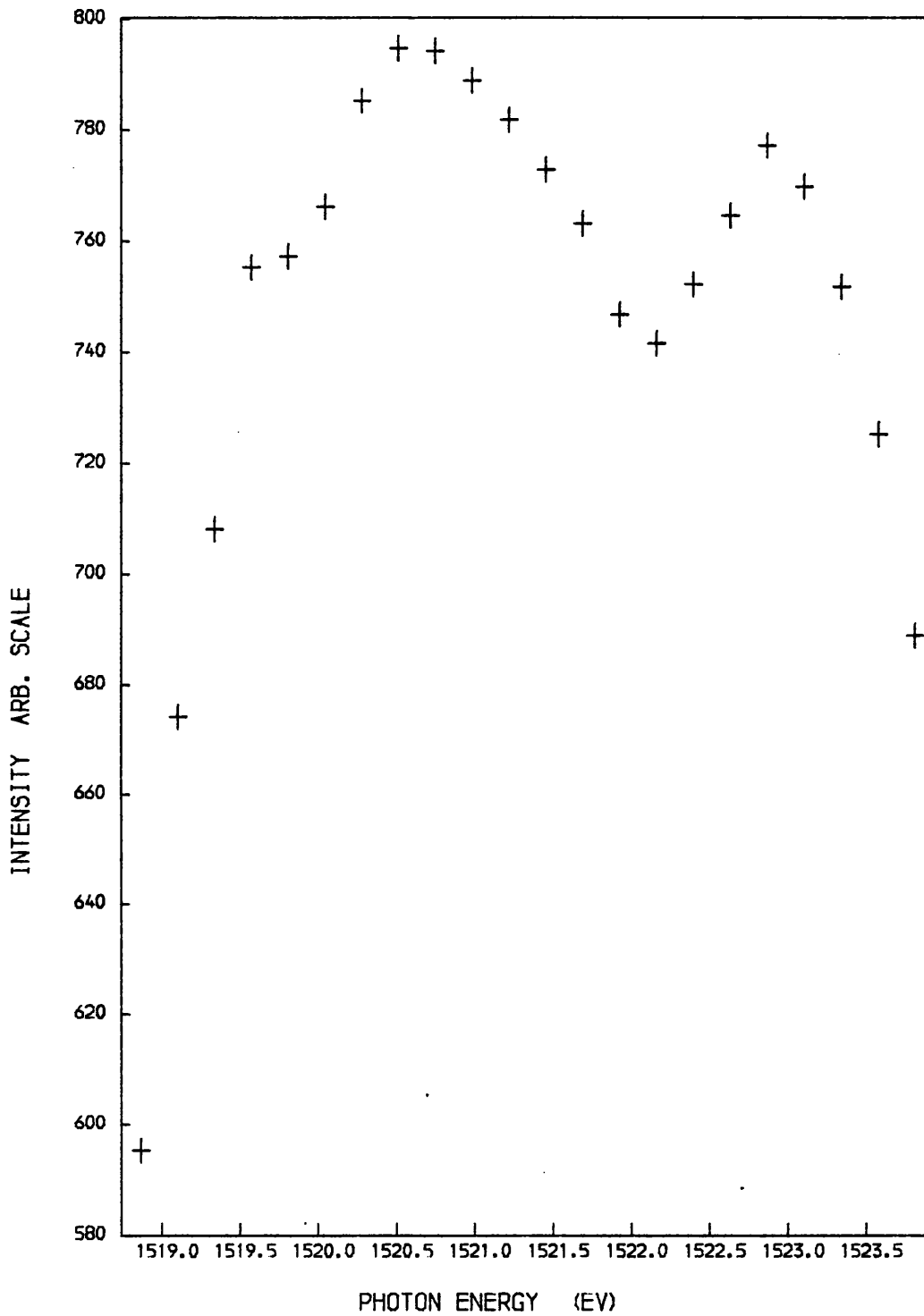
FIG 5:2



M ALPHA REGION OF YTTERBIUM METAL.

EXCITING VOLTAGE 3.0 K.V. , MAX. STANDARD DEVIATION 2%.
 RECONSTRUCTED SPECTRUM USING MULTIPLE EVAPORATION TECHNIQUE.

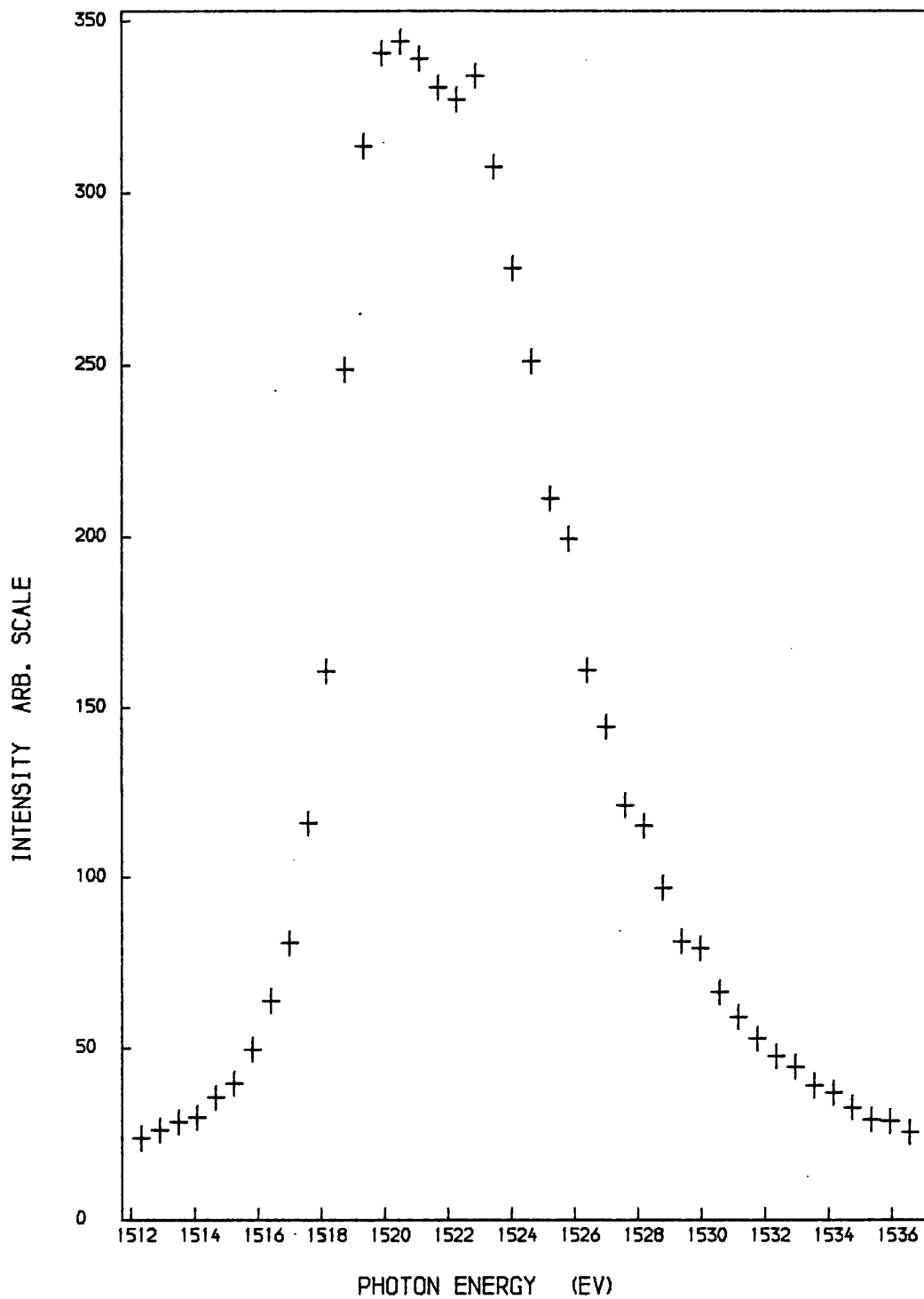
FIG 5:3



M ALPHA REGION OF YTTERBIUM IN YTTERBIUM FLUORIDE.

EXCITING VOLTAGE 3.0 K.V. , MAX. STANDARD DEVIATION 1%.
30 DEGREE INCIDENT ELECTRON ANGLE , 30 DEGREE TAKEOFF ANGLE.

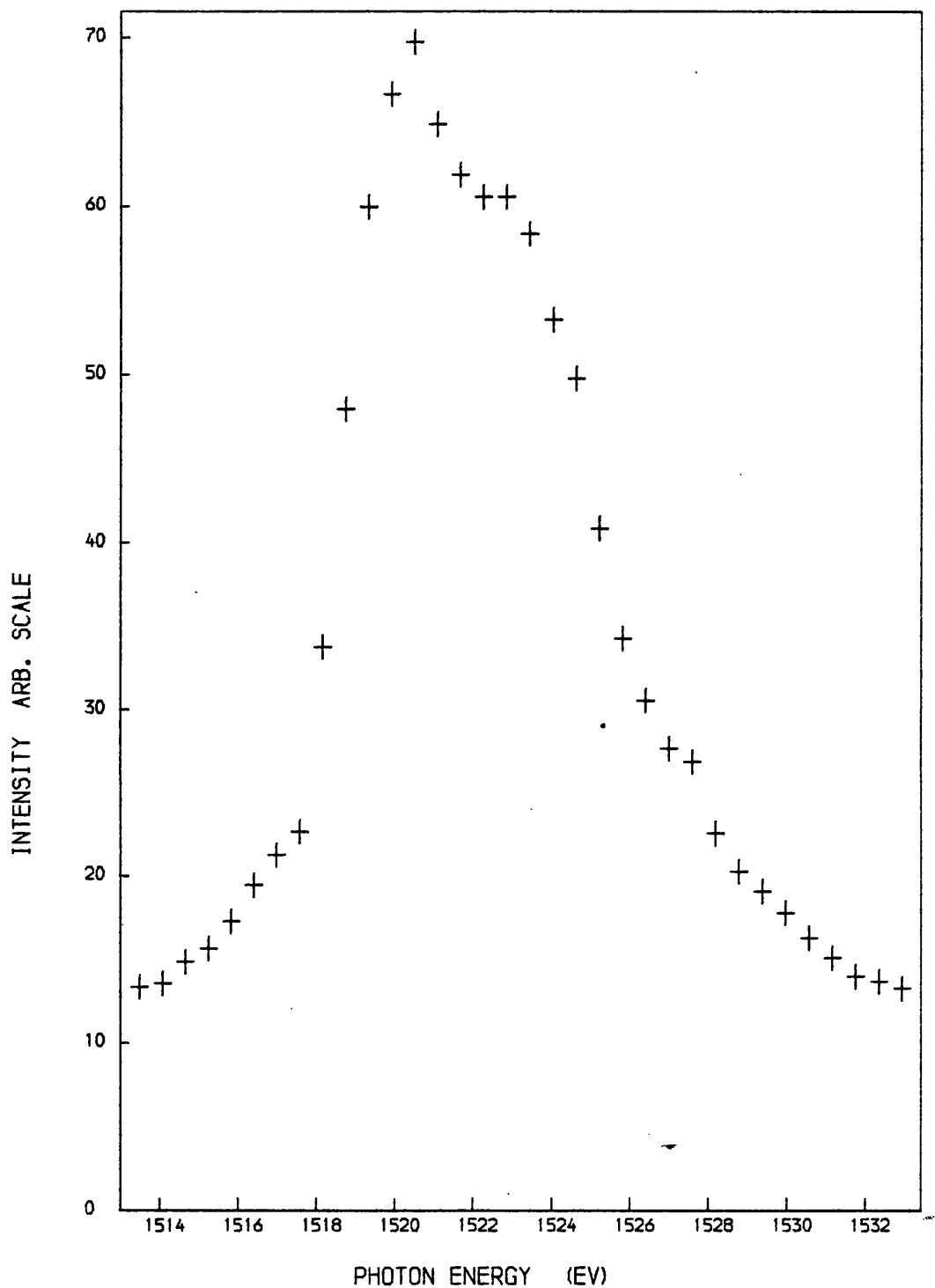
FIG 5:4



M ALPHA REGION OF YTTERBIUM IN YTTERBIUM FLUORIDE.

EXCITING VOLTAGE 3.0 K.V. , MAX. STANDARD DEVIATION 1%.
SPECTRUM CORRECTED FOR SELF ABSORPTION.

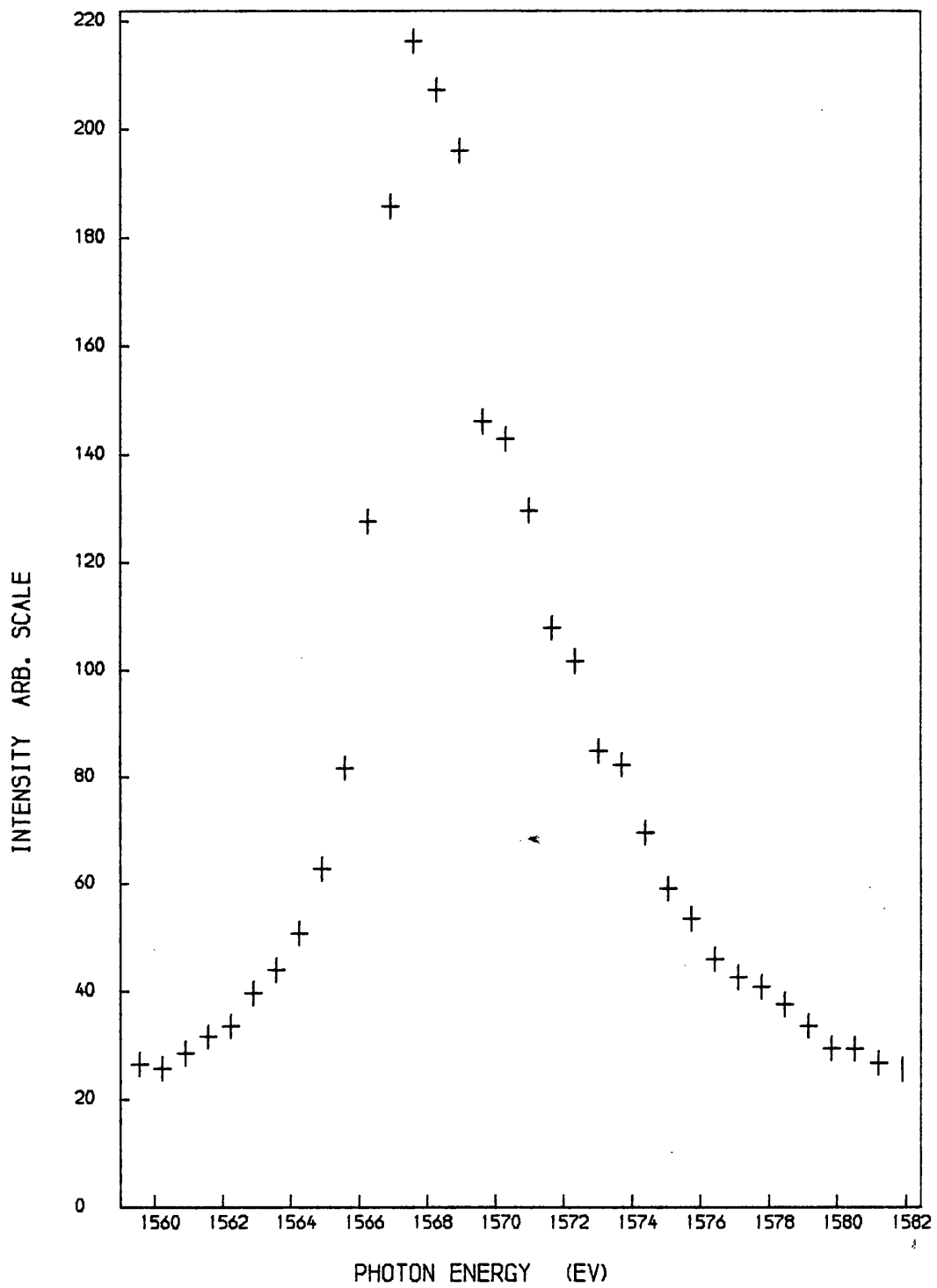
FIG 5:5



M ALPHA REGION OF YTTERBIUM IN YTTERBIUM FLUORIDE.

EXCITING VOLTAGE 2.0 K.V. , MAX. STANDARD DEVIATION 1%.
SPECTRUM CORRECTED FOR SELF ABSORPTION.

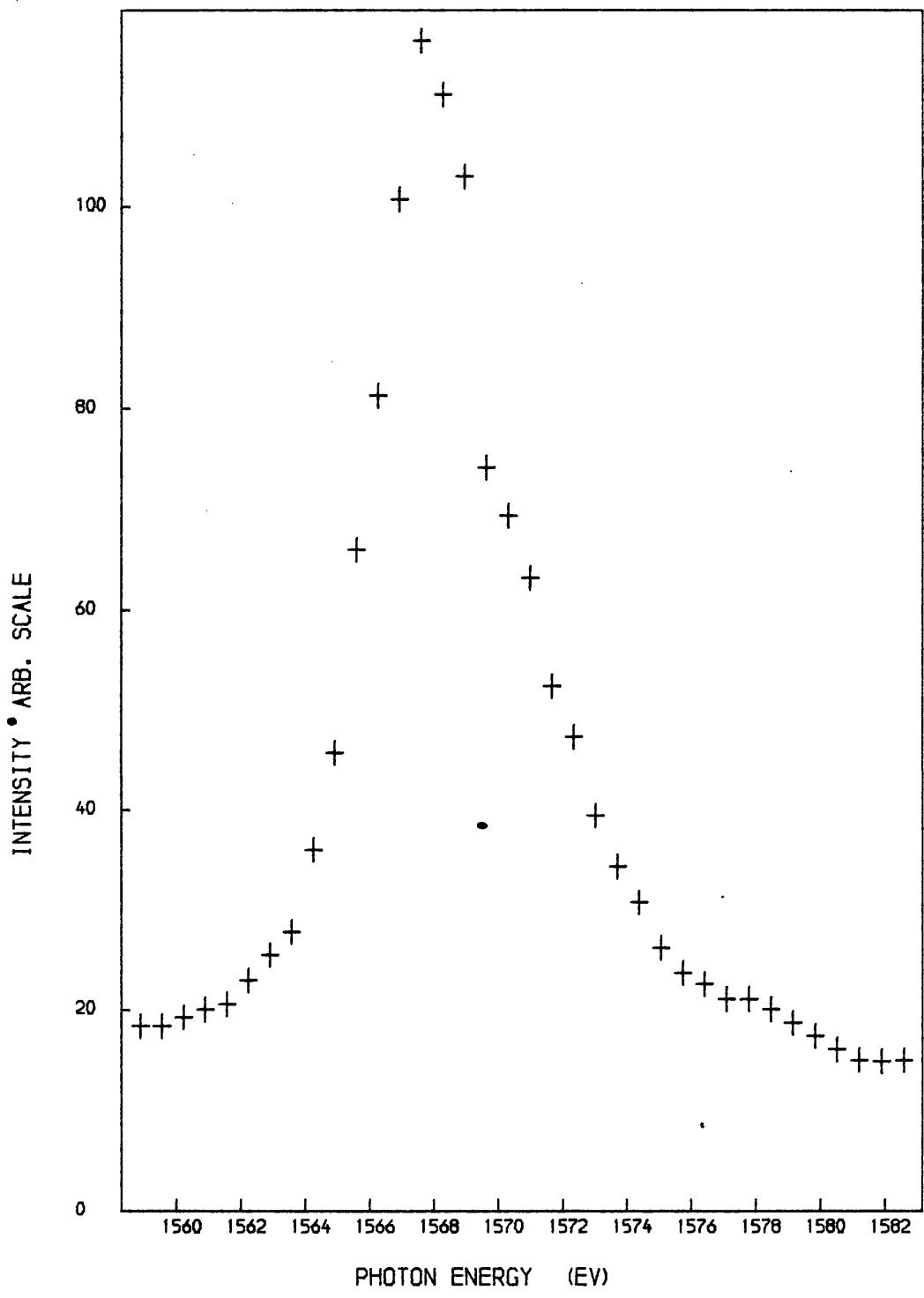
FIG 5:6



M BETA REGION OF YTTERBIUM IN YTTERBIUM FLUORIDE.

EXCITING VOLTAGE 3.0 K.V. , MAX. STANDARD DEVIATION 1%.

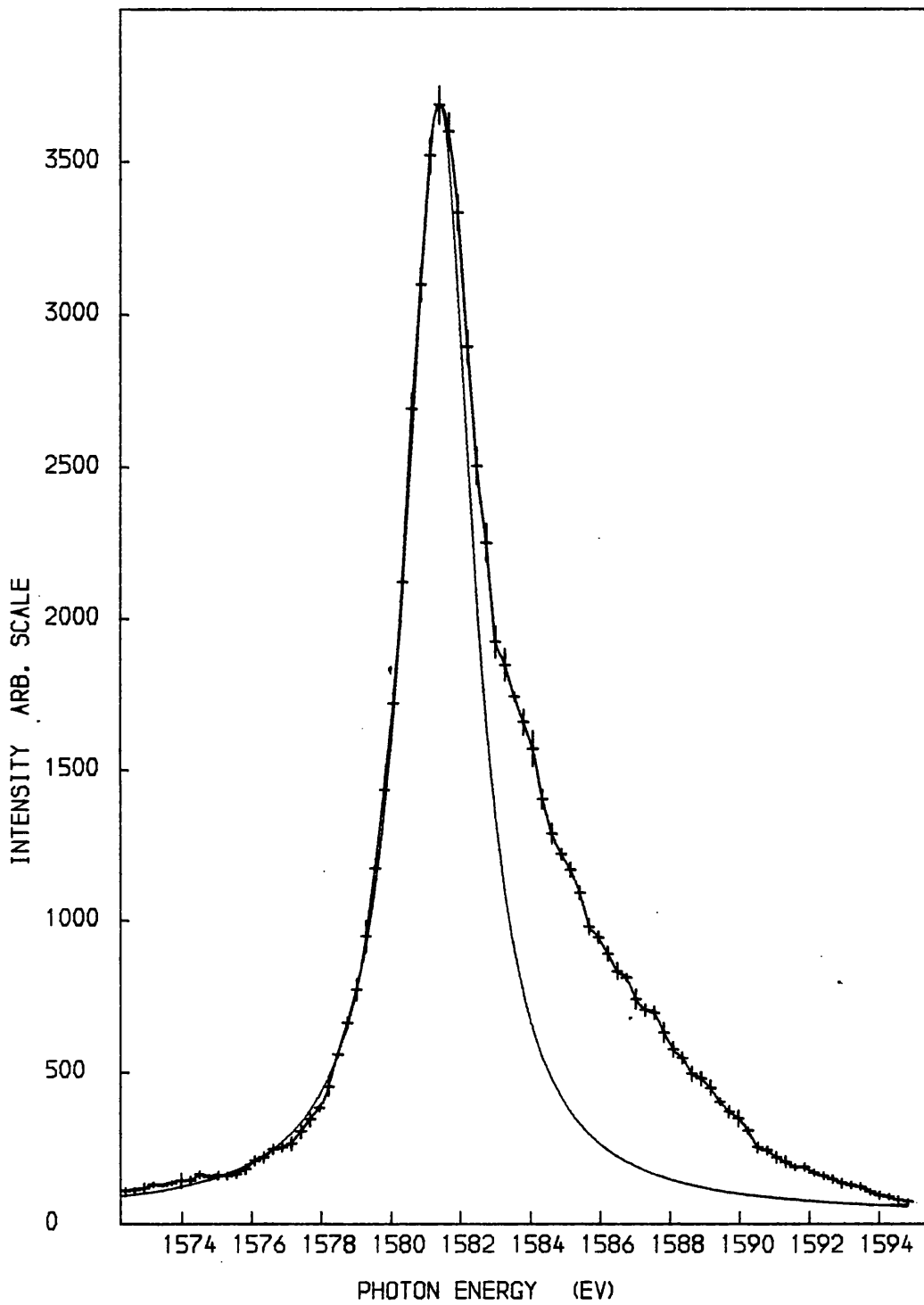
FIG 5:7



M BETA REGION OF YTTERBIUM IN YTTERBIUM FLUORIDE.

EXCITING VOLTAGE 2.0 K.V. , MAX. STANDARD DEVIATION 1%.

FIG 5:8

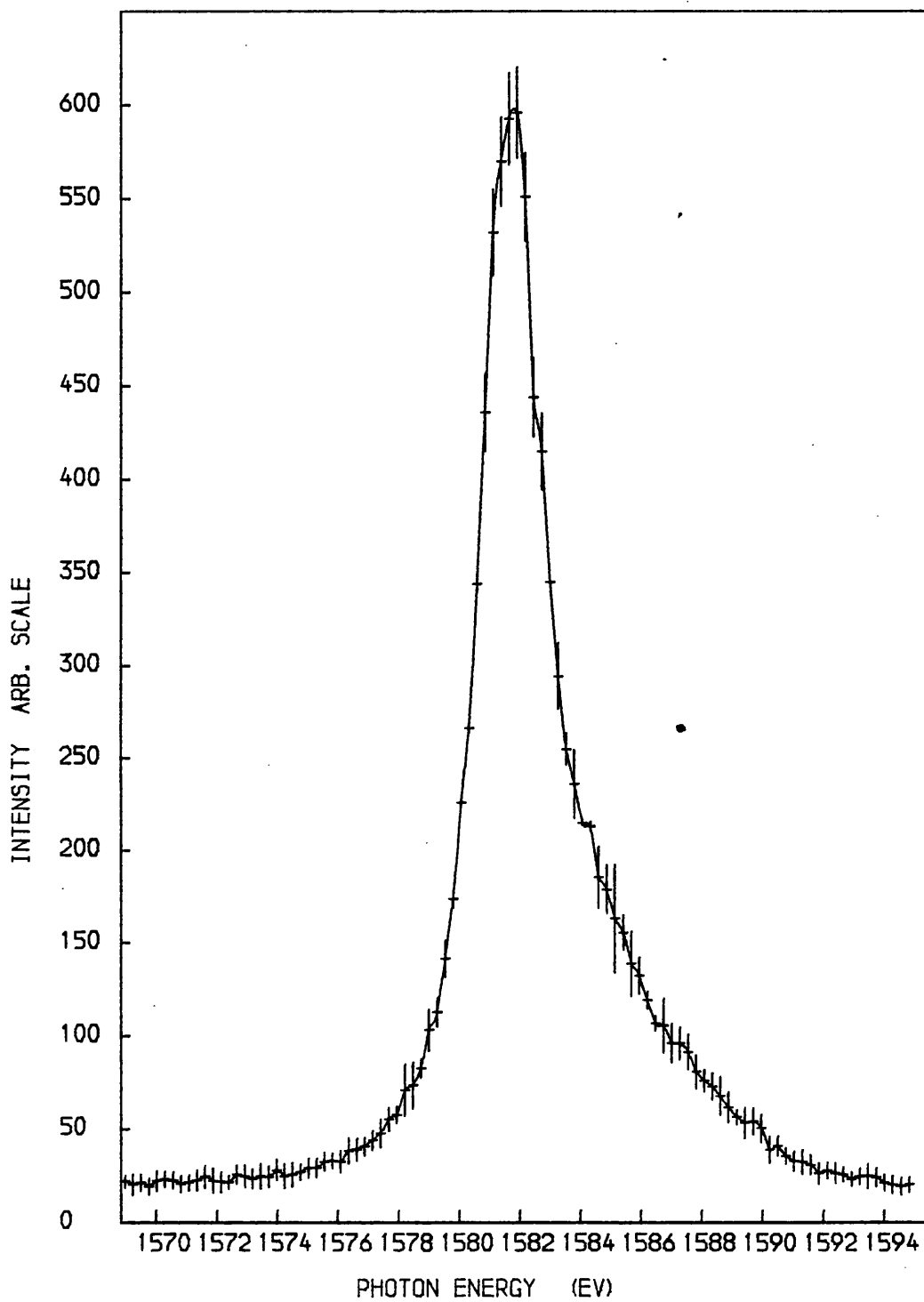


M ALPHA REGION OF LUTETIUM IN LUTETIUM FLUORIDE.

EXCITING VOLTAGE 3.0 K.V.

LORENTZIAN FIT TO MAIN PEAK.

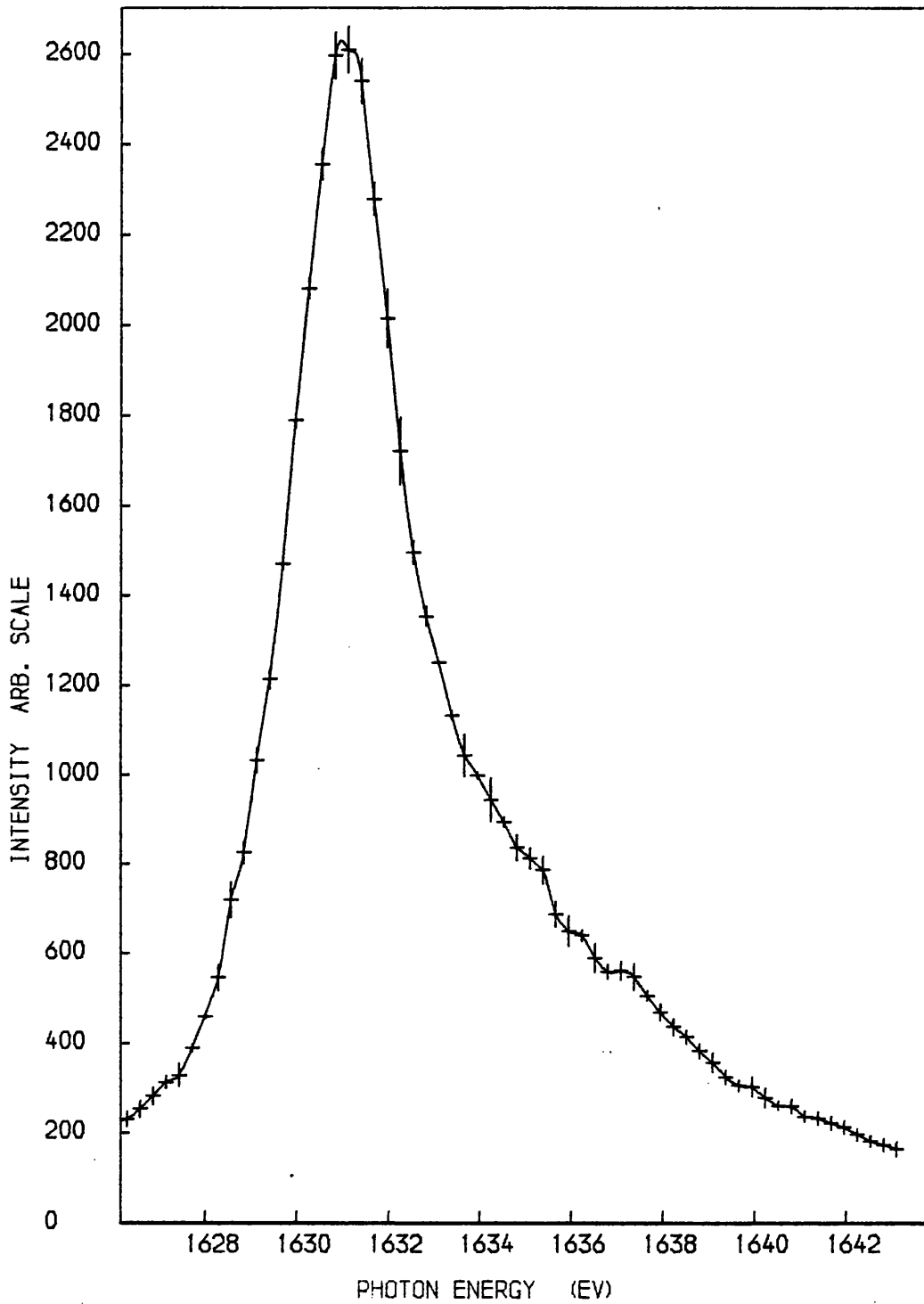
FIG 5:9



M ALPHA REGION OF LUTETIUM IN LUTETIUM FLUORIDE.

EXCITING VOLTAGE 2.0 K.V.

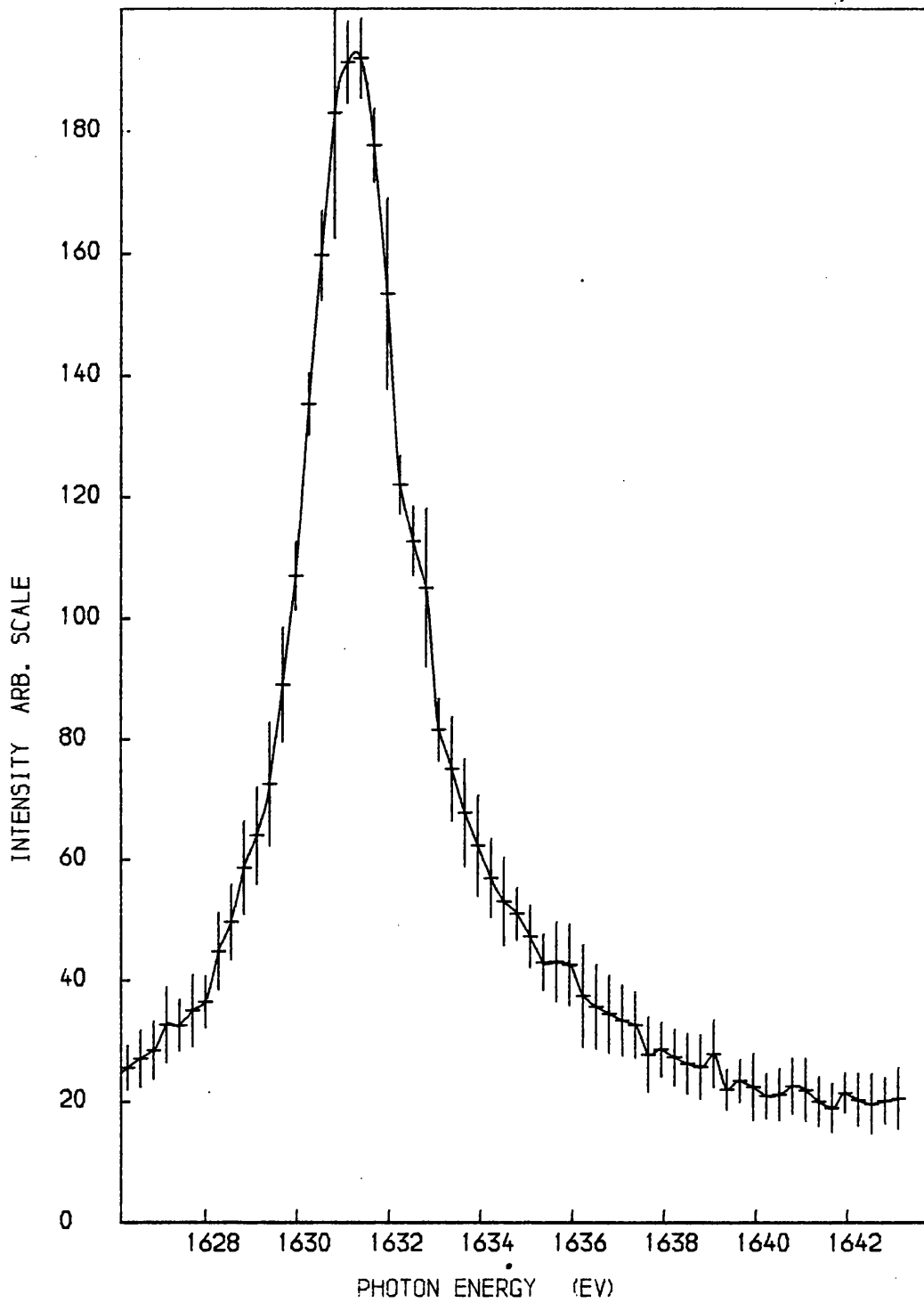
FIG 5:10



M BETA REGION OF LUTETIUM IN LUTETIUM FLUORIDE.

EXCITING VOLTAGE 3.0 K.V.

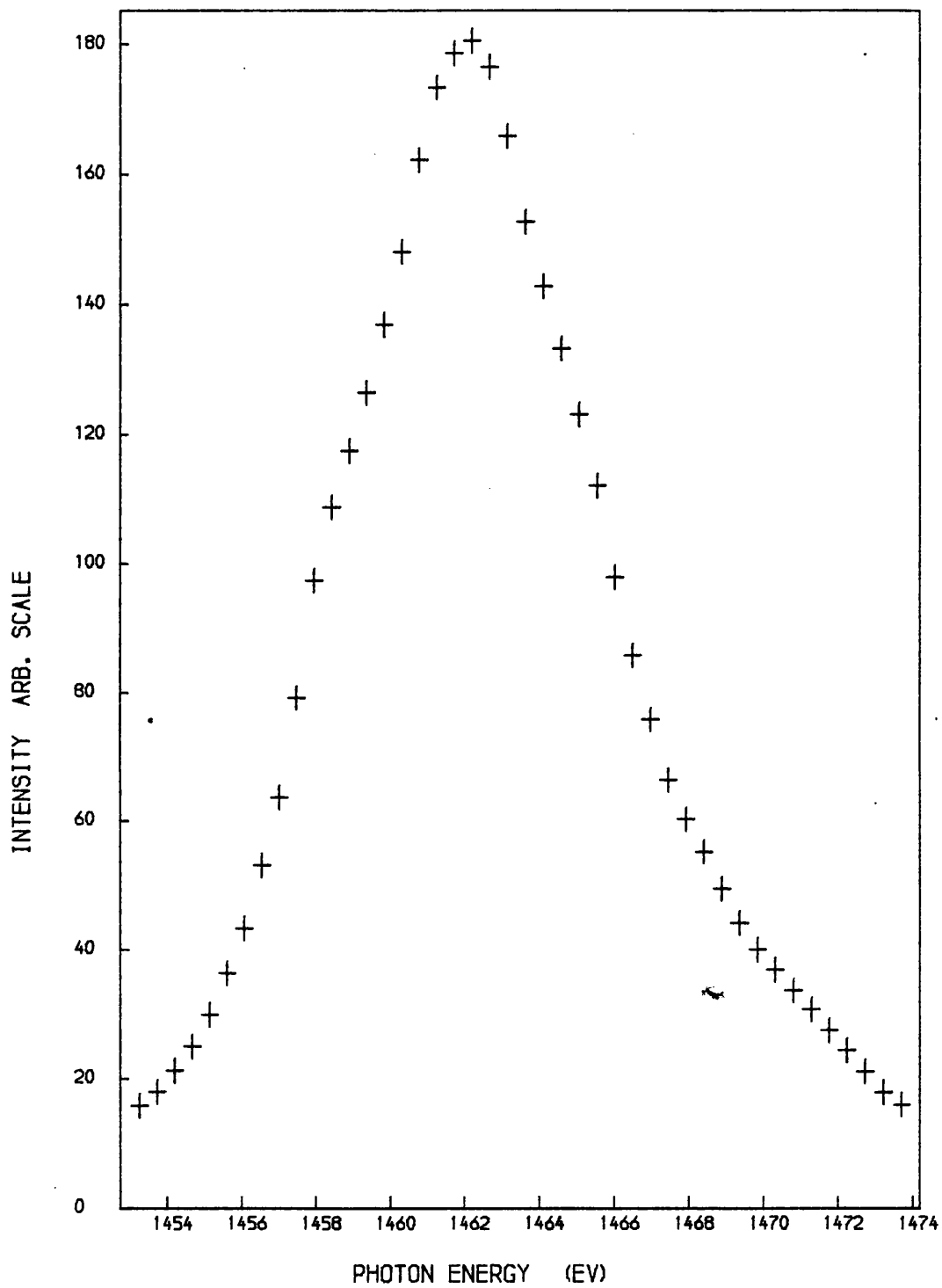
FIG 5:11



M BETA REGION OF LUTETIUM IN LUTETIUM FLUORIDE.

EXCITING VOLTAGE 2.0 K.V.

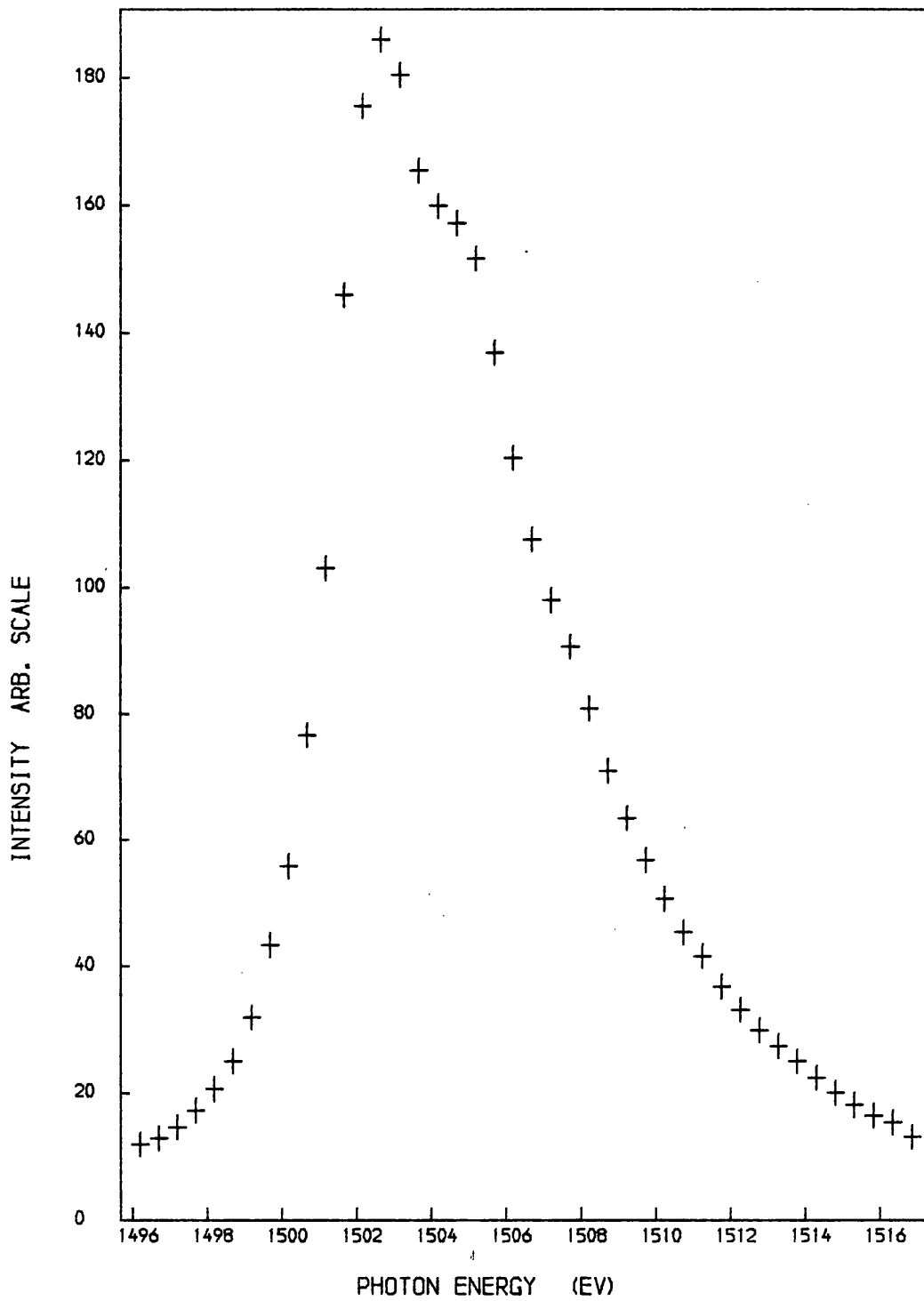
FIG 5:12



M ALPHA REGION OF THULIUM METAL.

EXCITING VOLTAGE 3.0 K.V. , MAX. STANDARD DEVIATION 2%.
RECONSTRUCTED SPECTRUM USING MULTIPLE EVAPORATION TECHNIQUE.

FIG 5:13

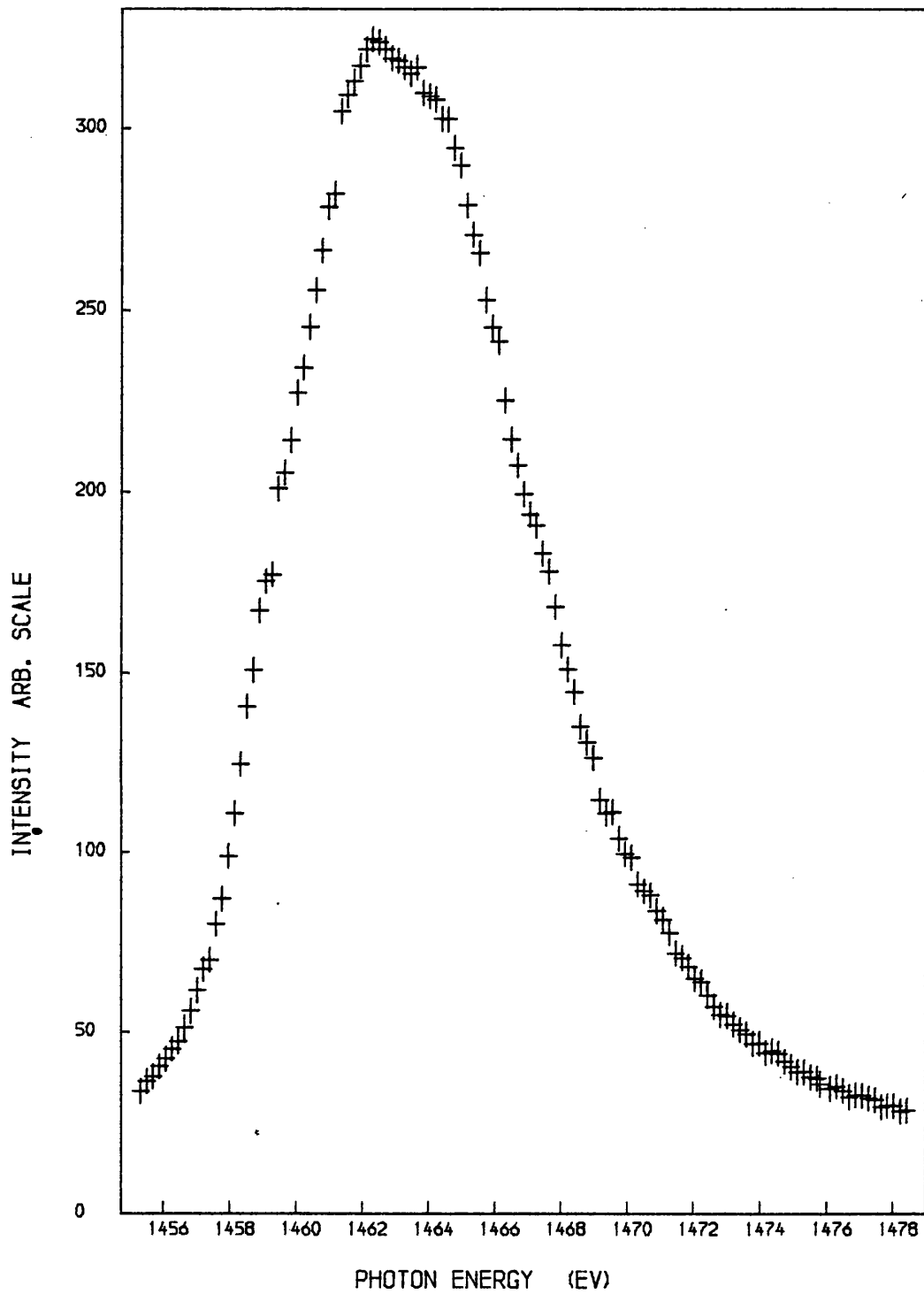


M BETA REGION OF THULIUM METAL.

EXCITING VOLTAGE 3.0 K.V. , MAX. STANDARD DEVIATION 2%.

RECONSTRUCTED SPECTRUM USING MULTIPLE EVAPORATION TECHNIQUE.

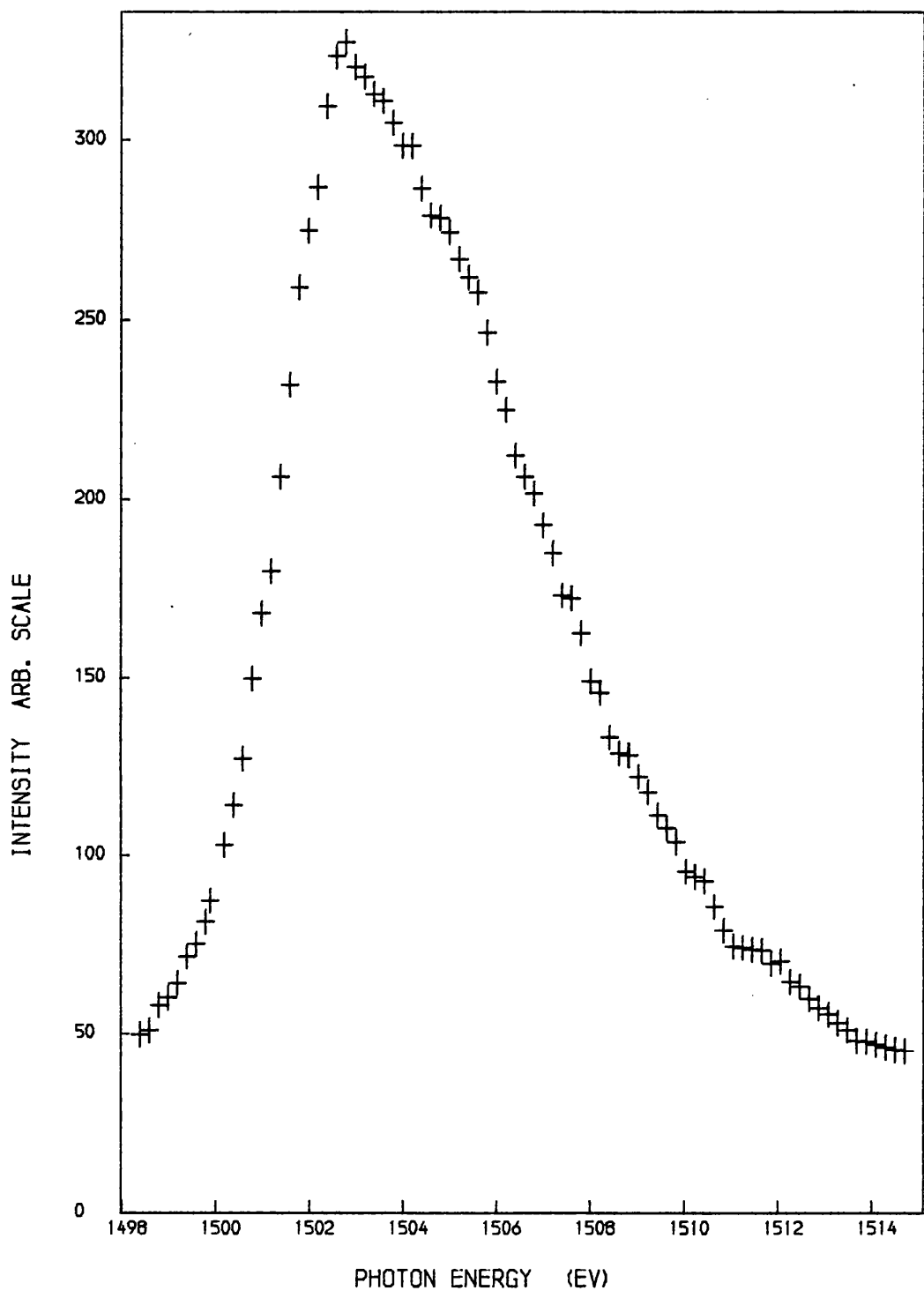
FIG 5:14



M ALPHA REGION OF THULIUM IN THULIUM FLUORIDE.

EXCITING VOLTAGE 3.0 K.V. , MAX. STANDARD DEVIATION 2%.
SPECTRUM CORRECTED FOR SELF ABSORPTION.

FIG 5:15



M BETA REGION OF THULIUM IN THULIUM FLUORIDE.

EXCITING VOLTAGE 3.0 K.V. , MAX. STANDARD DEVIATION 2%.
SPECTRUM CORRECTED FOR SELF ABSORPTION.

FIG 5:16

CHAPTER 6

DISCUSSION AND CONCLUSION

Page No.

Introduction	103.
6:1 Resonance emission in lanthanum.	107.
6:2 Competing processes in the spectra of the heavy rare earths.	109.
6:3 The $m_{\alpha, \beta}$ region of lutetium fluoride	111.
6:4 The m_{α} region of ytterbium metal.	114.
6:5 The $m_{\alpha, \beta}$ region of ytterbium fluoride	117.
6:6 The $m_{\alpha, \beta}$ region of thulium metal and fluoride.	122.
6:7 Experimental Refinements	125.
6:8 Conclusions	127.

CHAPTER 6DISCUSSION AND CONCLUSIONIntroduction

The purpose of this chapter is to discuss the data presented in Chapter 5 in the light of the resonance and ionisation transition model described in Chapter 2. The heavy rare earths thulium, ytterbium and lutetium were chosen for the study as they represent the simplest heavy rare earths as far as $4f - 3d$ transitions are concerned. The case of ytterbium is particularly important due to the change of valence from two to three on oxidation as observed by Combley, Stewardson and Wilson (1968). The change in valency causes the $4f$ occupation to drop from $4f^{14}$ to $4f^{13}$ which allows an alternative decay path to the normal ionisation channel. The number of allowed transitions for elements between cerium and thulium means that the $m_{\alpha, \beta}$ structures will consist of very heavily overlapped lines which will be unresolved making identification impossible. The $3d$ photo-absorption in the lanthanides is now well understood on an atomic model due to Sugar (1972) and was originally applied to lanthanum. This model has been extended to include most of the lanthanides (Bonnelle, Karnatak and Sugar, 1974; Bonnelle, Karnatak and Spector, 1977; Belrhmi-Belhassan, Karnatak, Spector and Bonnelle, 1981; Karnatak, Esteva and Connerade, 1981) and recently due to the use of the very high x-ray fluxes available from an electron synchrotron, very high resolution spectra have been obtained. In this work by Karnatak, Esteva and Connerade (1981), a double crystal monochromator was used which achieved a resolution of less than 0.1 eV and allowed a detailed investigation of line-shapes. The high flux available allowed spectra to be taken

very quickly and so reduced the possibility of oxidation or contamination of the thin films. The rare earth metals are extremely reactive and have been very difficult to study by x-ray emission. Due to the high incident electron fluxes needed to generate a reasonable count rate even using focusing crystal optics, the water cooled target becomes hot and enhances the reactivity of the material under study. A partial solution to the problem was found in the present study by using short data collection cycles and multiple evaporations in conjunction with a very clean electron gun and good ultra-high vacuum conditions. The problems with the present apparatus used to collect $m_{\alpha, \beta}$ x-ray emission spectra are discussed later in this chapter together with possible solutions. Although a very large body of high resolution data now exists on 3d photoabsorption, the only published $m_{\alpha, \beta}$ emission data exists for lanthanum (Mariot and Karnatak, 1974A; Liefeld, Burr and Chamberlain, 1974) cerium (Chamberlain, Burr and Liefeld, 1974) and europium (Mariot and Karnatak, 1974B), although unpublished work exists for cerium, europium, gadolinium, dysprosium and ytterbium in metallic and oxide form (Karnatak, 1971) and for ytterbium in metallic and fluoride form and hafnium dioxide (Parrott, 1965). The work of Karnatak (1971) was conducted using photographic recording and also suffered from poor instrumental resolution. Further to this, the metallic targets were prepared in poor vacuum conditions and then coated with a thin layer of aluminium to prevent further oxidation. Very large differences exist between the spectra recorded by Karnatak and Parrott with the spectra recorded by Karnatak being very broad. As discussed in Chapter 2, a measure of the severe instrumental broadening can be gained by a comparison of the $Yb_2 O_3$ m_5 absorption by Karnatak to the measurement by

Combley, Stewardson and Wilson (1968). In the work of Parrott (1965), reproduceable results were not obtained for the ytterbium metal m_{α} due to oxidation of the sample after vacuum evaporation. The work on europium by Mariot and Karnatak (1974) indicates an instrumental broadening of approximately 1.0eV, a similar aluminium sandwich being used to prevent oxidation of the metal as in the earlier work by Karnatak. Measurements of the m_{α} and m_{β} spectra of lanthanum metal were also conducted by Mariot and Karnatak (1974) using the same technique and apparatus as used for the europium measurements. Measurement of the $m_{\alpha,\beta}$ spectra of lanthanum were also made by Liefeld, Burr and Chamberlain (1974) but only in the low excitation voltage region from just below the m_{γ} threshold to 15.0eV above the m_{α} threshold, a region approximately 35.0eV wide. Similar experiments were also conducted by Chamberlain, Burr and Liefeld (1974) for the $m_{\alpha,\beta}$ spectra of cerium again for excitation energies from just below the m_{γ} threshold to just above the m_{α} threshold. Resonances in the m_{α} and m_{β} structures were seen when the excitation voltage was within a few volts of the m_{γ} and m_{α} thresholds respectively. The structures were interpreted as being due to incident electrons being scattered into available 4f valence levels with the conversion of electron kinetic energy into single photon energy. The resonant behaviour of the structures close to threshold was ascribed to resonances in the cross section for scattering incident electrons into the vacant 4f levels. The resonances were described in terms of the creation of a two electron bound state involving an m_{γ} or m_{α} vacancy, the corresponding excited 3d electron and the incident electron being in bound orbitals around the vacancy produced in the 3d shell. These states then radiatively decay with one

electron returning to the 3d vacancy and the other going to a 4f orbital above the fermi level. Although the present work was conducted at a minimum of 300V above threshold and in the case of the work of Mariot and Karnatak (1974) at 700V above the m_4 threshold, the effects of resonant scattering can still be seen in the $m_{\alpha,\beta}$ spectra due to some electrons being inelastically scattered in the solid to the resonance energy. The unidentified low energy shouldering on the $m_{\alpha,\beta}$ spectra of lanthanum recorded by Mariot and Karnatak (1974) could be due to these processes and indeed the highest excitation voltage spectra of Liefeld, Burr and Chamberlain (1974) show a distinct low energy tail which was assigned to the resonant process occurring with incident electrons inelastically scattered to energies near the m_5 or m_4 thresholds.

The information concerning the $m_{\alpha,\beta}$ spectra of the rare earths is therefore very limited due to the technical difficulties in recording accurate data and the very much more complicated structures that result in emission than in absorption. The only theoretical treatment of $m_{\alpha,\beta}$ x-ray emission has been for lanthanum metal which in several ways is a special case and not applicable to the interpretation of the heavy rare earth spectra. In the work of Mariot and Karnatak (1974) on the $m_{\alpha,\beta}$ spectra of europium, comparisons were drawn between the spectra for Eu, EuS, EuO and Eu_2O_3 but interpretation of the structures was not attempted as the spectra were expected to contain several hundred overlapping components. The purpose of the present study was to look at the $m_{\alpha,\beta}$ spectra of a group of several heavy rare earths in which the 4f occupancy varied from $4f^{12}$ to $4f^{14}$ so that an explanation of the gross spectral features could be found. The case of ytterbium was of particular interest as it exhibits divalency in the metal

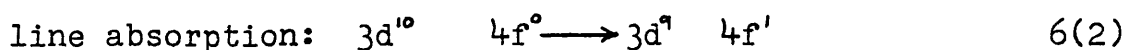
and trivalency in the compound form with a consequential reduction in the 4f occupation from $4f^{14}$ to $4f^{13}$ respectively. This contrasts with the normal trivalency of thulium and lutetium in metallic and compound form. The spectra of lanthanum and ytterbium in the metallic form are the simplest cases and on the basis of the model described in Chapter 2 should exhibit different types of transitions which occur together in cases where there are between one and thirteen electrons in the 4f shell.

6:1 Resonance emission in lanthanum.

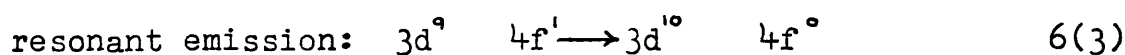
The normally designated $m_{\alpha,\beta}$ emission process involves the ionisation of a 3d electron. For lanthanum this would give,



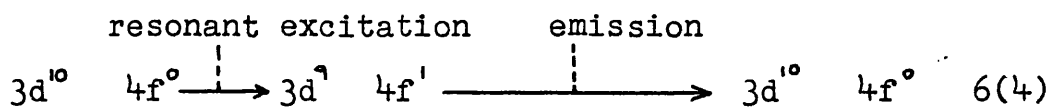
The measurements of the $m_{4,5}$ absorption spectrum of lanthanum by Ottewell (1969) show a doublet structure for m_5 and a single line for m_4 as discussed in Chapter 2. The lower energy component of the doublet is very weak and not clearly seen in the data of Mariot and Karnatak (1974) but is more clearly seen in the results presented by Bonnelle, Karnatak and Sugar 1974. The absorption line structure is therefore understood in terms of the transition,



The observation by Mariot and Karnatak (1974) of m_α and m_β structures in coincidence with the absorption features indicates that the initial state for emission must be the final state of the line absorption process.



The initial state is produced by a resonant promotion of a 3d electron to the 4f level by electron bombardment.



Because the 3d spin-orbit coupling is the predominant interaction, the m_4 and m_5 lines in absorption and emission are approximately separated by the separation of the $3d_{3/2}$ and $3d_{5/2}$ atomic levels. The areas under the m_4 and m_5 curves were found to be in good agreement with the calculations of Bonnelle, Karnatak and Sugar (1974). For lanthanum, the $3d_{3/2}$ (m_4) level is wider than the $3d_{5/2}$ (m_5) level due to the $3d_{3/2} 3d_{5/2} 4f$ Coster-Kronig transition which has a high transition probability. In the very high resolution work of Karnatak, Esteva and Connerade (1981) the m_5 width was measured to be 1.1eV and the m_4 width to be 1.8eV after deconvolution of the instrumental broadening. The width of the $3d_{5/2}$ level has been calculated by McGuire (1972) to be 0.73 eV, but the $3d^9 4f^1$ excited states should have a lifetime shorter than the $3d$ ion due to radiative and non radiative decay processes $3d^9 4f^1 \longrightarrow 3d^{10} 4f^0$ or $3d^9 4f^1 \longrightarrow 3d^{10} X^{-1}$. This would have the effect of increasing the value of 0.73eV by McGuire (1972) for the m_5 absorption line width. The lifetime of the $3d_{3/2}^9 4f^1$ excited state would also be reduced by $3d_{3/2} - 3d_{5/2} 4f$ Coster-Kronig transitions. This transition is obviously not open to a $3d_{5/2}^9 4f^1$ excited state and so the m_4 line width is less than the m_5 linewidth. Because the extra decay mode exists for $3d_{3/2}^9 4f^1$, the number of atoms available to radiatively decay from the excited state giving the m_5 resonance line is reduced. The m_5 line is therefore weakened in relation to m_4 when compared to the ratio of m_4 to m_5 absorption lines. The effective drop in intensity for m_5 due to Coster-Kronig decay from the $3d_{3/2}^9 4f^1$ excited state instead of radiative decay, is reflected in an

increase in width of the m_4 absorption line relative to m_5 .

These two effects compensate each other such that,

$$\frac{A(m_\alpha)}{A(m_\beta)} = \frac{H(m_\beta) \cdot W(m_4)}{H(m_4) \cdot W(m_\beta)} \quad 6(5)$$

where $A(m_\alpha)$ is the area under the m_α emission resonance line,

$A(m_\beta)$ is the area under the m_β emission resonance line,

$H(m_5)$ is the amplitude of the m_5 line absorption,

$H(m_4)$ is the amplitude of the m_4 line absorption,

$W(m_5)$ is the full width at half maximum of m_5 ,

$W(m_4)$ is the full width at half maximum of m_4 .

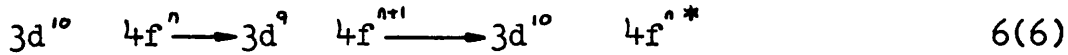
This has been experimentally verified by Motais, Belin and Bonnelle (1981) and independently by Connerade and Karnatak (1981) who derived a slightly different form of equation 6(5) from a consideration of the Auger decay rate of the $3d^9$ core and the Coster-Kronig decay of the excited state $3d^7_{3/2} 4f^1$.

The suppression of the m_β intensity and the increased width of the m_4 absorption line can be very well explained by a consideration of Coster-Kronig decay paths for the excited state. The change in lineshape between the symmetrical m_5 and the slightly asymmetrical m_4 absorption lines has also been explained in terms of excited state Coster-Kronig transitions by Karnatak, Esteva and Connerade (1981). The $m_{\alpha,\beta}$ spectra of the heavier rare earths will also have components from competing transitions and it may be impossible to deconvolve the various competing processes.

6:2 Competing processes in the spectra of the heavy rare earths.

In the emission process, the initial and final states are not unambiguously defined and in particular the final state need not be the ground state. In lanthanum however, where there are overlapping $m_{\alpha,\beta}$ and $m_{5,4}$ emission and absorption lines

which are clearly resolved, the corresponding resonance absorptions and emissions ($m_4 - m_5$, $m_5 - m_4$) are found to have very similar linewidths. The resonance transition can in general be represented by,



where * represents an excited final state.

The $3d^{10} 4f^{n*}$ state must decay to the ground state $3d^{10} 4f^n$ giving an optical transition. The maximum difference between the ground state and the excited final state of the neutral atom is the ionisation limit of the optical states which can be represented by $3d^{10} 4f^{n-1}$. From the extensive tabulations of optical data by El'Yashevich (1953) for the rare earths, the ionisation limit is 0.2eV for $4f'$, 1.3eV for $4f'^2$ and 4.7eV for $4f'^3$. Between $4f'$ and $4f'^2$ the limit is in the region of 5.3eV. For lanthanum with an empty $4f$ shell after resonant emission the final state has to be very near the ground state. For triply ionised ytterbium and particularly for thulium, there can be a large difference between the ground state and the final state of the emission process.

The lines making up the optical absorption spectrum even broadened by thermal motion are only of the order of 0.1eV wide. Transitions into excited final states will therefore cause additional structure on the low energy side of a resonance line. The resonance line will be the highest energy member of the transitions into excited final states. The direct ionisation of a $3d$ electron will also lead to the transition,



This will give rise to higher energy lines than in the case of resonance emission. The initial and final states for emission in this case also correspond to the final and initial states for resonant line absorption in an atom with one less $4f$ electron. This will give multiplet emission on

the high energy side of a resonance component. In the case of lanthanum, only resonance transitions can occur due to the empty 4f level in the ground state. In contrast, in the case of ytterbium metal, as the 4f shell is full in the ground state resonance transitions cannot take place, but transitions described by equation 6(7) involving ionisation of the 3d shell can occur.

The $m_{\alpha,\beta}$ spectra of the heavy rare earths will therefore contain many features which will occur due to the existence of several different radiative and non radiative processes. These will cause the spectra to be much wider than the corresponding absorption structures. The spectra will be heavily overlapped and in many cases resonance and ionisation components will be indistinguishable.

6:3 The $m_{\alpha,\beta}$ region of lutetium fluoride

The $m_{\alpha,\beta}$ region of lutetium fluoride should consist of reasonably simple structures due to the absence of resonance transitions. Resonance transitions cannot take place due to the full 4f shell in lutetium fluoride. Due to the final state being $3d^{10} 4f^{13}$, from the optical data of El'Yashevich (1953) it can be seen that the final state must be close to the ground state. The ionisation transition in lutetium fluoride can be represented by,



The initial and final states for emission are the same as the final and initial states for resonant line absorption in triply ionised ytterbium. The $Yb_2 O_3$ m_5 linewidth has been measured by Karnatak, Esteva and Connerade (1981) to be 1.4eV after correction for instrumental broadening. This is in good agreement with a calculation of the $3d_{5/2}^9 4f^{14}$ linewidth by

Chen, Craseman and Mark (1980). The m_5 line absorption in Yb_2O_3 is therefore a singlet with a width of 1.4eV. The m_4 structure of lutetium fluoride should therefore also be a singlet with an observed width of 1.9eV with the inclusion of instrumental broadening for the present case.

The results presented in Chapter 5 show that the lutetium m_4 structure is characterised by a single peak with associated higher energy satellites. If a lorentzian is fitted to the lower energy side of the main peak, the best fit curve gives a width of 2.5eV fwhm. This would appear to be in reasonable agreement with the width of 1.9eV derived from the Yb_2O_3 m_5 line absorption. The main line can therefore be assigned to the ionisation transition given by equation 6(8). The existence of satellite emission in the m_4 spectra was assigned by Hirsh (1936, 1942) to the Coster-Kronig transition $M_3 M_5 N_{4,5}$. The m_3 subshell is initially ionised allowing the radiationless transition of an m_5 electron into the m_3 vacancy with emission of an $N_{4,5}$ electron. From the tabulations of Cooper (1944) this transition is possible for $Z < 89$.

The m_3 threshold as tabulated by Bearden and Burr (1967) occurs at a binding energy of 2023eV. To excite the Coster-Kronig transition proposed by Hirsh (1942), the excitation voltage would have to be in excess of 2023 volts and clearly from the data presented in Chapter 5 satellite emission persists below this excitation voltage. Due to the electron beam size being bigger than the effective vertical aperture on the sample defined by the crystal optics, together with the non uniform vertical current density on the sample, the absolute excitation functions of the ionisation and satellite components could not be measured. The ratio of satellite to ionization components was however measured at twenty points between 1900 and 3000

volts and a small fraction of extra emission was found to occur above the m_3 threshold. The ratio was not distorted by structure in the ionisation component excitation curve as ionisation probabilities have been found to increase gradually up to a maximum at approximately four times the ionisation threshold (Massey and Burhop, 1952). Some of the m_α satellites could therefore be associated with $M_3 M_5 N_{4,5}$ Coster-Kronig transitions but the majority of satellites must be due to another mechanism. From the work of McGuire (1972) and Chen, Craseman and Mark (1980), the only other Auger or Coster-Kronig transitions possible for lutetium which leave an m_5 hole and an outer shell hole necessary for satellite emission are the $M_4 M_5 O_3$ for $Z < 79$ and $M_4 M_5 N_{6,7}$ for $Z < 74$. Of these two possible transitions the $M_4 M_5 N_{6,7}$ is much stronger than the $M_4 M_5 O_3$ and increases in strength from lanthanum to ytterbium falling rapidly to zero between ytterbium and tungsten ($Z = 74$).

The $M_4 M_5 N_{6,7}$ Coster-Kronig transition could therefore explain the m_α satellites in lutetium but positive identification would require the measurement of the satellite threshold. This was not possible in the present study due to the already low intensity of satellite emission at the practical low energy extreme of the electron gun which was found to be 1900eV.

The m_β data for lutetium fluoride presented in Chapter 5 suggest that the satellite transitions must be more complex. If the $M_4 M_5 N_{6,7}$ or the $M_4 M_5 O_3$ Coster-Kronig transitions were totally responsible for the m_α satellites, no satellites would be expected in the case of m_β . In this case, the low energy side of m_β cannot be well fitted by a lorentzian. The high energy side of the peak is asymmetric with a large satellite emission. On reduction of the excitation voltage

to below the m_3 threshold the satellite intensity reduced to a small level but did persist. To leave a hole in the m_4 shell after an Auger or Coster-Kronig transition, the excitation voltage obviously needs to be greater than the m_3 threshold. Normal Coster-Kronig transitions cannot therefore be responsible for the satellite emission.

The excitation function for the ratio of the satellite to parent emission as a function of excitation voltage was found to be a more steeply varying function than for m_α . The statistics were too poor to determine whether there was enhanced emission over the m_3 threshold. The more strongly varying satellite emission in the case of m_β is shown by the reduction from 3.1 to 2.9eV fwhm for m_α and from 3.5 to 2.9eV fwhm for m_β over the excitation range 3.0 KV to 2.0 KV. At the low energy excitation energy limit of the gun both the m_α and m_β widths had fallen slightly further. This behaviour is very difficult to explain but the fact that the m_β satellites are more voltage sensitive than the m_α satellites might indicate that an autoionising transition is responsible which results in the removal of a 4f electron as suggested by Connerade and Karnatak (1981) to explain the m_β asymmetry in lanthanum. In the case of the lutetium fluoride m_β satellites a study of the excitation function at low energy might yield more information, but more information is likely to be gained by combining these measurements with energy loss spectroscopy and threshold Auger spectroscopy.

6:4 The m_α region of ytterbium metal

The data presented for ytterbium metal m_α in Chapter 5 show a very similar structure to the m_α spectrum of lutetium fluoride also recorded at 3.0 KV. This is to be expected as

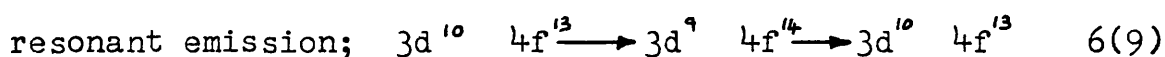
ytterbium metal also has a full 4f shell and so resonance transitions cannot occur. The ionisation transition is the same as for lutetium fluoride and is given by equation 6(8). The intensity of the satellites in this case was also very similar to those for lutetium fluoride. As discussed in Chapter 2, the ytterbium metal spectrum recorded by Karnatak (1971) is similar to the oxide spectra recorded in the same work. In the metallic spectrum, less emission was evident towards high energy but the overall structure was the same. The result obtained here suggests that the full 4f shell in the metal had lost a 4f electron through oxidation. The samples were prepared by evaporating a clean ytterbium film and then evaporating a thin coating of aluminium or some other protective layer. These films were prepared on targets in a separate chamber which could not achieve clean or ultra-high vacuum conditions. After evaporation the targets were removed from the evaporation plant and introduced into the direct bombardment x-ray tube used for soft x-ray studies. It seems possible therefore that in this process severe degradation of the ytterbium metal film took place. It is also possible that under the high temperature conditions in the x-ray gun alloying between the ytterbium sample and the protective coating took place which might have led to the emission of high energy structure. In this work no explanations of the nature of the metallic m_{α} spectrum was given. In the work of Parrott (1965) in which the m_{α} spectrum was measured, reproducible results could not be obtained and this was attributed to oxidation of the sample. In some spectra which were taken quickly after in situ evaporation a sharp reduction in width of the m_{α} region was observed. In the system described in Chapter 3, the best

possible ultra-high vacuum conditions were achieved, with a base pressure in the sample chamber of 2×10^{-10} Torr. In situ evaporation of the metallic sample was performed to ensure oxide free samples. Even under these conditions oxidation was too rapid for reliable data of good statistical accuracy to be recorded and so the multiple evaporation technique described in Chapter 5 was developed. The final m_x spectra recorded were therefore true metallic spectra. It can therefore be seen that the metallic m_x spectrum recorded by Fischer and Baun (1967) was also from a partially oxidised surface. The cause of high energy structure in ytterbium metal may also be related to the grain size of the structures in the evaporated film. It was reported by Bonnelle, Vergand and Karnatak (1973) that if the individual metal crystallites are less than 30\AA in size the occupation of the $4f$ shell drops from $4f^{14}$ to $4f^{13}$ with an increase in valency to three. From magnetic measurements, Leipfinger (1958) estimated that 2% of ytterbium metal atoms were trivalent and Lock (1957) estimated 0.5% were trivalent. In the measurements of Combley, Stewardson and Wilson (1968), although measuring a small m_x absorption in the metal corresponding to 1% of the metal atoms being trivalent, it was assumed that this was due to contamination. In the light of the measurements of Bonnelle, Vergand and Karnatak (1973), the observations of a small fraction of $4f^{13}$ metallic atoms could be due to the existence of small crystallites in the samples used. The existence of a small fraction of $4f^{13}$ atoms in the metal could give rise to a high energy structure similar to that in Yb_2O_3 . The size effect has only been studied for ytterbium but it is difficult to explain the existence of high energy structure in the case of lutetium fluoride on the same basis.

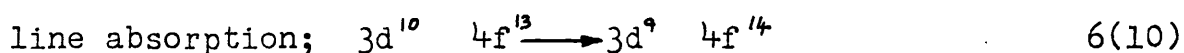
The data presented for the m_{α} region of ytterbium metal shows very similar structure to the m_{α} spectrum of lutetium fluoride. The main structure can therefore be identified as an ionisation transition of the type described by equation 6(8). The origin of the high energy satellite structure is unknown but due to the striking similarity between the ytterbium and lutetium fluoride spectra it is assumed the satellite structure in both is of the same origin. The m_{α} spectrum of ytterbium recorded at approximately 3.0 KV excitation energy has been measured in the metallic vapour phase by Brytov, Mstibovskaya and Rabinovich (1976). Due to the poor instrumental resolution used to record the metallic vapour phase m_{α} spectrum, exact comparisons between the solid and vapour spectra cannot be drawn but the spectra are similar with the peak emission at the same energy. The vapour phase spectrum also shows a high energy tail similar to the solid case. This result emphasises the essentially atomic nature of the rare earth $m_{\alpha,\beta}$ transitions.

6:5 The $m_{\alpha,\beta}$ region of ytterbium fluoride

In the form of an oxide or fluoride the occupancy of the 4f shell drops from $4f^{14}$ to $4f^{13}$ with an increase in valency from two to three. The result of this is that both ionisation transitions and resonance transitions can occur. The resonance transition can be represented by,

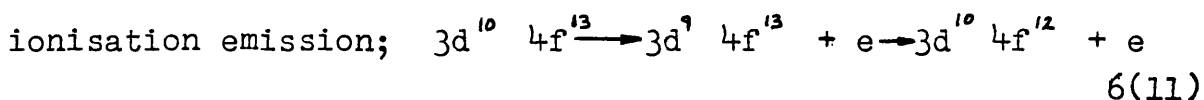


The initial and final states for emission are the final and initial states for absorption in ytterbium fluoride.



As in the case of lanthanum, components in the absorption and the emission spectrum will therefore lie at the same energy.

In the case of ytterbium fluoride however resonance transitions can occur in which the final state is an optical level 1.3eV above the ground state. This would result in the emission of lower energy resonance components of which the ground state resonance line would be the highest energy component. From the high resolution work of Karnatak, Esteve, and Connerade (1981), the intrinsic m_5 linewidth in Yb_2O_3 was found to be 1.4eV. For the m_α transitions in ytterbium and lutetium fluoride the linewidth of the ionisation component was measured to be 2.5eV fwhm. As the ionisation emission in ytterbium metal and lutetium fluoride is the same as the resonance emission in Yb_2O_3 the linewidths are expected to be similar. The resonance transition should occur at the same energy as the line absorption in ytterbium fluoride which has been measured by Combley Stewardson and Wilson (1968) to occur at 1520.0eV. If a lorentzian curve is fitted to the ytterbium fluoride 3.0 KV data at 1520.0eV, the best fit to the low energy side of the m_α peak gives a width of 3.6 eV fwhm. The fit to the low energy side of the m_α peak is not very good and indicates some lower energy emission. This is confirmed by the apparent broadening of the m_α resonance line and is ascribed to weak transitions into excited final states 1.3eV above the ground state. The higher energy structure will be due to the ionisation transition,



The reverse of this ionisation emission is the same as the resonance line absorption for thulium m_5 ,



The measurement of the thulium m_5 absorption gives three components, the strongest component being the centre line with

the two weaker lines at 2.0eV and 2.7eV lower and higher than the centre line respectively (Belrhmi-Belhassan, Karnatak, Spector and Bonnelle, 1981). The overall width of the structure was found to be 5.7eV. The ionisation and resonance transitions should overlap and therefore produce a composite structure. If the strong thulium m_5 peak is associated with the peak in the ytterbium fluoride m_α spectrum at 1522.8eV good agreement with the measured m_α spectrum is found. The lower energy component of the thulium m_5 triplet would lie at 1520.8eV compared to the main m_α peak at 1520.6eV. In addition, a small shoulder can be seen in the high energy structure at 1525.5eV. The separation of this feature from the component at 1522.8eV is therefore 2.7eV. This is exactly the separation of the main component and the weak high energy component in the thulium m_5 line absorption spectrum. The high energy structure can therefore be unambiguously identified as being due to an ionisation transition of the type represented by equation 6(11). It is clear from the data presented in Chapter 5 that the resonance transition is comparable in strength to the ionisation transition. If a spectrum is synthesised from the thulium m_5 ionisation emissions and from the lutetium or ytterbium m_α main line for the Yb F_3 resonance emission the composite structure has a width of 6.5eV. It was discussed earlier in this section that the fit of the ytterbium or lutetium m_α main line to the Yb F_3 spectrum at the resonance energy of 1520.0eV indicated that there was emission into an excited final state 1.3eV higher than the ground state which gave weak lower energy structure. The agreement between the composite spectrum, consisting of ionisation and resonance components giving a width of 6.5eV, and the observed spectrum with a width of 7.8eV is reasonable,

but if the extra low energy excited final state structure is taken into account the fit is very good.

On reduction of the excitation voltage, more resonance structure is to be expected due to the more sharply varying form of excitation functions than ionisation functions at low energy. The data presented in Chapter 5 also show this effect although the spectrum appears to have more weak high energy satellite emission.

The $m_{\alpha, \beta}$ spectra of Yb_2O_3 have been measured in fluorescence by La Villa (1974) and appear to disagree with the electron impact data presented in Chapter 5. The peak of the m_{α} spectrum appears at 1523.7eV instead of 1520.6eV in the present work, but the m_{β} appears to be in reasonable agreement at 1567.4eV to the present work value of 1567.7eV. The shape of the m_{β} generated in fluorescence is also quite similar to the m_{β} spectra presented in Chapter 5. If the m_{α} fluorescence spectrum is examined closely, a shoulder can be seen at 1520.0eV at approximately 15% of the main peak intensity. This corresponds to the m_{γ} absorption in Yb_2O_3 . The m_{β} line is similar to the present case because the m_{γ} absorption is not allowed for an initial state of $3d_{3/2}^{10} 4f^{13}$ and so no self absorption can occur. In the case of m_{γ} , there is a strong line absorption at 1520.0eV and therefore it can be concluded that the apparent shift of the m_{α} spectrum to 1523.7eV only occurs because the lower energy emission peak has been almost totally suppressed by m_{γ} self absorption. This interpretation is supported by the experimental details given by La Villa (1974). The primary x-ray beam and the analysing direction were at $\pm 45^\circ$ to the sample surface normal. Further to this, the samples were approximately 0.25 mm thick. Under these conditions

self absorption would have been very severe.

As the m_4 line absorption in YbF_3 is not allowed, identification of the resonance emission is not as easy for m_β as for m_α where a direct comparison with the m_5 spectrum can be made. Having identified the resonance component as lying at 1520.0eV for m_α , the spin-orbit splitting of the 3d level can be added to this value to give the energy of the m_β resonance component. The 3d spin orbit splitting is given by Bearden and Burr (1967) as 48.5eV and when added to the energy of the m_α resonance component at 1520.0eV gives the m_β resonance component to be at 1568.5eV. The data presented in Chapter 5 show the peak of m_β to lie at 1567.7eV and so this main peak must be the resonance component. The higher energy structure should again correspond to an ionisation transition which would give a component similar to the m_4 line absorption in thulium. The thulium m_4 component is much weaker than the triplet of lines making up the m_5 absorption structure and is situated 45.0eV higher in energy than the central m_5 component. This component has been identified as lying at 1522.8eV and so the single m_4 ionisation component should lie at 1567.8eV plus the difference between the thulium and ytterbium spin orbit splitting of the 3d $3/2, 5/2$ levels.

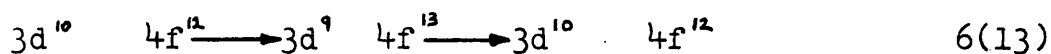
This is 2.6eV (Bearden and Burr, 1967) and therefore gives the ionisation component as being at 1570.4eV. This is in good agreement with a shoulder in the spectrum lying at 1570.0eV. There appears also to be some unresolved higher energy satellite emission. Similarly to the m_α case, on reduction of the excitation voltage to 2.0 KV, the ratio of resonance to ionisation components increases as expected.

The $m_{\alpha,\beta}$ spectra of ytterbium fluoride are therefore

made up of both resonance and ionisation components. A small amount of higher energy satellite emission is present in the spectra but it is overlapped with the ionisation components. The agreement with a resonance and ionisation transition model is good and the resonance and ionisation components have been identified in the $m_{\alpha,\beta}$ spectra.

6:6 The $m_{\alpha,\beta}$ region of thulium metal and fluoride

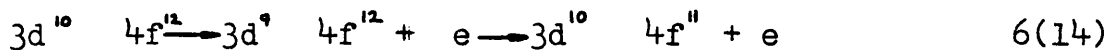
The $m_{\alpha,\beta}$ spectra of thulium metal should be similar to the $m_{\alpha,\beta}$ spectra of thulium fluoride due to the 4f shell containing twelve electrons in each case. The m_{α} spectrum of thulium metal should contain both resonance and ionisation emission components and excited final state low energy components. The resonance components can be represented by,



This will give resonance components at the same energy as the thulium m_{β} line absorptions. These are at 1460.2eV, 1462.2eV and 1464.9eV with the strongest component being in the middle and the weak m_{α} component being at 1507.2eV (Belrhmi-Belhassan, Karnatak, Spector and Bonnelle, 1981)

The data presented in Chapter 5 shows the peak of the thulium metal m_{α} spectrum to be at 1462.1eV in good agreement with the position of the strongest m_{β} resonance at 1462.2eV. There are no other resolved peaks in the m_{α} spectrum but there is evidence of submerged components at 1458.0eV and 1465eV. The lowest of the resonance components should lie at 1460.2eV and so the submerged component at 1458eV cannot be identified with resonance transitions to the ground state but might indicate resonance transitions to an excited final state. If the

submerged component at 1458eV is identified with excited final state resonance transitions it will represent the strongest m_5 resonance at 1462.2eV but for which the final state is near the ionisation limit of the $4f^{12}$ optical states. The ionisation limit is 4.7eV for thulium and seems to be in reasonable agreement with the energy difference between the submerged component at 1458eV and the main m_4 resonance component at 1462.2eV. The structure on the high energy side of the main m_4 peak should be made up of the highest energy m_5 resonance component and ionisation emission given by,



This will give structure which will be similar to the erbium m_5 absorption line components. From the work of Stewardson and Wilson (1956) it can be seen that the erbium m_5 structure consists of two principle lines and a weak third line at higher energy. Of the two principle lines, the higher energy line is slightly stronger. From the work of Sugar (1972) it can be seen that the m_5 region actually consists of seven components, the three mentioned above being the strongest, and the m_4 region consists of a narrowly spaced triplet which gives rise to a single wide observable structure. The width of the m_5 structure was found to be 5.6eV and the width of the m_4 was 3.5eV. The m_5 resonance of erbium would lead to high energy structure in the thulium m_4 spectrum, but due to the width of the both the thulium and erbium m_5 spectra the resulting m_4 spectrum is heavily overlapped with no resolvable higher energy components. If the lower energy resonance transitions are

included, the width of the m_{α} spectrum seems reasonable. The m_{β} spectrum of thulium metal is also expected to contain a resonance component and an ionisation component. As described above, the thulium m_{γ} absorption line has been measured and was found to lie at 1507.2eV and so should be present at the same energy in the m_{β} spectrum. A very weak rise in emission can be seen at this energy in the data, but the gross structure lies at lower energy with a peak at 1502.5eV and a shoulder at 1504.4eV. The measurements of thulium m_{β} by Fischer and Baun (1967) do not resolve the shoulder recorded in this work and put the peak of m_{β} at 1505eV but clearly this is still much too low to be identified as the resonance emission. The ionisation components will occur higher in energy than the resonance components and so some other mechanism must be responsible for the low energy structure. If the resonance emission intensity is similar to the corresponding line absorption intensity, then from the measurements of Belrhmi-Belhassan, Karnatak, Spector and Bonnelle (1981) it can be seen that the m_{γ} resonance would be very weak. If the intense low energy m_{β} structure is associated with resonance transitions into excited final states then it would be expected that the m_{β} peak would represent transitions to excited states near the ionisation limit. The difference in energy between the m_{β} peak and the m_{γ} resonance line is 4.7eV which is exactly the ionisation limit given by El'Yashevich (1953). The reason for the excited state transition being so intense is unknown but there are many excited states available for thulium where there is only one for ytterbium where this effect was observed to be much less intense.

The thulium metal and thulium fluoride spectra are very similar, in direct contrast to the case of ytterbium metal and fluoride. This is expected due to the same 4f occupation in the metal and fluoride. The greatest differences exist in the case of the thulium m_{α} structure identified with transitions to excited final states. These effects are small, with the gross structure being similar in the metal and fluoride.

6:7 Experimental Refinements

It is clear from the present study of the $m_{\alpha,\beta}$ spectra of the heavy rare earths that due to the heavy overlap of components in the spectra, if satisfactory deconvolution of the components is to be achieved very good statistical accuracy is required. In general however, the $m_{\alpha,\beta}$ spectra are weak and to achieve the statistical accuracy of the present study extremely long data collection cycles were needed. It is clear also that although the resolution achieved in the present study was adequate, resolution cannot be sacrificed to improve the data rate.

The data rate could be improved by increasing the beam current of the electron gun, but it was found that the power loading in the present arrangement was probably as high as possible due to the restricted water cooling rate dictated by the moveable anode. By altering the water cooling arrangement and changing to a copper anode, current densities up to a factor of ten higher might be achievable. For recording the spectra of the metallic rare earths it has been shown however that the beam current has to be very low if extremely rapid degradation of the sample is not to occur. The current density in the present study was probably the maximum that could be used and so the only

way to increase the data rate would be to increase the sensitivity of detection. The size of the crystal aperture cannot be increased as the instrumental resolution would be degraded. The only way to improve the detection efficiency without degrading the instrumental resolution would be to use an area detector along the Rowland circle. Area detectors for soft x-ray detection are now quite common and employ various techniques including x-ray sensitive diodes arrays, channel plate amplification and multiwire proportional counters. The gain factor in using some of these techniques would be simply the image width divided by the channel width, which would give in the present study a value of typically one hundred. This gain would certainly make the study of $m_{\alpha,\beta}$ structures much easier and allow a better deconvolution of overlapping components.

The design of the present electron gun did not allow the absolute excitation functions of spectral features to be obtained. With an area detection system, only the area of the $m_{\alpha,\beta}$ lines need be illuminated and this would mean that the electron beam current could be reduced to only several milliamps. Using a conventional three element tube electron lens and a single hairpin filament the focal spot on the sample surface could be kept to less than 1mm over the energy range of interest. (Harting and Read, 1976). Even for beam currents of the order of a few milliamperes, space charge repulsion would be significant but still a small spot size could be achieved which would remain reasonably constant as the beam energy was altered (Read, Comer, Imhof Brunt and Harting, 1974). The use of such an electron gun would significantly improve the $m_{\alpha,\beta}$ measurements.

With the use of these two techniques, the $m_{\alpha,\beta}$ measurements could be greatly enhanced. The measurement of the component excitation functions would be of great help in the identification of competing processes and the use of image plane area detection would allow far greater statistical accuracy to be achieved, making deconvolution much simpler and more exact. If an angle integrating electron detector could be used in the analysis chamber, electron spectroscopy could be used to monitor surface contamination and could also be used to study the electron excited Auger and Coster-Kronig transitions in the rare earths.

6:8 Conclusion

It has been shown in this study of the $m_{\alpha,\beta}$ spectra of the heavy rare earths that several competing processes take place to produce the observed structures. The gross structures have been shown to be due to both resonance and ionisation transitions although it is evident that the processes may be complicated by excited final state effects. It can also be concluded that most of the fairly limited $m_{\alpha,\beta}$ measurements published so far have been distorted by self-absorption or the effects of contamination or poor resolution. The explanation of the gross structures in the $m_{\alpha,\beta}$ spectra appear to be well explained in terms of resonance and ionisation transitions although much theoretical work needs to be done in this area. To carry interpretation of the $m_{\alpha,\beta}$ structures any further needs the implementation of image plane area detection so that better statistical accuracy can be achieved and the use of a small spot size tuneable electron gun so that excitation functions can be measured.

With these instrumental developments and theoretical effort in this area the origin of the $m_{\alpha,\beta}$ structures may be as well determined as the origin of the $m_{4,5}$ absorption spectra.

APPENDIX A.

Cross assembled version of a simple control program.

```

000001
000002      FED1      OUTEE
000003      FFFF1     POATAE
000004      FF35     INEEER
000005      FF73     BADDR
000006      FF96     BYTE
000007      8000C    DR3A
000008      8000D    CR3A
000009      8000E    DR3B
000010      8000F    CR3B
000011      8010    DR4A
000012      8011    CR4A
000013      8012    DR4B
000014      8013    CR4B
000015      8014    DR5A
000016      8015    CR5A
000017      8016    DR5B
000018      8017    CR5B
000019      8018    DR6A
000020      8019    CR6A
000021      801A    DR6B
000022      801B    CR6B
000023      801C    DR7A
000024      801D    CR7A
000025      801E    DR7B
000026      801F    CR7B
000027      8000    ACIAS
000028      0000    MEM1
000029      0002    MEM2
000030      0004    MEM3
000031      0006    MEM4
000032      0008    MEM5
000033      000A    MEM6
000034      000C    MEM7
000035      000E    MEM8
000036      0010    MEM9
000037      0012    TEM1
000038      0013    TEM2
000039      0014    TEM3
000040      0015    TEM4
000041      0016    TEM5
000042      0017    TEM6
000043      0018    TEM7
000044      0019    TEM8
000045      001A    TEM9
000046      0100    ORG
000047

```

```

000048
000049      *
000050      *SET UP PIAS FOR INPUT/OUTPUT.
000051      *SET STEPPERS TO STOP.
000052      *
000053      *
000054      *PORT 3
000055      * DR3A INPUT ;
000056      * DR3B INPUT ;
000057      *
000057      0100    7F    800D    CLR    CR3A
000058      0103    7F    800F    CLR    CR3B
000059      0106    7F    800C    CLR    DR3A

```

```

000060 0109 7F 800E          CLR      DR3B
000061 010C 86 04          LDA  A   #804
000062 010E 87 800D        STA  A   CR3A
000063 0111 87 800F        STA  A   CR3B
000064
000065          *
000066          *PORT 4
000067          * DR4A INPUT ;
000068          * DR4B INPUT ;
000069          *
000069 0114 7F 8011          CLR      CR4A
000070 0117 7F 8013          CLR      CR4B
000071 011A 7F 8019          CLR      DR4A
000072 011D 7F 8012          CLR      DR4B
000073 0120 86 04          LDA  A   #804
000074 0122 87 8011        STA  A   CR4A
000075 0125 87 8013        STA  A   CR4B
000076
000077          *
000078          *PORT 5
000079          * DR5A INPUT ;
000080          * DR5B INPUT ;
000081          *
000081 0128 7F 8015          CLR      CR5A
000082 012B 7F 8017          CLR      CR5B
000083 012E 7F 8014          CLR      DR5A
000084 0131 7F 8016          CLR      DR5B
000085 0134 86 04          LDA  A   #804
000086 0136 87 8015        STA  A   CR5A
000087 0139 87 8017        STA  A   CR5B
000088
000089          *
000090          *
000091          *PORT 6
000092          * DR6A OUTPUT ;
000093          * DR6B OUTPUT ;
000094          *
000094 013C 7F 8019          CLR      CR6A
000095 013F 7F 801B          CLR      CR6B
000096 0142 86 FF          LDA  A   #FF
000097 0144 87 8018        STA  A   DR6A
000098 0147 87 801A        STA  A   DR6B
000099 014A 86 04          LDA  A   #804

001000 014C 87 8019          STA  A   CR6A
001001 014F 87 801B          STA  A   CR6B
001002
001003          *
001004          *PORT 6
001005          * DR7A INPUT ;
001006          * DR7B INPUT ;
001007          *
001007 0152 7F 801D          CLR      CR7A
001008 0155 7F 801F          CLR      CR7B
001009 0158 7F 801C          CLR      DR7A
001010 015B 7F 801E          CLR      DR7B
001011 015E 86 04          LDA  A   #804
001012 0160 87 801D        STA  A   CR7A
001013 0163 87 801F        STA  A   CR7B
001014
001015          *
001016          * SET UP STEPPER MOTORS.
001017          * SET TO OFF.
001018          *
001018 0166 86 00          LDA  A   #00
001019 0168 87 8018        STA  A   DR6A
001020
001021          *
001022          * INHIBIT RECORDER.
001023          *
001023 016B 86 02          LDA  A   #02
001024 016D 87 801A        STA  A   DR6B
001025
001026          *
001027          * MAIN CALLING ROUTINE
001028          *
001029          * PRINT PROMPT
001030          *

```

```

00131 0170 CE 03FE LP LDX #TEX1
00132 0173 BD FFF1 JSR PDATA1
00133 *
00134 * WAIT FOR OPTION
00135 *
00136 0176 BD FE85 LP0 JSR INEE
00137 0179 81 41 CMP A #841
00138 0173 26 03 BNE LP1
00139 0170 7E 01C5 JMP MOVE
00140 0180 81 42 LP1 CMP A #842
00141 0182 26 03 BNE LP2
00142 0184 7E 03E9 JMP CAL
00143 0187 81 43 LP2 CMP A #843
00144 0189 26 03 BNE LP3
00145 0188 7E 03EC JMP SYNC
00146 018E 81 44 LP3 CMP A #844
00147 0190 26 03 BNE LP4
00148 0192 7E 02D7 JMP SCAN1
00149 0195 81 45 LP4 CMP A #845
00150 0197 26 03 BNE LP5
00151 0199 7E 03EF JMP SCAN2

00152 019C 81 46 LP5 CMP A #846
00153 019E 26 03 BNE LP6
00154 01A0 7E 03F2 JMP SCAN3
00155 01A3 81 47 LP6 CMP A #847
00156 01A5 26 03 BNE LP7
00157 01A7 7E 03F5 JMP DUM1
00158 01AA 81 48 LP7 CMP A #848
00159 01AC 26 03 BNE LP8
00160 01AE 7E 03F8 JMP DUM2
00161 01B1 81 49 LP8 CMP A #849
00162 01B3 26 03 BNE LP9
00163 01B5 7E 03FB JMP DUM3
00164 01B8 BD 01BE LP9 JSR ERROR
00165 01BB 7E 0170 JMP LP
00166 *
00167 * SENDS ERROR SIGNAL TO SCREEN
00168 *
00169 01BE CE 0423 ERROR LDX #TEX2
00170 01C1 BD FFF1 JSR PDATA1
00171 01C4 39 * RTS
00172 *
00173 * THIS IS THE MOVE ROUTINE ; A
00174 *
00175 * ASK FOR POSITION
00176 *
00177 01C5 CE 0441 MOVE LDX #TEX3
00178 01C8 BD FFF1 JSR PDATA1
00179 *
00180 * WAIT FOR ENTRY
00181 *
00182 01CB BD 0299 E2 JSR ENTRY
00183 *
00184 * ISSUE PROMPT
00185 * G GO ; R RE-ENTER
00186 *
00187 01CE CE 045E F1 LDX #TEX4
00188 01D1 BD FFF1 JSR PDATA1
00189 01D4 BD FE85 F2 JSR INEE
00190 01D7 97 12 STA A TEM1
00191 01D9 81 52 CMP A #852
00192 01DB 26 09 BNE E3
00193 01DD CE 047D LDX #TEX5
00194 01E0 BD FFF1 JSR PDATA1
00195 01E3 7E 01CB JMP E2
00196 01E6 96 12 E3 LDA A TEM1
00197 01E8 81 47 CMP A #847
00198 01EA 26 10 BNE E4
00199 01EC CE 048B LDX #TEX6
00200 01EF BD FFF1 JSR PDATA1
00201 01F2 86 44 LDA A #844

```

```

00202 01F4 97 13          STA A   TEM2
00203 01F6 BD 0202       JSR    MOVEIT

00204 01F9 7E 0170       JMP    LP
00205 01FC BD 01BE E4    JSR    ERROR
00206 01FF 7E 01D4       JMP    F2
00207 *
00208 *
00209 * THIS ROUTINE READS THE ADC,
00210 * & DRIVES THE ASSOCIATED STEPPER
00211 * UNTIL ADC=MEM1.
00212 *
00213 * TEM2 MUST CONTAIN 41,42,43,44
00214 * CORRESPONDING TO STEPPER SLOW,
00215 * MEDIUM, FAST, V.FAST.
00216 *
00217 *
00218 * READ ADC AND STORE AT MEM2
00219 *
00220 0202 B6 8016 MOVEIT LDA A   DR5B
00221 0205 97 02          STA A   MEM2
00222 0207 B6 8014       LDA A   DR5A
00223 020A 97 03          STA A   MEM2+$1
00224 *
00225 * FWD ON STEPPER CONTROL
00226 * REDUCES ADC LEVEL.
00227 *
00228 * COMPARE MEM2 & MEM1.
00229 *
00230 020C 96 00 T1     LDA A   MEM1
00231 020E 91 02         CMP A   MEM2
00232 0210 27 06         BEQ    N1
00233 0212 91 02         CMP A   MEM2
00234 0214 22 0E         BHI    REV
00235 0216 20 12         BRA    FWD
00236 0218 96 01 N1     LDA A   MEM1+$1
00237 021A 91 03         CMP A   MEM2+$1
00238 021C 27 52         BEQ    STOP
00239 021E 91 03         CMP A   MEM2+$1
00240 0220 22 02         BHI    REV
00241 0222 20 06         BRA    FWD
00242 0224 86 00 REV    LDA A   #B00
00243 0226 97 16         STA A   TEM3
00244 0228 20 04         BRA    FWDD
00245 022A 86 FF FWD    LDA A   #FFF
00246 022C 97 16         STA A   TEM5
00247 022E 06 13 FWDD   LDA B   TEM2
00248 0230 06 13         LDA B   TEM2
00249 0232 C1 41         CMP B   #$41
00250 0234 27 1A         BEQ    FWD1
00251 0236 C1 42         CMP B   #$42
00252 0238 27 10         BEQ    FWD2
00253 023A C1 43         CMP B   #$43
00254 023C 27 06         BEQ    FWD3
00255 023E 86 1C         LDA A   #X00011100

00256 0240 97 15          STA A   TEM4
00257 0242 20 10         BRA    FINI
00258 0244 86 6C FWDD3  LDA A   #X01101100

```

```

00259 0246 97 15 STA A TEM4
00260 0248 20 0A BRA A FINI
00261 024A 2C FWD2 LDA A #X00101100
00262 024C 97 15 STA A TEM4
00263 024E 20 04 BRA A FINI
00264 0250 86 4C FWD1 LDA A #X01001100
00265 0252 97 15 STA A TEM4
00266 0254 96 16 FINI LDA A TEM5
00267 0256 81 FF CMP A #FFF
00268 0258 27 09 BEQ A FWD
00269 025A 96 15 LDA A TEM4
00270 025C 84 F7 AND A #X11110111
00271 025E B7 8018 STA A DR6A
00272 0261 20 05 BRA A F5
00273 0263 96 15 FWD LDA A TEM4
00274 0265 B7 8018 STA A DR6A
00275 0268 B0 0292 F5 JSR DELAY
00276 026B B0 027C JSR CHECK
00277 026E 20 92 BRA A MOVEIT
00278 0270 86 00 STOP LDA A #00
00279 0272 B7 8013 STA A DR6A
00280 0275 CE 0493 LDX A #TEX7
00281 0278 B0 FFF1 JSR PDATA1
00282 027B 39 RTS
00283 027C B6 8001 CHECK LDA A ACIAS+$1
00284 027F 84 7F AND A #7F
00285 0281 81 2E CMP A #2E
00286 0283 26 0C BNE J2
00287 0285 CE 0493 LDX A #TEX7
00288 0288 B0 FFF1 JSR PDATA1
00289 028B B0 0270 JSR STOP
00290 028E 7E 0170 JMP LP
00291 0291 39 J2 RTS
00292 0292 CE 0FFF DELAY LDX #0FFF
00293 0295 09 D1 DEX
00294 0296 26 FD BNE D1
00295 0298 39 RTS
00296
00297
00298
00299
00300
00301
00302
00303
00304
00305
00306 0299 B0 FF73 ENTRY JSR BADDR
00307 029C DF 00 STX MEM1

```

```

*
*
*ROUTINE MODIFIES BADDR SO
*ONLY 4 DIGIT DEC. NUMBERS
*CAN BE ENTERED. NUMBER
*STORED IN INDEX REG & MEM1.
*IF ILLEGAL DIGITS ARE ENTERED,
*ERROR MESSAGE IS PRINTED.
*
*
00308 029E 86 0F LDA A #X00001111
00309 02A0 94 01 AND A MEM1+$1
00310 02A2 80 09 SUB A #09
00311 02A4 23 06 BLS C1
00312 02A6 B0 01BE JSR ERROR
00313 02A9 7E 0299 JMP ENTRY
00314 02AC 86 F0 C1 LDA A #X11110000
00315 02AE 94 01 AND A MEM1+$1
00316 02B0 80 90 SUB A #90
00317 02E2 23 06 BLS C2
00318 02E4 B0 01BE JSR ERROR
00319 02E7 7E 0299 JMP ENTRY
00320 02BA 86 0F C2 LDA A #X00001111
00321 02EC 94 03 AND A MEM1
00322 02FE 80 09 SUB A #09
00323 02C0 23 06 BLS C3
00324 02C2 B0 01BE JSR ERROR
00325 02C5 7E 0299 JMP ENTRY
00326 02C8 86 F0 C3 LDA A #X11110000
00327 02CA 94 00 AND A MEM1
00328 02CC 80 90 SUB A #90
00329 02CE 23 06 BLS C4

```

```

00330 0200 BD 01BE          JSR    ERROR
00331 0203 7E 0299          JMP    ENTRY
00332 02D6 39                C4    RTS
00333 *
00334 *
00335 * THIS IS THE SCAN 1 ROUTINE
00336 *
00337 *
00338 0207 CE 049D SCAN1 LDX    #TEX9
00339 02DA BD FFF1          JSR    PDATA1
00340 *
00341 * ASK FOR START-FINISH
00342 *
00343 02DD CE 04B1 SCANN LDX    #TEX9
00344 02E0 BD FFF1          JSR    PDATA1
00345 02E3 BD 0299          JSR    ENTRY
00346 02E6 DF 04            STX    MEM3
00347 02E8 86 20            LDA    A #20
00348 02EA BD FED1          JSR    OUTEEE
00349 02ED BD 0299          JSR    ENTRY
00350 02FC DF 06            STX    MEM4
00351 *
00352 * CHECK TO SEE IF SPECT
00353 * SCAN IS IN CAL DIRECTION
00354 *
00355 02F2 BD 038A          JSP    CHEKT
00356 02F5 81 FF            CMP    A #FF
00357 02F7 27 09            BEQ    NN1
00358 02F9 CE 04CD          LDX    #TEX10
00359 02FC BD FFF1          JSR    PDATA1

00360 02FF 7E 02DD          JMP    SCANN
00361 *
00362 * ASK FOR SCAN SPEED.
00363 * STORE AT TEM9.
00364 *
00365 0302 CE 04E8 NN1 LDX    #TEX11
00366 0305 BD FFF1          JSR    PDATA1
00367 0308 BD FE85          JSR    INEE
00368 030B 81 44            CMP    A #44
00369 030D 27 11            BEQ    NN2
00370 030F 81 43            CMP    A #43
00371 0311 27 0D            BEQ    NN2
00372 0313 81 42            CMP    A #42
00373 0315 27 09            BEQ    NN2
00374 0317 81 41            CMP    A #41
00375 0319 27 05            BEQ    NN2
00376 031B BD 01BE          JSR    ERROR
00377 031E 2C E2          BRA    NN1
00378 0320 97 1A NN2 STA    A TEM9
00379 *
00380 * ASK FOR RECORDING Y-N.
00381 * STORE AT TEM8
00382 *
00383 0322 CE 0504          LDX    #TEX12
00384 0325 BD FFF1          JSR    PDATA1
00385 0328 BD 03D2          JSR    YESNO
00386 032B 97 19          STA    A TEM8
00387 *
00388 * G GO ; R RE-ENTER
00389 * IF GO, ACCA=$FF ON EXIT.
00390 *
00391 032D BD 03AE          JSR    GOGO
00392 0330 81 FF            CMP    A #FF
00393 0332 27 08            BEQ    NN3
00394 0334 CE 047D          LDX    #TEX5
00395 0337 BD FFF1          JSR    PDATA1
00396 033A 2C A1          BRA    SCANN
00397 033C CE 048B NN3 LDX    #TEX6
00398 033F BD FFF1          JSR    PDATA1
00399 *
00400 * THIS ROUTINE MODIFIES THE

```

```

00401
00402
00403
00404
00405
00406
00407 0342 86 50
00408 0344 DE 04
00409 0346 08
00410 0347 4A
00411 0348 26 FC
* ACTION OF MOVEIT BY REMOVING
* BACKLASH IN SPECT DRIVE.
*
* GO TO POS. 750 HIGHER THAN
* MEM3.
*
BLASH LDA A #50
LDX MEM3
BL1 INX
DEC A
BNE BL1

00412 034A DF 10
00413 034C DF 00
00414 034E 86 44
00415 0350 97 13
00416 0352 BD 0202
00417 0355 BD 03A7
00418 0358 DE 04
00419 035A DF 00
00420 035C 86 44
00421 035E 97 13
00422 0360 BD 0202
00423 0363 BD 03A7
STX MEM9
STX MEM1
LDA A #44
STA A TEM2
JSR MOVEIT
JSR DELAY1
LDX MEM3
STX MEM1
LDA A #44
STA A TEM2
JSR MOVEIT
JSR DELAY1
*
* BACKLASH REMOVED
*
* SWITCH ON RECORDER IF
* REQUIRED.
*
00424
00425
00426
00427
00428
00429
00430 0366 96 19
00431 0368 81 FF
00432 036A 26 05
00433 036C 86 00
00434 036E B7 801A
LDA A TEM3
CMP A #FF
BNE BL2
LDA A #00
STA A DR6B
*
* SET SPEED & START SCAN
*
BL2 LDA A TEM9
STA A TEM2
LDX MEM4
STX MEM1
JSR MOVEIT
LDX #TEX13
JSR PDATA1
*
* SWITCH OFF RECORDER
* & RETURN
*
00435
00436
00437
00438 0371 96 1A
00439 0373 97 13
00440 0375 DE 06
00441 0377 DF 00
00442 0379 BD 0202
00443 037C CE 0519
00444 037F BD FFF1
LDA A #02
STA A DR6B
JMP LP
*
* ROUTINE CHECKS TO SEE IF NUMBER
* IN MEM4 < OR EQU MEM3. IF SO ACCA
* IS SET TO $FF; IF NOT $00.
*
00445
00446
00447
00448
00449 0382 86 02
00450 0384 B7 801A
00451 0387 7E 0170
CHEKT LDA A MEM4
CMP A MEM3
BEQ CHEKN
CMP A MEM3
BLS CHEK
CHET LDA A #00
BRA CHEKT1
00452
00453
00454
00455
00456
00457 038A 96 06
00458 038C 91 04
00459 038E 27 08
00460 0390 91 04
00461 0392 23 10
00462 0394 86 00
00463 0396 26 0E

```

```

00464 03 98 96 07 CHEKN LDA A MEM4+$1
00465 03 9A 91 05 CMP A MEM3+$1
00466 03 9C 27 F6 BEQ CHET
00467 03 9E 91 05 CMP A MEM3+$1
00468 03 A0 23 02 BLS CHEK
00469 03 A2 20 F0 BRA CHET
00470 03 A4 86 FF CHEK LDA A #FFF
00471 03 A6 39 CHEKT1 RTS
00472 03 A7 CE 6FFF DELAY1 LDX #6FFF
00473 03 AA 09 DD1 DEX
00474 03 AB 26 FD BNE DD1
00475 03 AD 39 RTS
00476
00477 *
00478 * ROUTINE ISSUES PROMPT G GO
00479 * R RE-ENTER. CHECKS TO SEE IF
00480 * EITHER G OR R IS ENTERED. IF
00481 * G ACCA=$FF; IF R ACCA=$00
00482 03 AE CE 045E GOGO LDX #TEX4
00483 03 B1 BD FFF1 JSR PDATA1
00484 03 B4 BD FE85 GOGO1 JSR INEE
00485 03 B7 97 12 STA A TEM1
00486 03 B9 81 47 CMP A #$47
00487 03 BB 27 12 BEQ GOGO4
00488 03 BD 96 12 LDA A TEM1
00489 03 BF 81 52 CMP A #$52
00490 03 C1 27 08 BEQ GOGO3
00491 03 C3 CE 0423 LDX #TEX2
00492 03 C6 BD FFF1 JSR PDATA1
00493 03 C9 20 E9 BRA GOGO1
00494 03 CB 86 00 GOGO3 LDA A #000
00495 03 CD 20 02 BRA GOGO5
00496 03 CF 86 FF GOGO4 LDA A #FFF
00497 03 D1 39 GOGO5 RTS
00498
00499 *
00500 * ROUTINE WAITS FOR EITHER
00501 * Y OR N; IF Y, ACCA=$FF,
00502 * IF N, ACCA=$00.
00503 03 D2 BD FE85 YESNO JSR INEE
00504 03 D5 81 59 CMP A #$59
00505 03 D7 27 00 BEQ YES
00506 03 D9 81 4E CMP A #$4E
00507 03 DB 27 05 BEQ NO
00508 03 DD BD 01BE JSR ERROR
00509 03 DE 20 F0 BRA YESNO
00510 03 E2 86 00 NO LDA A #000
00511 03 E4 20 02 BRA YES1
00512 03 E6 86 FF YES LDA A #FFF
00513 03 E8 39 YES1 RTS
00514 03 E9 7E 0170 CAL JMP LP
00515 03 EC 7E 0170 SYNC JMP LP

00516 03 EF 7E 0170 SCAN2 JMP LP
00517 03 F2 7E 0170 SCAN3 JMP LP
00518 03 F5 7E 0170 DUM1 JMP LP
00519 03 F8 7E 0170 DUM2 JMP LP
00520 03 FB 7E 0170 DUM3 JMP LP

```

```

00521
00522
00523
00524
00525
00526 03FE 0D
          03FF 0A
          0400 0A

          *
          * TEXT ROUTINES
          *
TEX1  FCB  $0D,$0A,$0A

00527 0401 48          FCC  /HAPLINK 2.1 : 19,5,80
00531 0423 0D          TEX2  FCB  $0D,$0A,$0A
          0424 0A
          0425 0A
00532 0426 45          FCC  /ERROR : RE-ENTER COMMAND/

          0417 30
          0418 0D
          0419 0A
00528 041A 0A          FCC  $0D,$0A,$0A
          041B 40
          041C 4F
          041D 44

          043F 0A
          0440 04
00534 0441 0D          TEX3  FCB  $0D,$0A,$0A
          0442 0A
          0443 0A
00535 0444 41          FCC  /ADC POSITION REQUIRED ?/
          0445 44
          0446 43
          0447 20

          045C 0A
          045D 04
00537 045E 0D          TEX4  FCB  $0D,$0A,$0A
          045F 0A
          0460 0A
00538 0461 47          FCC  /G FOR GO ; R FOR RE-ENTER/
          0462 20

          047C 04
          047D 0D
          047E 0A
00540 047F 0A          ,TEX5  FCB  $0D,$0A,$0A
          0480 52
          0481 45
          0482 2D
          0483 45
          0484 4E
          0485 54
          0486 45
          0487 52
00542 0488 0D          FCC  $0D,$0A,4
          0489 0A
          048A 04
00543 048B 0D          TEX6  FCB  $0D,$0A,$0A
          048C 0A
          048D 0A
00544 048E 47          FCC  /GO/

```

00545	04 90 0D 04 91 0A 04 92 04		FCB	\$00, \$0A, 4
00546	04 93 0D 04 94 0A 04 95 0A	TEX7	FCB	\$00, \$0A, \$0A
00547	04 96 53 04 97 54 04 98 4F		FCC	/STOP/
00548	04 99 50 04 9A 00 04 9B 0A		FCB	\$00, \$0A, 4
00549	04 9C 04 04 9D 00 04 9E 0A	TEX8	FCB	\$00, \$0A, \$0A
00550	04 9F 0A 04 A0 53 04 A1 43		FCC	/SCAN ROUTINE 1/
00552	04 B0 04 04 B1 0D 04 B2 0A	TEX9	FCB	\$00, \$0A, \$0A
00553	04 B3 0A 04 B4 53 04 B5 54 04 B6 41		FCC	/START-FINISH POSITIONS/
00555	04 CC 04 04 CD 0D 04 CE 0A	TEX10	FCB	\$00, \$0A, \$0A
00556	04 CF 0A 04 D0 45 04 D1 52 04 D2 52		FCC	/ERROR: START < FINISH/
00558	04 E7 04 04 E8 0D 04 E9 0A	TEX11	FCB	\$00, \$0A, \$0A
00559	04 EA 0A 04 EB 53 04 EC 43		FCC	/SCAN SPEED ; 1,2,3,4 ?/
00561	05 03 04 05 04 0D 05 05 0A	TEX12	FCB	\$00, \$0A, \$0A
00562	05 06 0A 05 07 52 05 08 45 05 09 43		FCC	/RECORDING Y - N/
00563	05 15 4E 05 16 0D 05 17 0A		FCB	\$00, \$0A, 4
00564	05 18 04 05 19 0D 05 1A 0A	TEX13	FCB	\$00, \$0A, \$0A
00565	05 1B 0A 05 1C 45 05 1D 4E		FCC	/END OF SCAN/

REFERENCES

- (1) Åberg T., 1973 Proc. International Symposium on X-ray Spectra and Electronic Structure of Matter, Vol. 1,1, (München)
- (2) Åberg T., and Utriainen J., 1973, Phys. Rev. Lett. 22, 1346
- (3) Allison S.K., 1931, Phys. Rev. 38, 203
- (4) Backlin E., 1924, Z.Phys. 27, 30
- (5) Bearden J.A., 1931A, Phys. Rev. 37, 1210
- (6) Bearden J.A., 1931B, Phys. Rev. 38, 2089
- (7) Bearden J.A., 1967, Rev. Mod. Phys. 39, 78
- (8) Bearden J.A. and Burr A.F., 1967, Rev. Mod. Phys. 39, 125
- (9) Bearden J.A. and Shaw C.H., 1935, Phys. Rev. 48, 18
- (10) Belin E., 1967, Ph.D. Thesis, University of Paris
- (11) Belrhmi-Belhassan A., Karnatak R.C., Spector N., and Bonnell C., 1981, Phys. Lett. 82A, 174
- (12) Berreman D.W., 1955, Ph.D. Thesis, Cal.Tech. Pasadena, California
- (13) Beuthe H., 1930, Z Phys. 60, 603
- (14) Blackman M., 1951, Proc. Phys. Soc. 64B, 624
- (15) Bonnelle C. and Karnatak R.C., 1969, C.R. Acad. Sci. 268, 494
- (16) Bonnelle C. and Karnatak R.C., 1970, 8th Rare Earth Research Conf., Edition du Centre National de la Recherche Scientifique, Vol. 1, 515
- (17) Bonnelle C., Karnatak R.C. and Sugar J., 1974, Phys. Rev. A9, 1920

- (18) Bonnelle C., Karnatak R.C., and Spector N., 1977, J.Phys.B. 10, 795
- (19) Bonnelle C., Vergand F. and Karnatak R.C., 1973, Proc. 10th Rare Earth Conf. (Carefree, Arizona)
- (20) Brigham E.O., 1974 The Fast Fourier Transform (Prentice-Hall)
- (21) Brytov I.A., Mstibouskaya L.E. and Rabinovich L.G., 1976, Bull. Acad. Sci., USSR, Phys Ser (USA) 40, 2,72
- (22) Cauchois Y.J., 1932, Phys.et. Rad. 3,7,320
- (23) Cauchois Y.J. and Hulubei H., 1947, Longueur d'Onde des Emission et des Discontinuités d'Absorption X (Hermann, Paris)
- (24) Chamberlain M.B., Burr A.F. and Liefeld R.J., 1974 Phys. Rev. 9A, 663
- (25) Chen M.H., Crasemann B., and Mark H., 1980 Phys. Rev. 21A, 449
- (26) Combley F.H., 1963, Ph.D. Thesis, University of Leicester
- (27) Combley F.H., Stewardson E.A. and Wilson J.E., 1968, J. Phys. B. 1, 120
- (28) Connerade J.P. and Karnatak R.C., 1981 J. Phys. F. 11, 1539
- (29) Compton A.H. and Allison S.K., 1935, X-rays in Theory and Experiment, Ch. 9. (Van Nostrand, London)
- (30) Condon E.U. and Shortley G.H., 1935, The Theory of Atomic Spectra. (C.U.P.)
- (31) Cooper J.N., 1944, Phys.Rev. 65, 155
- (32) Coster D. and Kronig R.DeL., 1935, Physica 2, 13
- (33) Coulson C.A. and Sharma C.S., 1962, Proc. Phys. Soc. 79, 920

- (34) Crisp R.S., 1983, J. Phys.F. 13, 1325
- (35) Curzon A.E. and Chlebek H.G., 1973, J. Phys. F. 3, 1
- (36) Darwin C.G., 1914, Phil. Mag. 27, 315, 675
- (37) Demekin V.F. and Sachenko V.P., 1966, Sov. Phys. - JETP 22, 532
- (38) Deodhar G.B., 1962, Proc. Nat. Acad. Sci. (India) A 32, 320
- (39) Didsman S.A., 1961, Bull. Acad. Sci., USSR, Phys.Ser. (USA) 25, 935
- (40) Druyvesteyn M.J., 1928, Z. Phys. 43, 707
- (41) Eadie W.T., Dryard D., James F.E., Roos M and Sadoulet B, 1971, Statistical Methods in Experimental Physics. (North Holland)
- (42) El'Yashevich, 1953, Spectra of the Rare Earths, State Publishing House of Technical-Theoretical Literature (Moscow)
- (43) Ewald P.P., 1916, Ann. Phys. (Leipzig) 49, 1, 117
- (44) Ewald P.P., 1917, Ann. Phys. (Leipzig) 54, 519
- (45) Fischer D.W. and Baun W.L., 1967, J. Appl. Phys. 38, 4830.
- (46) Fock V.A. and Kolpinsky V.A., 1940, J. Phys. USSR, 3, 125
- (47) Ford O.R., 1932, Phys.Rev. 41, 577
- (48) Gschneidner K.A., and Smoluchowski R., 1963 J. Less Common Metals, 5, 374
- (49) Hall R., 1979, Private Communication, University of Leicester

- (50) Harting E. and Read F.H., 1976 Electrostatic Lenses (Amsterdam: Elsevier)
- (51) Hirsh F.R. (Jnr), 1931, Phys. Rev. 38, 914
- (52) Hirsh F.R. (Jnr), 1936, Phys. Rev. 50, 191
- (53) Hirsh F.R. (Jnr), 1941, Phys. Rev. 59, 766
- (54) Hirsh F.R. (Jnr), 1942, Rev. Mod. Phys. 14, 45
- (55) James R.W., 1954, The Optical Principles of the Diffraction of X-rays. (Bell, London)
- (56) Johann H.H., 1931, Z.Phys. 69, 185
- (57) Johansson T., 1933, Z.Phys. 82, 507
- (58) Karnatak R.C., 1971, Ph.D. Thesis, University of Paris
- (59) Karnatak R.C., Esteva J.M., and Connerade J.P., 1981, J. Phys.B. 14, 4747
- (60) Knowles J.W., 1965, Crystal Diffraction Spectroscopy of Nuclear γ - Rays, in, Alpha, Beta and Gamma-Ray Spectroscopy. Vol 1. (K. Siegbahn, ed., North-Holland)
- (61) Kunzle V.C.R., 1935, Acad.Sci. (Paris) 201, 16, 656
- (62) LaVilla R.E., 1974, Phys.Rev. 9A, 1801
- (63) Lee P.A. and Stewardson E.A., 1951, Proc. Phys. Soc. A64, 318
- (64) Lee P.A., Stewardson E.A. and Wilson J.E., 1952, Proc. Phys. Soc. A65, 668
- (65) Leipfinger H., 1958, Z. Physik. 150, 415
- (66) Liefeld R.J., Burr A.F. and Chamberlain M.B., 1974, Phys. Rev. 9A, 316

- (67) Lindberg E., 1931, Nova Acta Reg. Soc. Sci. Upsal.
7 No. 7
- (68) Lock J.M., 1957, Proc. Phys. Soc. B70, 476
- (69) Mariot J.M. and Karnatak R.C., 1974A, Phys. F.
4, L223
- (70) Mariot J.M. and Karnatak R.C., 1974B, Proc. Int.
Conf. X-ray Proc. in Matter, Helsinki University of
Technology, Otaniemi, Finland.
- (71) Massey H. and Burhop E., 1952, Electronic and Ionic
Impact Phenomena (O.U.P.)
- (72) Mayer M.G., 1941, Phys. Rev. 60, 184
- (73) McGuire E.J., 1971A, Phys. Rev. 3A, 587
- (74) McGuire E.J., 1971B, Phys. Rev. 3A, 1801
- (75) McGuire E.J., 1972A, Phys. Rev. 5A, 1043
- (76) McGuire E.J., 1972B, Phys. Rev. 5A, 1052
- (77) Motais P., Belin E. and Bohnelle C., 1981, J.
Phys. F. 11, L169
- (78) Ottewell D., 1969, Ph.D. Thesis, University of
Leicester
- (79) Ottewell D., Stewardson E.A. and Wilson J.E.,
1973, J. Phys. E. 6, 2184
- (80) Packwood R.H. and Brown J.D., 1981, X-ray Spectrom,
10, 138
- (81) Parratt L.G., 1939, Phys. Rev. 56, 295
- (82) Parratt L.G., 1959, Rev. Mod. Phys. 31, 616
- (83) Parrott M.A., 1965, Ph.D. Thesis, University of
Leicester

- (84) Prins J.A., 1930, Z.Phys. 63, 477
- (85) Protopopov V.N., 1948, Zav. Lab. 14, 2, 196
- (86) Ramberg E.G., 1934, Phys. Rev. 45, 389
- (87) Ramberg E.G. and Kennard E.H., 1934, Phys. Rev. 46, 1040
- (88) Rau A.R.P. and Fano U., 1968, Phys. Rev. 137, 167
- (89) Read F.H., Comer J, Imhof R.E., Brunt J.N.H. and Harting E., 1974, J. Elect. Spect. 4, 293
- (90) Richtmyer F.K., 1928, Phil. Mag. 6, 64
- (91) Richtmyer F.K. and Ramberg E.G., 1937 Phys. Rev. 51, 925
- (92) Rule K.C., 1945, Phys. Rev. 68, 246
- (93) Russel P.C., 1958, Ph.D. Thesis, University of Leicester
- (94) Senemaud C., 1963, Ph.D. Thesis, University of Paris
- (95) Siegbahn M., 1933, Nature 151, 502
- (96) Siegbahn M. and Leide A., 1919, Phil.Mag. 38, 647
- (97) Siegbahn M. and Stenstrom W., 1916, Z Phys. 17, 318
- (98) Spedding F.H. and Duane A.H., 1961, The Rare Earths, (Wiley, New York)
- (99) Soller W., 1924, Phys. Rev., 24, 158
- (100) Stewardson E.A. and Wilson J.E., 1956, Proc. Phys. Soc. A69, 93

- (101) Sugar J., 1972 A, Phys. Rev. 6A, 1764
- (102) Sugar J., 1972 B, Phys, Rev. 5B, 1785
- (103) Topp N.E., 1965, the Chemistry of the Rare Earth Elements (New York, Elsvier)
- (104) Tukey J.W., 1977, Exploratory Data Analysis, (Addison-Wesley)
- (105) Valadares M. and Mendes M., 1948, Comp, Rend. 226, 1185
- (106) Valasek J., 1938, Phys. Rev. 53, 274
- (107) Van der Berg C.B. and Brinkman H., 1955, Physica 21, 2, 85
- (108) Van der Tuuk J.H., 1927, Z.Phys. 44, 737
- (109) Wetterblad K., 1927, Z. Phys. 42, 611
- (110) Wentzel G., 1921, Ann. Phys. 66, 437
- (111) White J.E., 1950, J. Appl. Phys. 21, 855
- (112) Williams K.C., 1966, Proc. Phys. Soc. 87, 983
- (113) Wilson J.E., 1978, Private Communication, University of Leicester
- (114) Wolfe H.C., 1933, Phys. Rev. 43, 221
- (115) Zandy H.F., 1952, Proc. Phys. Soc. A65, 1015
- (116) Zandy H.F., 1967, Phys. Rev. 162, 1

ABSTRACT

The $m_{\alpha,\beta}$ x-ray emission spectra of some of the heavy rare earths were measured using a high resolution x-ray spectrometer. The x-ray spectrometer was designed to allow the preparation of pure samples in ultra-high vacuum conditions so that accurate spectra could be measured. Due to the large number of measurements necessary, the spectrometer was automatically controlled by a microprocessor based system.

From the high resolution data obtained, it has been possible to produce an explanation of the gross structures seen in the rare earth $m_{\alpha,\beta}$ x-ray emission spectra. It has been shown that the spectra are made up from several competing processes but that the main features can be explained in terms of resonant excitation of a 3d electron to the 4f shell followed by 4f - 3d emission and by normal 4f - 3d emission after ionisation of a 3d electron. Modifications to the spectra caused by excited final state transitions have also been observed. The dramatic effects on the m_{α} spectra of ytterbium due to chemical combination have also been explained in terms of the reduction of the 4f occupancy from $4f^{14}$ to $4f^{13}$.

It has been shown that much of the published data for the $m_{\alpha,\beta}$ rare earth emission spectra is incorrect. The distorting effects of self absorption and sample contamination have been shown to be particularly severe for the rare earths.